REVIEWS OF MODERN PHYSICS, VOLUME 83, OCTOBER–DECEMBER 2011

Physical basis of radiation protection in space travel

Marco Durante

GSI Helmholtzzentrum für Schwerionenforschung, Biophysics Department,
and Darmstadt University of Technology, Department of Condensed Matter Physics,
Planckstrasse 1, 64291, Darmstadt, Germany

Francis A. Cucinotta

NASA Lyndon B. Johnson Space Center, 2101 NASA Parkway, Houston, Texas 77058, USA

(published 8 November 2011)

The health risks of space radiation are arguably the most serious challenge to space exploration, possibly preventing these missions due to safety concerns or increasing their costs to amounts beyond what would be acceptable. Radiation in space is substantially different from Earth: high-energy (E) and charge (Z) particles (HZE) provide the main contribution to the equivalent dose in deep space, whereas γ rays and low-energy α particles are major contributors on Earth. This difference causes a high uncertainty on the estimated radiation health risk (including cancer and noncancer effects), and makes protection extremely difficult. In fact, shielding is very difficult in space: the very high energy of the cosmic rays and the severe mass constraints in spaceflight represent a serious hindrance to effective shielding. Here the physical basis of space radiation protection is described, including the most recent achievements in space radiation transport codes and shielding approaches. Although deterministic and Monte Carlo transport codes can now describe well the interaction of cosmic rays with matter, more accurate double-differential nuclear cross sections are needed to improve the codes. Energy deposition in biological molecules and related effects should also be developed to achieve accurate risk models for long-term exploratory missions. Passive shielding can be effective for solar particle events; however, it is limited for galactic cosmic rays (GCR). Active shielding would have to overcome challenging technical hurdles to protect against GCR. Thus, improved risk assessment and genetic and biomedical approaches are a more likely solution to GCR radiation protection issues.

DOI: 10.1103/RevModPhys.83.1245 PACS numbers: 87.50.−a, 96.50.S−, 94.05.S−, 94.05.Hk

CONTENTS

I. INTRODUCTION

The 20th century will be remembered as a time when mankind left planet Earth for the first time. The 21st century may well be the "age of maturity" for space exploration. Many nations now recognize space as a key driver for educational, economic, scientific, and technological advancement (ESA, 2007). In addition to the International Space Station (ISS), there are four destinations that offer suitable destinations for human explorers: the Moon, Mars, near Earth

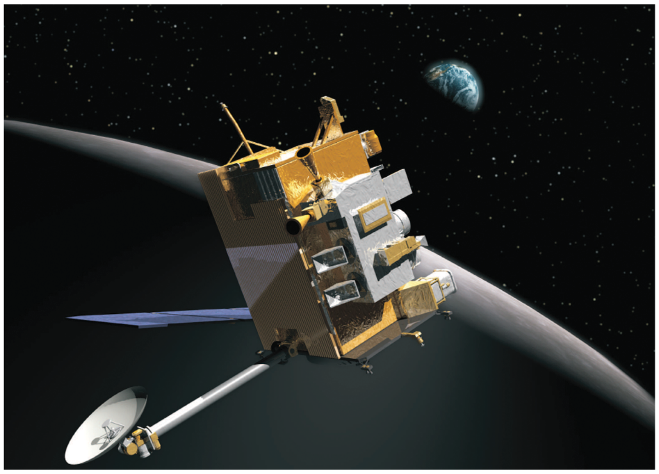

FIG. 1 (color). One of the first steps in the 21st century exploration plans has been the launch of the NASA Lunar Reconnaissance Orbiter (LRO) on 18 June 2009. LRO is in low-polar orbit (50 km altitude) around the Moon and is designed to generate a comprehensive atlas of the Moon's features and identifying available resources. Measurements of the lunar ionizing radiation environment represent one of the main goals of the LRO mission (see Sec. II.D.3), and two dedicated instruments are in the payload: CRaTER is a cosmic-ray telescope for the detection of charged particles with energies >10 MeV, and LEND is a spectrometer to measure neutrons at energies <15 MeV. Image: artist's view of LRO courtesy of NASA multimedia gallery.

objects (NEOs), and the Earth-Moon Lagrangian points. Each of these has a unique environment and offers different challenges and opportunities. Many robotic lunar missions from the USA, Russia, China, Japan, India, and Europe are already planned or are under way (Fig. 1). Once the ability to survive on the Moon and utilize the alien lunar environment has been demonstrated, the way will be open for the first human expeditions to Mars.

Scientific achievements expected from human exploration include exobiology and astronomical observatories on the Moon or in deep space laboratories. Technological and economic developments are linked to applied microgravity research, entrepreneurial activities, and space services, such as use of the Moon or asteroids as a source of natural resources and industrial raw materials, use specific areas of outer space as safe havens and operational hubs, and in-space infrastructures and services to support space exploration and make it sustainable.

The final goal of space exploration programs is enabling life in space through a stable and safe colonization of the Solar System. Can this be achieved? Certainly space is not a safe environment for humans and enabling life in space requires coping with several health problems (White and Averner, 2001). The risks of space travel have been comprehensively summarized in the NASA bioastronautics roadmap (NASA, 2005), now updated in the Human Research Roadmap[1], and current gaps in knowledge also identified. Risks were rated from 1 (risk of serious health effects, and mission could be impossible without mitigation) to 3 (suspected health consequences with limited impact on the mission design). The risks can be summarized into three broad categories (NASA, 2009):

(1) physiological problems caused by microgravity (or reduced gravity),
(2) psychological and medical problems caused by isolation, and
(3) acute and late risks caused by exposure to radiation.

The physiological changes in weightlessness have been extensively studied, especially during long-term missions on space stations (ISS and, previously, Mir) in low-Earth orbit (LEO). Bone loss, kidney stone formation, skeletal muscle mass reduction, cardiovascular alterations, impaired sensory-motor capabilities, and immune system dysfunctions are among the consequences of prolonged permanence in microgravity. The risks are well characterized and several countermeasures are available. None of these risk are given the highest rating of 1 (i.e., risk of serious adverse health consequences, and there is no mitigation strategy validated in space or demonstrated on Earth) in the bioastronautics roadmap (risk category 2 is associated with a serious risk with no countermeasure validated in space, and 3 is for known or suspected health consequences whose mitigation strategies have been validated in space).

Isolation may lead to serious neurobehavioral problems caused by poor psychosocial adaptation (NASA, 2009). Several ground platforms are used to study these problems and develop countermeasures, such as the Concordia base in Antarctica and the Mars500 isolation experiments currently under way in Russia. Isolation also brings the problem of autonomous medical care (AMC), i.e., the capability to handle sickness or accidents in complete isolation. This is clearly a risk category 1 for the mission to Mars. Countermeasures for AMC risks are mostly technological, i.e., rely on the development of portable medical equipment and telemedicine.

Finally, there are the risks related to exposure to space radiation (ESA, 2006). Because of the complex nature of the space radiation environment (see Sec. II), both acute (i.e., short-term risk of radiation sickness) and late (e.g., cancer) effects are possible. Acute radiation syndrome can be associated only with intense solar particle events (SPE) with crews unable to reach adequate shielding. Late radiation morbidity including cancer and other diseases of old age is associated with the chronic exposure to galactic cosmic radiation (GCR), which is substantially different both qualitatively and quantitatively from the Earth's radiation natural background. Because of the qualitative difference in the radiation spectrum (x, γ, β, and α rays on Earth; protons and heavy ions in space), the uncertainty in radiation risk estimates is very high, especially for carcinogenesis, central nervous system (CNS) damage, and late cardiovascular damage. Early estimates of the uncertainty on space radiation cancer mortality risk ranged from 400% to 1500% (NASA, 1998), with more precise estimates showing uncertainties at the 95% confidence level of 4-fold times the point projection (Cucinotta, Schimmerling *et al.*, 2001; Cucinotta and Durante, 2006). Despite the extensive ground-based experimental program currently ongoing, this uncertainty is still

---

[1] http://humanresearchroadmap.nasa.gov/.

very high (Schimmerling *et al.*, 1999; Durante and Cucinotta, 2008). Moreover, countermeasures are not easily available. In every radiation protection textbook it is normally stated that there are three means to reduce exposure to ionizing radiation: increasing the *distance* from the radiation source, reducing the exposure *time*, and by *shielding*. Cosmic radiation is isotropic, and therefore increasing the distance is not an option in space. Time in space should be increased rather than decreased according to the plans of exploration and colonization, although reduction of the transit time to the planet, where heavy shielding can be more easily achieved, may contribute to reducing radiation exposure (Durante and Bruno, 2010). Shielding remains as the only feasible countermeasure, but it cannot be a full solution for the GCR problem, even though it can significantly contribute to risk reduction (Wilson *et al.*, 1995). Very heavy shields are impractical on spaceships, although small ''storm shelters'' can be designed against intense SPE. Other strategies include the choice of an appropriate time of flight, i.e., mission planning and ability to predict solar particle events (see Sec. II.B), administration of drugs or dietary supplements to reduce the radiation effects, and crew selection based on genetic screening. However, it is generally acknowledged that the high uncertainty on risk estimates and the lack of effective countermeasures make cosmic radiation one of the main health concerns for space exploration.

A. Radiation protection quantities

The physical basis of radiation protection on Earth is well established and based on solid scientific evidence and epidemiological data, as summarized in the latest report to the United Nations (UNSCEAR, 2008) and of the US National Academy of Sciences (NRC, 2006). The new recommendations of the International Commission on Radiological Protection (ICRP) have been published in the recent report ICRP-103 (ICRP, 2007). The new ICRP recommendations formally replace the commission's previous (1990) recommendations (ICRP, 1991).

As described in Sec. II, the space radiation spectrum is a complex mixture of protons, neutrons, and heavy ions with energies from a few MeV/nucleon up to TeV/nucleon. All of these components can have substantially different relative biological effectiveness (RBE), which is defined as the ratio of doses of particles to γ rays that produce and equivalent biological effect. Therefore, measuring the dose D_{TR} (in gray, Gy) averaged over a tissue T by the tissue weighting fraction (w_T) (values shown in Table I) due to radiation R does not provide information about the biological response. An approximate scheme is to calculate the equivalent dose H_T (in sievert, Sv) in the organ or tissue T using

$$H_T = \sum_R w_R D_T, \quad (1)$$

where w_R is the so-called radiation weighting factor, whose values are based on the review of biological information. The revised w_R values reported in the ICRP-103 are provided in Table I, and the energy-dependent values for neutrons are provided in Fig. 2.

TABLE I. Radiation (w_R) and tissue (w_T) weighting factors, as recommended in the latest ICRP-103 report (ICRP, 2007).

Radiation type	w_R
X and γ rays	1
Electrons and muons	1
Protons and charged pions	2
α particles and heavy ions	20
Neutrons	2–20 (see Fig. 2)
Organ	**w_T**
Breast, bone marrow, lung, colon, stomach	0.12
Gonads	0.08
Bladder, liver, esophagus, thyroid	0.04
Bone surface, brain, salivary glands, skin	0.01
Remainder	0.12

Exposure of different organs or tissues is associated with different risks of stochastic effects. For example, irradiation of blood-forming organs (BFO) will produce a much higher risk of leukemia than skin irradiation. If the irradiation is not uniform, the different values of H_T have to be weighted when estimating the risk. Although a whole-body exposure is expected in space, doses to different organs can be substantially different for solar particle events while very similar for GCRs (see Sec. II.D.2). To estimate the risk of all stochastic effects, whether the body is exposed uniformly or not uniformly, the ICRP recommends the use of a gender and age independent effective dose E (also measured in Sv):

$$E = \sum_T w_T \left(\frac{H_T^M + H_T^F}{2} \right), \quad (2)$$

where the indices M and F refer to male and female reference phantoms, respectively. Of course, radiation risks depend to a large extent on age and gender, making the use of Eq. (2) highly inaccurate for risk estimation. There is an inherent assumption in the ICRP approach that the worker exposures are well below limits making crude approximations acceptable.

In space radiation protection, however, radiation weighting factors are not used. As a matter of fact, the space radiation

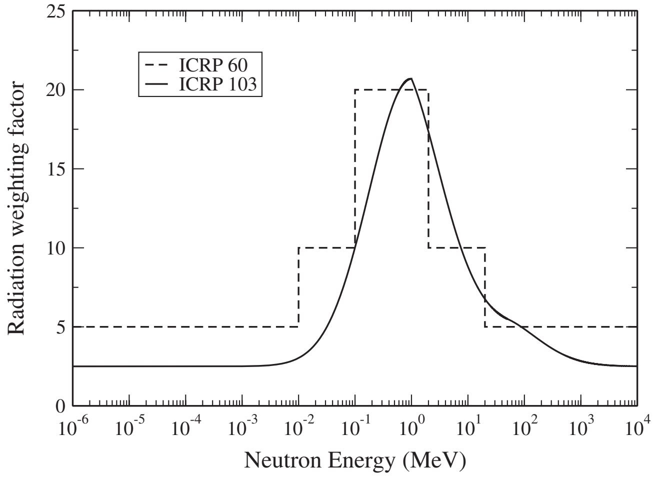

FIG. 2. Radiation weighting factor w_R for neutrons at different energies. The step function is from ICRP60 (1991), and the continuous function is the latest ICRP-103 (2007) recommendation.

spectrum in different organs is a complicated mixture of primary and secondary charged particles with different energies. ICRP-103 indeed acknowledges explicitly the following:

"The selection of a single w_R value of 20 for all types and energies of heavy charged particles seems to be a conservative estimate for many particles and is recommended as sufficient for general application in radiological protection. For applications in space, where these particles contribute significantly to the total dose in the human body, a more realistic approach may be used." (ICRP, 2007, para. 124,).

The approach recommended by the National Council on Radiation Protection and Measurements (NCRP), at least for LEO (NCRP, 2000), is to use the organ dose equivalent H_T defined by ICRU (1993) as a mass m average over the tissue:

$$H_T = \frac{1}{m}\int_m dm \int Q(L)F_T(L)LdL, \tag{3}$$

where L is the linear energy transfer (LET $= dE/dx$, normally expressed in keV$/\mu$m), m is the organ mass, F_T is the fluence of particles through the organ T, and Q is the quality factor (dimensionless), which was adopted in radiation protection (ICRP, 1977) prior to the introduction of the weighting factors. In radiation protection LET refers to the local energy deposition, which is approximated by the stopping power. Unlike the weighting factors (Table I), Q is a continuous function of LET. The latest recommendations for $Q(L)$ are provided by the ICRP-60 (ICRP, 1991) and are given in Fig. 3. The integration over the mass of the organ is approximated by averaging over a number of points within the organ, for example, 33 representative points for the BFO in a reference phantom. As discussed in Sec. V, most of the uncertainty in Eq. (3) is associated with the quality factor Q. There is also clear experimental evidence that the biological effectiveness of charged particles depends on both Z and β, i.e., on the track structure, and not on the LET alone (Katz, Scharma, and Homayoonfar, 1972; Belli *et al.*, 1993; Cucinotta, Wilson *et al.*, 1996; Schardt, Elsässer, and Schulz-Ertner, 2010). Nevertheless, $Q(L)$ represents a first approximation of the changes in RBE in a mixed radiation field such as that in space.

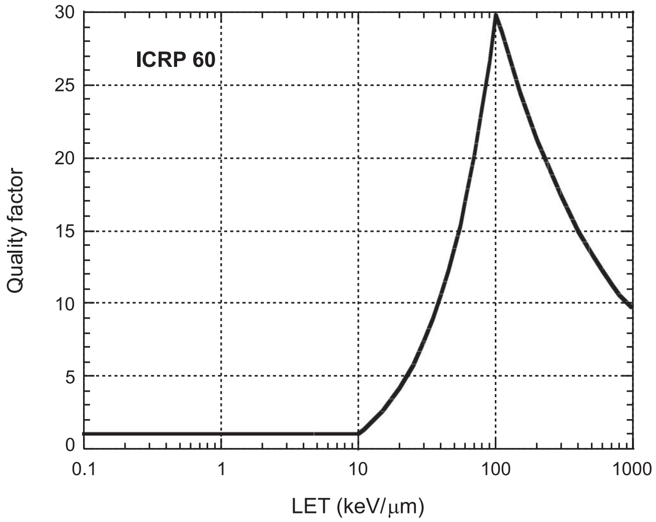

FIG. 3. Dependence of the quality factor Q from LET according to the latest ICRP recommendations.

Effective or equivalent doses are ultimately used to estimate radiation protection limits. The protection for workers on Earth relies in the first place on the so-called as low as reasonably achievable (ALARA) principle, as formulated by ICRP (ICRP, 1977): "All radiation exposures should be kept as low as reasonably achievable, economic and social factors taking into account." There is not enough scientific evidence to support a lower bound on what constitutes a harmful dose, and the issue of low-dose research is always a major component in research programs in the USA and Europe (HLEG, 2009). In practice ALARA is not a scientific principle, but rather a management tool to implement safety factors below dose limits using cost-benefit analysis.

B. Exposure limits

As yet, terrestrial exposure limits from the ICRP are largely based on cancer risk with an added contribution from hereditary risks as reflected in the tissue weights of Table I. This is due to the evidence that cancer occurs at much lower doses than any acute effects. A single coefficient is used at all doses assuming a low dose-rate exposure, thus following the linear-no-threshold dose-response model, which despite many controversies has not been disproved (Brenner *et al.*, 2003; Mullenders *et al.*, 2009). The estimates of cancer risk attributable to radiation exposure have not changed greatly in the past years and continue to be largely based on the life span study (LSS) of the survivors following the atomic bombings of Hiroshima and Nagasaki. The LSS estimates (which correspond to acute exposure) are corrected by a dose and dose-rate effectiveness factor (DDREF) for solid cancers, which takes into account the reduced radiation effectiveness at a low dose rate: ICRP-103 upheld their recommendation of the previous DDREF value of 2, while the BEIR VII report argues for a lower value of 1.5 which would increase solid cancer risk estimates by 33% over the older value. Finally, ICRP-103 (ICRP, 2007) still recommends a risk coefficient for an average population of 5×10^{-2} Sv^{-1}, which was also proposed in ICRP-60 (ICRP, 1991). The corresponding radiation limits for the radiation workers and the general population are summarized in Table II. For comparison, typical doses associated with medical imaging exposures to ionizing radiation are also shown. The average annual effective dose on Earth is about 3 mSv and is reduced to less than 1 mSv if man-made sources and the internal α-particle exposure to Rn daughters are excluded. A few areas on Earth display anomalously high levels of background radiation, as is the case with Th-rich monazite sands, where values 200–400 times higher than the world average can be found (UNSCEAR, 2000). It should also be noted that approximately 20% of the U.S. population receives annual effective doses exceeding the natural 3 mSv background (Fazel *et al.*, 2009). Dose rates in space are definitely higher than on Earth, although still in the low-dose region. The equivalent dose rate in LEO is about 1 mSv/day; on Mars it ranges between 100 and 200 mSv/yr (Durante and Bruno, 2010), depending on the solar cycle and altitude; values around 350 mSv/yr can be reached on the Moon

TABLE II. Effective dose limits recommended by ICRP-103 (ICRP, 2007), and comparison with typical exposures due to medical procedures (Fazel *et al.*, 2009). The medical exposures are not considered in the computation of the maximum dose.

Exposure	Occupational (mSv)	Public (mSv)
Maximum effective dose per year	20 mSv, average over defined periods of 5 yr	1 mSv
Medical procedure		
Chest x-ray film (posteroanterior)		0.02
Computed tomography (CT) chest		7.0
CT abdomen		8.0
CT angiography		15.0
Mammography		0.4
Myocardial perfusion imaging		15.0
Urography		3.0
Nuclear bone imaging		6.0

(ESA, 2003). Therefore, astronauts experience a considerably higher radiation risk than the population on Earth and occupationally exposed workers, particularly considering that the latter group receives on average far lower doses than the annual limits. NASA has put in place a new approach for radiation limits that accounts for uncertainties at the 95% confidence level (Cucinotta, Hu *et al.*, 2010). This approach shows how research to lower uncertainties will be the most cost effective method to enable long-term space missions.

ALARA should be used to optimize radiation protection in space missions too. For astronauts, the recommendations of NCRP (2000) have been issued only for activities in LEO and are based on 3% risk of exposure-induced cancer mortality. If the maximum dose for radiation workers in Table II is applied, a career lifetime excess risk of approximately 3% is indeed reached (assuming a 10 yr career). The risk coefficients are age and gender dependent, and this was carefully considered by NCRP. The corresponding NASA astronaut career limits are reported in Table III and compared with those from other space agencies. The European, Canadian, and Russian space agencies do not adopt age- and gender-corrected coefficients, but rather resort to a single career limit of 1 Sv. These limits are, however, currently under revision (Straube *et al.*, 2010). For exploratory-class missions beyond LEO, a description of the major information needed to issue recommendations has been instead provided in a dedicated NCRP report (NCRP, 2006).

TABLE III. Age- and gender-dependent career effective dose limits (in Sv) as recommended by different space agencies (Cucinotta, Hu *et al.*, 2010; Straube *et al.*, 2010). NASA limits are always based on 3% risk of exposure-induced death, and the values refer to a 1 yr mission. Different values will be calculated for different mission durations (Cucinotta, Hu *et al.*, 2010).

		Age at first exposure, (yr)			
Space agency	Gender	30	35	45	55
NASA (USA)	Female	0.47	0.55	0.75	1.1
	Male	0.62	0.72	0.95	1.5
JAXA (Japan)	Female	0.6	0.8	0.9	1.1
	Male	0.6	0.9	1.0	1.2
ESA		1.0	1.0	1.0	1.0
FSA (Russia)		1.0	1.0	1.0	1.0
CSA (Canada)		1.0	1.0	1.0	1.0

II. SPACE RADIATION ENVIRONMENT

The radiation environment in the Solar System is a complex mixture of particles of solar and galactic origin with a broad range of energies. For radiation protection, the problems are related to GCRs and particles ejected from the Sun during SPEs, as well as secondary radiation produced through interaction with planetary surfaces. The solar wind particles, even when enhanced due to higher solar activities, do not contribute to the radiation burden to astronauts due to their relative low energy and hence their absorption in already very thin shielding thicknesses. Nevertheless, the solar wind modulates the flux of galactic cosmic rays in the energy range below about 1 GeV/nucleon, with a fairly regular 11-yr long cycle (see Fig. 4 for current solar activity and predictions for the next cycle based on sunspot numbers). During phases of higher solar activity the cosmic-ray flux is decreased by a factor of 3 to 4 against phases during minimum solar activity. However, the probability of SPE is higher during solar maximum. The question is then whether a mission should be planned in solar minimum (lower chance of acute exposure from SPE, but higher GCR risk) or solar maximum. However, there is no clear pattern of SPE occurrence with large SPEs observed in about 9 of the 11 years of any given solar cycle.

Through the Earth's magnetic field and an atmospheric thickness of about 1 $\mathrm{kg/cm^2}$ thickness, the exposure to cosmic radiation on the Earth's surface is reduced to a nearly zero level. Leaving Earth astronauts are shielded by the structure of the spacecraft. For the ISS the interior is shielded on average by 20 $\mathrm{g/cm^2}$, a shielding close to that of the Martian atmosphere. In LEO astronauts are still protected by the magnetosphere which limits even the exposure to solar

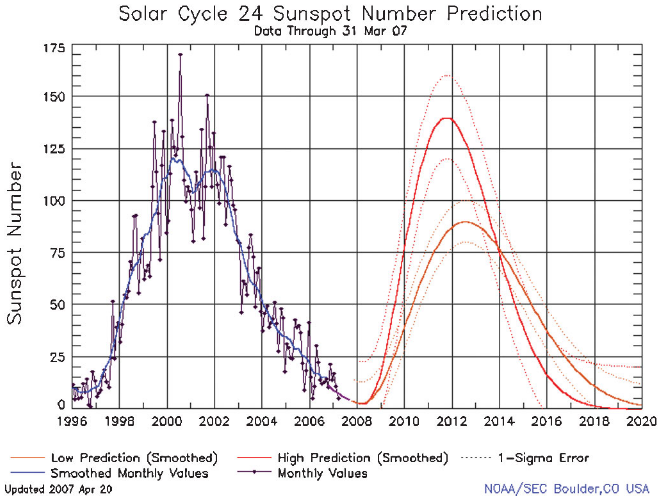

FIG. 4 (color). Solar cycle 23 and predictions of the sunspot numbers for solar cycle 24 using different models. The next solar maximum is expected in late 2001–mid 2012, and the next solar minimum around 2019. Data and prediction from the NOAA/NSW Space Weather Prediction Center (http://www.swpc.noaa.gov/).

energetic particles to exposures far below such causing acute radiation effects in man. SPE are, therefore, mostly an issue for exploratory-class missions.

A. Galactic cosmic radiation

Galactic cosmic radiations originate outside the Solar System and impinge isotropically on Earth. Because of their high energies (up to 10^{20} eV), they most probably originate from supernova explosions, neutron stars, pulsars, or other sources where high energetic phenomena are involved (Cronin, 1999). Detected particles consist of 98% baryons and 2% electrons. The baryonic component is composed of 85% protons (hydrogen nuclei), with the remainder being helium (14%) and heavier nuclei (about 1%). Figure 5 (Cucinotta *et al.*, 2003; Durante and Cucinotta, 2008) using the HZETRN code (Wilson *et al.*, 1991; Wilson *et al.*, 1995; Tweed, Wilson, and Tripathi, 2004) and the Badhwar–O'Neill GCR model (Badhwar and O'Neill, 1994; O'Neill, 2010) shows the relative contribution of the different elements in flux, dose, and equivalent dose. The energetic ions heavier than helium nuclei have been termed HZE particles (high charge Z and high energy E). Although iron nuclei are only one-tenth as abundant as carbon or oxygen their contribution to the GCR equivalent dose is higher than protons, since the dose is proportional to the square of the charge and Q is high (Fig. 3). The GCR make up more than 80% of the effective doses to crews on ISS, much higher than trapped radiation because of their higher penetration power to deep seated organs and large quality factors (Cucinotta, Nikjoo, and Goodhead, 2000; Cucinotta *et al.*, 2008).

In addition to the galactic cosmic rays, the so-called anomalous component [anomalous cosmic rays (ACRs)] is observed. ACRs consist of originally neutral particles coming from the interstellar gas which become single ionized by solar radiation after entering the heliosphere. These particles are then accelerated in collision regions between fast and slow moving streams of the solar wind. They are able to penetrate deeper into the magnetic field than fully ionized cosmic rays. Their energies are around 20 MeV/nucleon. Therefore, they can contribute only to radiation effects behind small shielding. However, it has to be considered that they lose all their electrons after penetration of a very small amount of shielding material and thus also deposit energy proportional to the square of their charge.

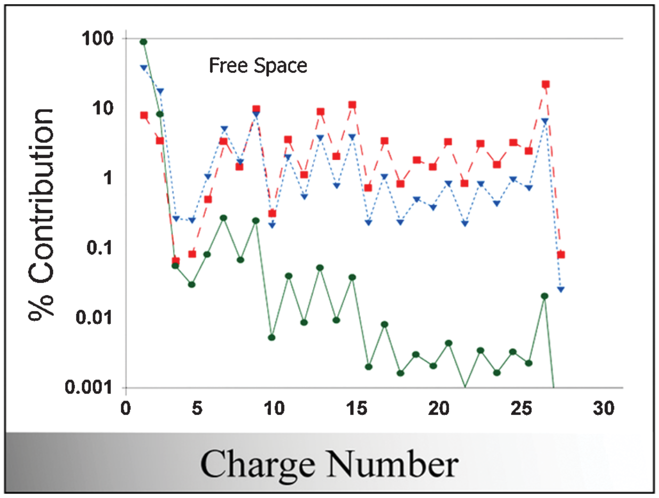

FIG. 5 (color). Relative contribution in fluence (circles), dose (triangles), and dose equivalent (squares) of different elements in the GCR from the HZETRN computer code as reproduced from Cucinotta *et al.* (2003) in Durante and Cucinotta (2008). The calculation is an average over 1-year in solar minimum behind 5 g/cm^2 Al shielding.

The propagation of cosmic rays in the interplanetary medium can be described by a Fokker-Planck equation. If U is the cosmic-ray density, E is the particle kinetic energy, V is the velocity, and κ^s is the symmetric part of the diffusion tensor, the basic equation is (Parker, 1965)

$$\frac{\partial U}{\partial t} = \nabla(\kappa^s \cdot \nabla U) - \vec{V} \cdot \nabla U + \frac{1}{3}\nabla \cdot \vec{V}\frac{\partial}{\partial E}\left[\left(1 + \frac{m}{E+m}\right)UE\right] = 0, \tag{4}$$

where m is the proton rest mass. A full numerical solution of the equation is given by the deceleration potential ϕ (in MV):

$$\phi(r,t) = \frac{1}{3}\int_r^{r_B} \frac{\vec{V}_w(r',t)}{\kappa(r',t)}dr', \tag{5}$$

where r_B is the radial extent of the heliosphere, κ is the diffusion coefficient, and V_w is the solar wind velocity. The deceleration potential is the most important parameter in describing the modulation of GCR intensity. An approximate solution for the integral fluence $j(r,E)$ at high energies (≥ 300 MeV/nucleon) can be expressed as a function of the deceleration potential ϕ as

$$\frac{j(r,E)}{E^2 - m^2} = \frac{j_0(r_B, E + Ze\phi)}{(E + Ze\phi)^2 - m^2}, \tag{6}$$

where j_0 is the local interstellar spectrum. Equation (6) basically represents the standard convection-diffusion model of the GCR modulation, and although it does not explain the radial gradient and the charge dependence, it is widely used to predict the fluence rate $j(Z,E,t)$ in any point r in the heliosphere. Since there are no measurements of j_0, different forms for this function have been used, with the constraint that the high-energy portion of the spectrum agrees with the measurements in LEO. The different GCR models currently used basically differ in the choice of this function and the solar activity parameter used for prediction. For instance, in Nymmik's model (Nymmik, 1996), also known as the Moscow State University model, j_0 is described as a function of the particle velocity β and rigidity R as

$$j_0(Z,E)dE = C\beta^\alpha R^\gamma\left(\frac{dE}{\beta}\right), \tag{7}$$

where C, α, and γ are Z-dependent parameters derived from fits to experimental data. To obtain the modulated fluence rate $j_n(Z,E,t)$ at time t during the nth solar cycle, the local interstellar spectrum in Eq. (6) must be multiplied by a modulation function Ψ, which is a function of the deceleration potential, the rigidity, and the Wolf sunspot number. Hence, Nymmik's model is a semiempiric approach which relates the solar-cycle variation in the GCR intensity to the observed time history of the Wolf sunspot number. It is quite accurate, with an estimated uncertainty below 15%, and therefore commonly used. It is, for example, used in the CREME-96 software (Tylka *et al.*, 1997), the most recent update of the original cosmic-ray effects on microelectronics model developed at the Naval Research Laboratory to predict effects of cosmic rays on microelectronics on space.

There are also other models based on the standard diffusion-convection theory of modulation, but different empirical formulation for the local interstellar spectrum: widely used are the CRRES/SPACERAD heavy ion model of the environment (CHIME) model (Chen *et al.*, 1994) and the Badhwar–O'Neill (or Johnson Space Center) model (Badhwar and O'Neill, 1994; O'Neill, 2010). These models are based on a fit of the high-energy component of the GCR differential flux using a power law:

$$j_l = j_0 \beta^{\delta} (E + E_0)^{-\gamma}, \tag{8}$$

where E and E_0 are, respectively, the particle kinetic and rest energy and/or nucleon, and γ, δ, and j_0 are the fitting parameters for each charge group.

The Badhwar–O'Neill model (Badhwar and O'Neill, 1992, 1994; O'Neill, 2010) was developed upon a self-consistent fit of the diffusion equation (4) to a large number of satellite, balloon, and more recently data from the advanced composition explorer in order to describe solar modulation effects. This fit provides the high-energy portion of j_0, which is then modulated using the deceleration potential. The Badhwar–O'Neill model has been fit either to the Wolf sunspot numbers or to cosmic-ray neutron monitor counting rates as predictors of the solar activity. This flux has been measured over long periods by different ground-based stations using neutron monitors. Despite statistical fluctuations, maxima and minima of the neutron spectra are clearly anticorrelated to the 11-yr solar cycle with a roughly sinusoidal form around an average particle flux.

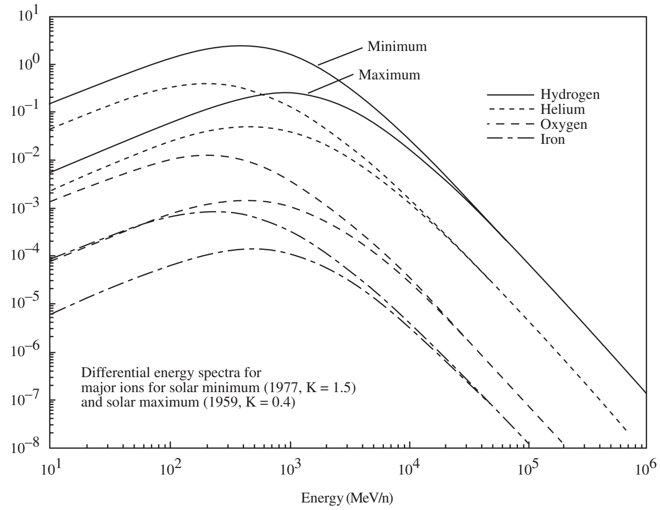

FIG. 6. GCR particle spectra (H, He, O, and Fe) and their modification by solar activity at 1 AU (Badhwar and O'Neill, 1992; Badhwar, Cucinotta, and O'Neill, 1993) and reproduced in NCRP (2000).

The accuracy of the current models of the GCR is around 10% for most ions at energies <5 GeV/nucleon, i.e., in the region where the solar modulation is most important. Figure 6 reproduces the differential spectra for H, He, O, and Fe for the 1977 solar minimum and 1959 solar maximum, the two cycles with the strongest modulation of the past 50 years. It is noteworthy that the maximum of the spectrum is around 1 GeV/nucleon for all ions, shifting from lower to higher energies and lower fluence in solar maximum.

B. Solar particle events

Besides electromagnetic radiation, the Sun continuously emits particle radiation, consisting mainly of protons and electrons, the so-called solar wind. The intensities of these low-energy particles vary from 10^{10} to 10^{12} particles $\mathrm{cm^{-2}\,s^{-1}\,sr^{-1}}$ with velocities between about 300 and $800\ \mathrm{km\,s^{-1}}$. The related energies are so low (for a proton between 100 eV and 3.5 keV) that the particles will be stopped within the first few hundred nm of skin. They are therefore not of concern for radiation protection.

However, occasionally the surface of the Sun releases large amounts of energy in sudden local outbursts of hard and soft x rays and radio waves in a wide frequency band. In these SPE large currents and moving magnetic fields in the solar corona accelerate solar matter [reviewed in NCRP (2006)]. Coronal particles, mostly protons (McGuire, von Rosenvinge, and McDonald, 1986) with a small fraction of heavier nuclei (Table IV), with energies up to several GeV escape into the interplanetary space. They spiral around the interplanetary magnetic field lines. Within the ecliptic plane field lines expand from the Sun into the interplanetary medium similar to the beam of a rotating garden hose. They connect the Earth with a certain spot on the western part of the Sun. The number and energy spectrum of particles observed in SPE at Earth depends on this connection. SPE show an enormous variability in particle flux and energy spectra, but the most intense events (Fig. 7) have the potential to expose unshielded space crews to life threatening doses (Kim *et al.*, 2009a). Since high energetic particles are arriving first and followed by particles of lower energies the energy spectrum of SPE

TABLE IV. Elemental composition of SEP (McGuire, von Rosenvinge, and McDonald, 1986). The solar energetic particle baseline (SEPB) is defined as the ratio of the flux of each element compared to oxygen. Protons account for about 98% of the composition in flux, but helium ions can give a contribution around 10% in dose.

Particle	SEPB	Particle	SEPB
H/O	3500 ± 500	Na/O	0.0083 ± 0.0015
He/O	53 ± 5	Mg/O	0.183 ± 0.010
Li/O	<0.001	Al/O	0.0115 ± 0.018
Be/O	$<5 \times 10^{-4}$	Si/O	0.147 ± 0.009
B/O	$<5 \times 10^{-4}$	P/O	0.0014 ± 0.0006
C/O	0.454 ± 0.018	S/O	0.0229 ± 0.0025
N/O	0.129 ± 0.008	Ar/O	0.0016 ± 0.0007
O/O	$\mathbf{1.00 \pm 0.031}$	Ca/O	0.0076 ± 0.0016
F/O	$<5 \times 10^{-4}$	(Ti + Cr)/O	0.0024 ± 0.0009
Ne/O	0.128 ± 0.008	Fe(group)/O	0.066 ± 0.006

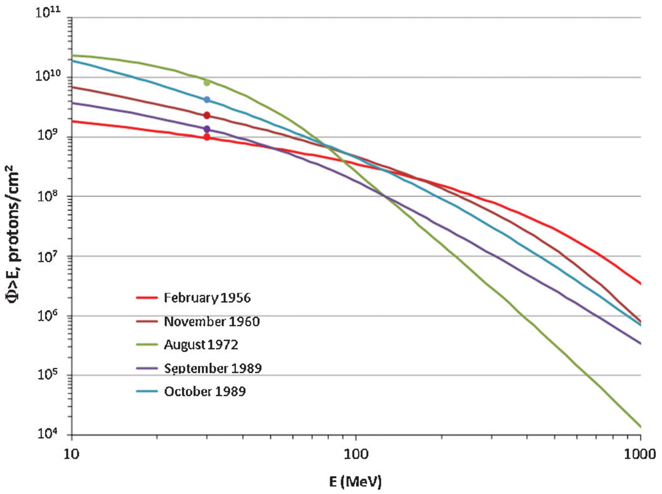

FIG. 7 (color). Integral energy spectra of intense solar particle events in the 20th century [Kim, Tylka, Atwell, and Cucinotta (unpublished)].

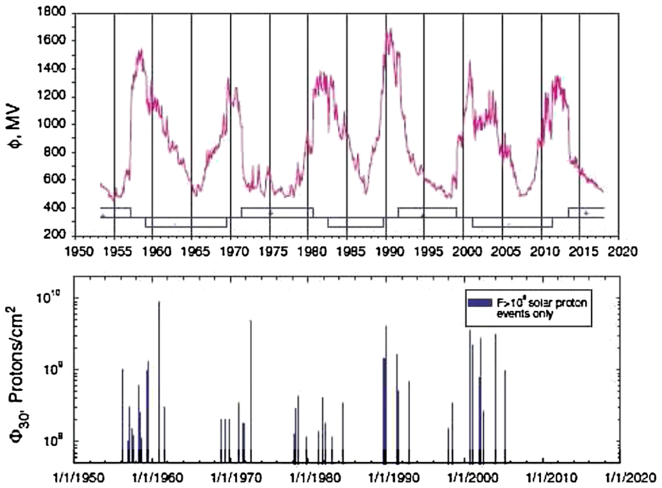

FIG. 8 (color online). GCR deceleration potential [Eq. (2)] and large (proton fluence $> 10^8\ \mathrm{cm}^{-2}$ at $E > 30$ MeV) GLE occurrences as a function of time. From NASA, 2009.

particles observed at Earth depends on time after the onset of the event. Differential energy spectra of solar particle events can be represented by a power law (Nymmik, 1996):

$$\frac{df}{dE} = f_0 k \alpha E^{\alpha-1} e^{-kE^{\alpha}}, \tag{9}$$

where f is the proton fluence and f_0, k, and α are three fitting parameters. However, other functional forms can be used, including a Weibull function or a double power law in the rigidity function (Band, 1993; Tylka and Dietrich, 2009). Different functional forms to represent SPE spectra will often result in different predictions of doses behind shielding.

A well-connected SPE with high particle fluxes observed at Earth is a rare event which is likely to be observed during the period of increasing and decreasing maximum solar activity. Therefore, major SPEs are observed at Earth as random events with a low frequency, typically one per month. They last for several hours or days. Events with significant fluxes of protons with higher energies can be observed as "ground-level events" (GLE) by neutron monitors (Tylka and Dietrich, 2009). Figure 8 shows the number of GLEs observed over the last solar cycles and their correlation with the deceleration potential ϕ [Eq. (5)], i.e., the solar-cycle phase. Long gaps with no events can be seen during solar minimum activity. Between the last GLE in cycle 21 and the first one in cycle 22 there was a 65 month quiet period which was followed by a sequence of 11 GLEs within 1 yr.

For radiation protection purposes, it is important to predict intensity, energy, and duration of a SPE. In general, energies of SPE are lower than GCR, and shielding is therefore a possible solution. Storm shelters, i.e., small areas with thick shields, are included in spacecrafts and can be built in planetary stations. Maximum risk will be during extravehicular activities (EVA) with minimal shielding, especially planetary exploration when astronauts can be very far from the Moon (or Mars) base. Since, unlike GCR, intense SPE can be life threatening or induce acute radiation syndromes (including nausea and possibly vomiting), they represent not only a health problem, but an operational issue of great concern. Intense SPE are seldom, but their occurrence is not negligible. The large solar flares of August 1972 (Fig. 7) might have caused prodromal syndromes for an unprotected crew on the lunar surface (Hu *et al.*, 2009). Only four months before the event, Apollo 16 was on the Moon. Although the events in Fig. 7 are generally used to construct "worst case scenario" energy-flux spectra for planning shielding and protection (Spillantini *et al.*, 2007), we are aware of at least one event in the past 500 years much more intense than anyone else recorded: the so-called "solar superstorm," also known as the "Carrington event," because it was recorded by the British astronomer Richard Carrington from 28 August to 2 September 1859 (Cliver, 2006). Apart from the original reports and visual observations of the event, the analysis of nitrate concentrations in ice cores proves that the protons fluence at energies >30 MeV was close to $2 \times 10^{10}\ \mathrm{cm}^{-2}$ at the top of the polar atmosphere, and it would have been similar in LEO. Reconstruction of the energy spectrum is particularly problematic, but the lack of ^{10}Be in the ice core suggests that this was a soft event. Using this spectrum, it has been estimated that the skin dose for an unprotected crew in EVA would have been about 35 Gy, but a normal spacecraft shielding of 5–10 $\mathrm{g/cm^2}$ Al would be sufficient to reduce the BFO dose to 0.2–0.7 Gy (Townsend *et al.*, 2006). Events of this intensity are very rare, perhaps 1–2 per millennium, and clearly their effect strongly depends not only on the fluence, but on the energy spectrum. A Carrington event with a spectrum such as, for instance, the September 1989 event (Fig. 7), would lead to much higher doses, radiation sickness even for crews inside spacecrafts, and catastrophic consequences for the electronics in space.

Because intense SPE are seldom, of relative short duration, and can generally be shielded effectively, any risk would be minimized if an adequate forecast system would be available. Unfortunately, our current forecasting ability is quite limited.

Several statistical models of SPE occurrences are available: the King model (King, 1974), the Jet Propulsion Laboratory (JPL) model (Feynman *et al.*, 1993), the Emission of Solar Protons (ESP) model (Xapsos *et al.*, 2000), and the NASA SPE Propensity Model (Kim *et al.*, 2009a, 2009b).

The King and JPL models are useful for predicting event fluences for long-term degradation but do have limitations due to the incomplete nature of the data sets upon which they were based. For instance, they do not accurately describe the complete distribution, allow for the possibility of infinitely large events, and lack strong physical and mathematical justification. In the ESP model a more accurate approach, based on the maximum entropy theory, is used to generate the initial distribution of SPE fluences. The basic idea is to maximize the entropy S defined for the variable $M = \log f$ as

$$S = -\int p(M) \log p(M) dM. \tag{10}$$

Defining the boundary conditions, a system of mathematical equations is used to find the solution $p(M)$ that maximizes S, by means of the Lagrange multiplier technique.

The model developed at NASA Johnson Space Center (Kim *et al.*, 2009a, 2009b) considered the 370 SPEs that were identified during solar cycles 19–23. Fluence data were combined over all 5 cycles to estimate an overall probability distribution of Φ_{30} for an average cycle. Between the years 1561 and 1950, 71 SPEs with $\Phi_{30} > 2 \times 10^9$ protons cm^{-2} (McCracken *et al.*, 2001) were also identified from impulsive nitrate enhancements in polar ice cores, and these events were shown to have a similar probability of occurrence as the large events occur during solar cycles 19–23 (Kim *et al.*, 2009a).

In the Poisson process model, the propensity for SPE occurrence at time t is a continuous function of t, known as the hazard function. More formally, the hazard function, say

$$\lambda(t) = \lim_{h \to 0} \frac{P\{\mathrm{SPE}_{\mathrm{occurrence}}(t, t+h)\}}{h}. \tag{11}$$

In terms of $\lambda(t)$, $E\{N(t_1, t_2)\}$, the expected number of events in an interval (t_1, t_2) is equal to $m(t_1) - m(t_2)$, where $m(t)$ known as the "mean value function," is the cumulative hazard:

$$m(t) = \int_0^t \lambda(u) du. \tag{12}$$

The functional form best explaining the data was found to be proportional to a beta distribution density function offset by a quantity λ_0; i.e.,

$$\lambda(t) = \frac{\lambda_0}{4000} + \frac{K}{4000} \frac{\Gamma(p+q)}{\Gamma(p)\Gamma(q)} \left(\frac{t}{4000}\right)^{p-1} \left(1 - \frac{t}{4000}\right)^{q-1}$$
$$(0 \leq t \leq 4000) \tag{13}$$

for a "typical" nonspecific cycle of 4000 days' duration, where λ_0, K, p, and q are parameters to be estimated. After redefining SPE occurrence times relative to 4000-day cycles and combining across all 5 cycles, the method of maximum likelihood was used to estimate the unknown parameters λ_0, K, p, and q (Kim *et al.*, 2009a). From Eq. (10), it can be shown that μ, the time of peak hazard, is $4000(p-1)/(p+q-2)$ days into a cycle. For the observed data, μ was estimated at 1783 days. Using this approach the number of events for a given mission length and period within the mean cycle can be predicted. A similar analysis is used to predict the number of events over a given threshold of 30, 60, and 100 MeV proton fluence (Kim *et al.*, 2009b).

In addition to knowing the expected number of SPEs of a given size within a mission period, the actual distribution of $N_a(t_2) - N_a(t_1)$, the numbers of such events, provides useful information for mission planning. Using the fitted Poisson model, the estimated cumulative probability distributions of $N_a(t_2) - N_a(t_1)$ can be calculated (Kim *et al.*, 2009b): for a 120-day mission the probability of at least one "large" SPE (Φ_{30} fluence greater than 10^7 protons cm^{-2}) is about 0.8 (80%), with the probability of having at least two large SPEs, about 50% and about 20% for more than two SPEs, etc. As mission durations reach 540 days, there is almost no chance of avoiding an SPE whose event size is greater than 10^7 protons cm^{-2}. The probability for multiple numbers of SPE occurrences is increased for longer missions and decreased for higher thresholds.

All these models can be used to estimate the probability of large SPE and planning of shielding amounts based on probabilistic risk assessment concepts, but do not represent a "warning system" of practical use. It was recently shown (Posner, 2007) that detection of relativistic solar electrons

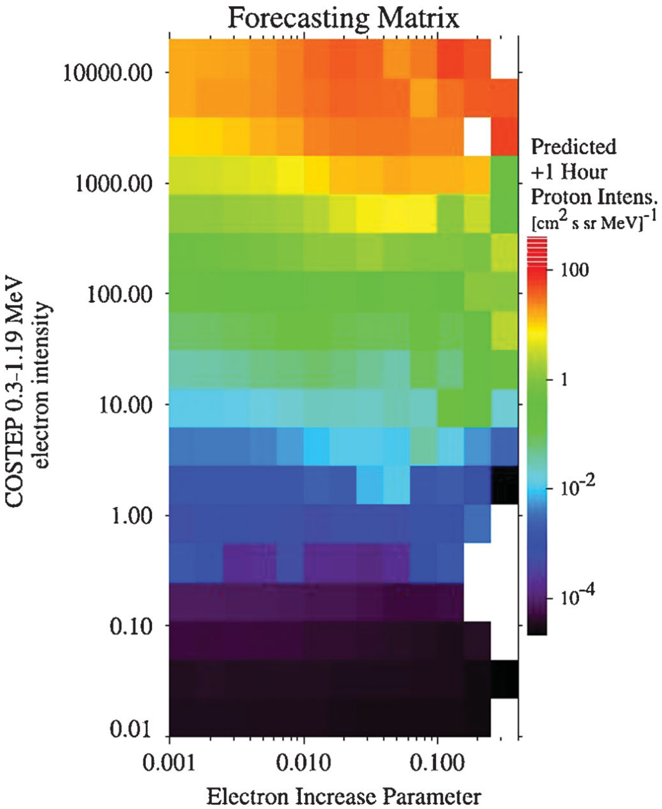

FIG. 9 (color). This color matrix provides a color code for the future proton intensity, 1 hour ahead of time, as predicted by relativistic electron measurements. The parameter space is given by the current maximum electron increase parameter, going back in time for at least 5 min, but up to 60 min, and the current relativistic electron intensity. The matrix is derived from the aggregate of all 1998–2002 relativistic electron observations and their corresponding 30–50 MeV proton intensities 1 hour later. The color shows the average for the proton intensity in each locus. Low statistics limit the extent of the matrix to the bottom and upper right. From Posner, 2007.

may enable a prewarning of up to 1 hour of subsequent proton events and allow prediction of the integral number of protons. The color matrix in Fig. 9 provides a code to predict future proton intensity, 1 hour ahead of time, as predicted by relativistic electron measurements. Quantities reported on the two axes are the current maximum electron increase parameter, going back in time 5 to 60 min, and current relativistic electron intensity. The matrix is derived from the aggregate of all 1998–2002 relativistic electron observations and their corresponding 30–50 MeV proton intensities 1 hour later. The database used contains both "impulsive" (flare-accelerated) and "gradual" (coronal-mass-ejection-accelerated) events. The color shows the average for the proton intensities in each locus. Statistical considerations limit the utility of the matrix at the bottom and upper right ranges. These findings not only provide evidence of up to a 1-hour early detection capability, but also may allow astronauts and mission control to predict if an event is likely to be insignificant, which is the most likely outcome. The forecasting potential is limited for poorly connected events with very slow increase in proton intensities. However, these events are less hazardous and now casting can be more useful than forecasting. Based on these observations, it could be possible to build on the Moon a solar particle alert station, with electron current detectors used to predict the arrival and intensity of SPE in about 1 hour (NASA, 2009).

C. Trapped particle radiation

Protons and electrons trapped in the Van Allen belts (trapped radiation) represent an important contribution to radiation exposure in LEO, such as for astronauts on the International Space Station (NCRP, 2000), albeit the GCR are the dominant component to astronaut organ dose equivalents (Cucinotta *et al.*, 2000; Cucinotta *et al.*, 2008). Trapped radiation originates from the interaction of GCR and solar particles with the Earth's magnetic field and the atmosphere. Electrons reach energies of up to 7 MeV and protons up to 600 MeV. A small fraction of heavier ions is also observed, at energies <50 MeV/nucleon; however, because of their limited penetration capacity, they are of no relevance for radiation protection. Charged particles with these energies moving into a dipole field can never enter into inner areas of this field. However, if they are put into this field for any reason, they are restricted to certain positions and cannot escape. They move in spirals along the geomagnetic field lines and are reflected back between the magnetic poles, acting as mirrors (Rodger and Clivelrd, 2008). Different processes contribute to fill in particles into the radiation belt and two main zones of captured particles are observed. The inner belt is mainly formed by decaying neutrons, coming from the atmosphere in which they are produced in cosmic-ray interactions and producing protons and electrons. The outer belt consists mainly of trapped solar particles and is populated mainly by electrons. During disturbances of the magnetosphere by magnetic storms related to SPE where the geomagnetic cutoff is usually depressed particles of lower energies can penetrate from outside toward the inner regions and fill them up. The radiation belts extend over a region from 200 km to about 75 000 km around the geomagnetic equator.

The trapped radiation is modulated by the solar cycle: Proton intensity decreases with high solar activity, while electron intensity increases, and vice versa. Diurnal variations by a factor of between 6 and 16 are observed in the outer electron belt, and short-term variations due to magnetic storms may raise the average flux by 2 or 3 orders of magnitude. The center of the inner belt is quite stable, especially with respect to protons with a slight westward drift observed over time and in some cases transient belts are observed (Badhwar *et al.*, 2002). However, at the lower edge of the belt, electron and proton intensity may vary by up to a factor of 5. For the majority of space missions in LEO, protons deliver the dominant contribution to the radiation exposure inside space vehicles. Because of their higher energies and correspondingly longer range, their total dose surpasses that of electrons at mass shielding above about 0.3 $\mathrm{g/cm^2}$ Al. At lower shielding (e.g., in case of EVA) the absorbed dose is dominated by the electron contribution and may reach up to 10 mSv/day.

Of special importance for LEO is the so-called "South Atlantic anomaly" (SAA), a region over the coast of Brazil, where the radiation belt extends down to altitudes of 200 km. This behavior is due to an 11° inclination of the Earth's geomagnetic dipole axis from its axis of rotation toward Northern America and a 500 km displacement of the dipole center toward the Western Pacific, with corresponding significant reduced field strength values. Almost all radiation received in LEO at low inclinations is due to passages through the SAA (Fig. 10). At an orbit with 28.5° inclination, six orbital rotations per day pass through the anomaly, while nine per day do not. Although traversing the anomaly takes less than about 15 min and occupies less than 10% of the time in orbit, this region accounts for the dominant fraction of total exposure on ISS.

There are several trapped radiation environments available, and the Space Environment Information System (SPENVIS) platform developed by ESA (Heynderickx *et al.*, 2004) implements three proton models and four electron models. SPENVIS is a web-based tool providing space engineers and scientists with information on the space environment and its likely effects on space systems. The NASA AP-8 and AE-8

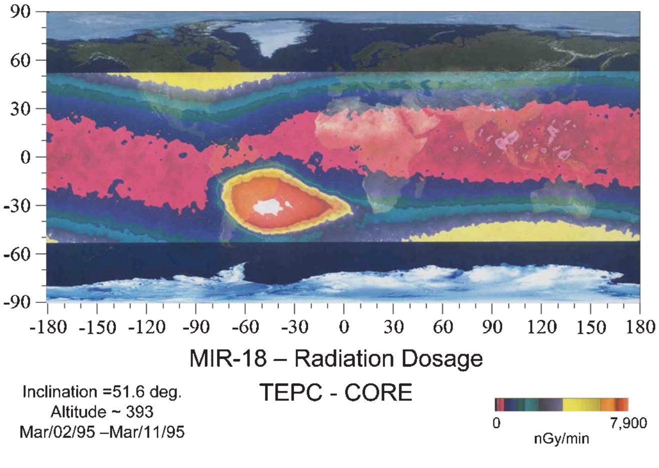

FIG. 10 (color). Space radiation field measured onboard the MIR space station in 1995 using a tissue-equivalent proportional chamber. Image courtesy of Gautam Badhwar (NASA).

radiation belt models (Vette, 1991) are still the standards for engineering applications and are, of course, implemented in SPENVIS. Up to now, the NASA codes are the only models that completely cover the region of the radiation belts and have a wide energy range for both protons (0.1–4600 MeV) and electrons (0.04–7 MeV). The maps are based on data from more than 20 satellites from the early 1960s to the mid-1970s, but a considerable part of the range of the NASA models was achieved by extrapolation.

D. Radiation measurements in spaceflight

1. Particle and neutron spectra in low Earth orbit

The radiation detector systems applied for the monitoring of the radiation environment onboard the ISS can be grouped into two categories. The first category comprises the "operational radiation monitoring devices," i.e., area monitors and personal dosimeters [such as thermoluminescence dosimeters (TLD)] used to measure field quantities and organ or tissue doses to be used for normalizing radiation transport calculations, individual dose assessment and record keeping purposes, and real-time or near real-time estimates of dose rates for purposes of immediate dose management or ALARA.

The second category consists of instruments selected for specific science topics and for limited operation times, typically for one or two increments. These topics are a characterization of the radiation field, such as determination of particle flux and energy spectra for each particle type at different locations and times in the different modules and outside the space station, and influence of shielding material composition and thickness. Presently on ISS there are two Italian silicon strip detectors, ALTEA (Narici, 2008) and ALTEINO (Casolino *et al.*, 2007), a German (DOSTEL) and a Bulgarian (LIULIN) silicon telescope, and a Japanese Bonner ball neutron detector. As a by-product, these instruments deliver data which supplement missing information from the operational systems and thereby increase the reliability of such data substantially. Figure 11 provides an example of LET spectrum measured by DOSTEL (Reitz *et al.*, 2005). A charged particle spectrum measured on ISS by the Sileye-3/ALTEINO instruments is shown in Fig. 12.

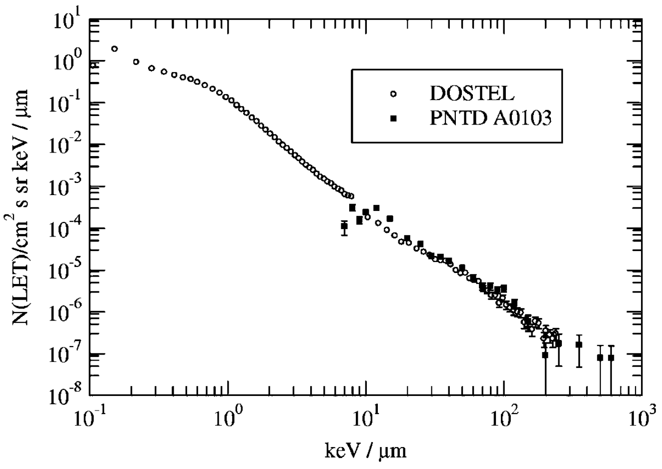

FIG. 11. Comparison of measured LET spectra from DOSTEL and CR-39 nuclear track detectors. From Reitz *et al.*, 2005.

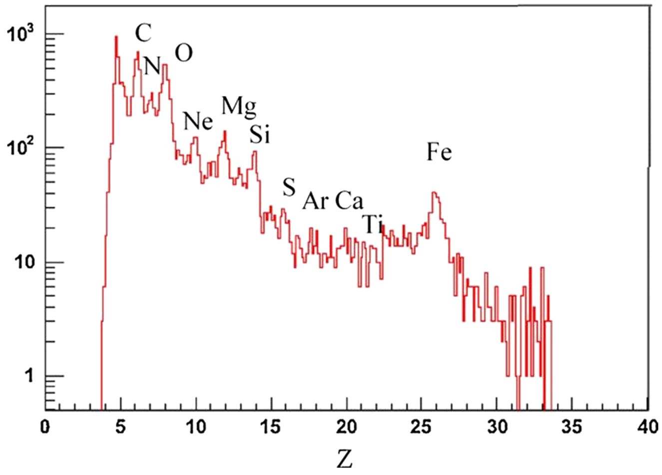

FIG. 12 (color online). Histogram of particle counts showing the nuclear identification capabilities of Sileye-3/ALTEINO from C to Fe in the Pirs module of the ISS (Casolino *et al.*, 2007). The peak at $Z < 6$ is an overlap of different light ions.

Neutron dosimetry is particularly challenging in space flights. Neutrons are produced in nuclear interactions between trapped protons or GCR with the spacecraft walls and the human body. Many neutron detection methods rely on the measurement of charged particle produced by neutrons, which is quite difficult because of the many charged particles of similar energies produced by trapped protons, primary GCR and projectile fragments. They have a very wide energy spectrum extending from thermal neutrons to more than 1 GeV. TLDs have low sensitivity to neutrons. However, chips with ^{6}LiF (TLD600) or ^{7}LiF (TLD700) have almost the same response to γ rays but different response to neutrons. Table IV shows the results of neutron measurements by nuclear emulsions in different shuttle missions (Badhwar, Keith, and Cleghorn, 2001). Recoil proton measurements in nuclear emulsion can measure neutron energy up to about 14 MeV, and data in Table IV suggest that these neutrons contribute about 7% of the absorbed dose, but around 30% of the equivalent dose. The models predict that neutron dose rates of nearly 0.5 mSv/day are possible on the ISS with lower estimates below 0.1 mSv/day. Considering that the charged particle dose rate on the Mir station was between 0.4 and 1 mSv/day, it is clear that neutron contribution can be comparable to the charged particle dose. However, an important complication for neutron dosimetry in space is the possible double counting of secondary radiation. Since neutrons are secondaries from primary protons and heavy ions, and tertiary or higher-order reactions are non-negligible, it is not always clear how the results from different devices can be added. Of note is that ISS astronaut biodosimetry measurements using chromosomal aberrations which has excellent response to neutrons are quite consistent with data from tissue equivalent proportional counter (TEPC) and radiation transport codes, both of which consider charged particles and neutron contributions in a consistent manner (Cucinotta *et al.*, 2008).

Measurements of the neutron energy spectra have also recently been performed with other instruments, for instance, using Bonner balls on ISS (Koshiishi *et al.*, 2007).

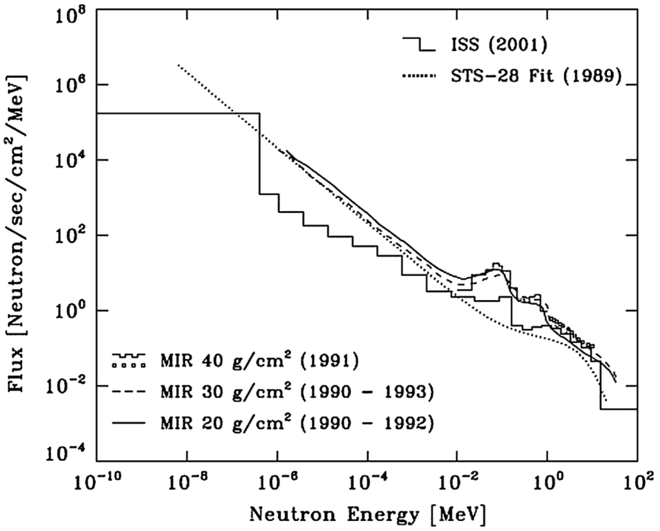

FIG. 13. Comparison of the orbit-averaged neutron spectrum obtained inside the ISS with the neutron measurements inside the other spacecraft; the fitted neutron spectrum evaluated from the measurement inside the STS-28 in 1989, as well as the neutron spectra measured inside the MIR in 1991 under 40 g/cm^2 shielding thickness, from 1990 through 1993 under 30 g/cm^2 shielding thickness, and from 1990 through 1992 under 20 g/cm^2 shielding thickness. From Koshiishi *et al.*, 2007.

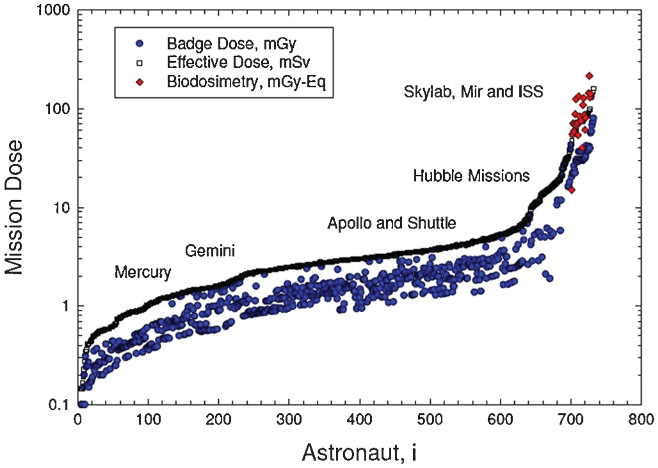

FIG. 14 (color). Summary of mission personnel dosimetry from all past NASA crews. Effective dose and population average biological dose equivalent for astronauts on all NASA space missions, including Mercury, Gemini, Apollo, Skylab, Apollo-Soyuz, Space Shuttle, NASA-Mir, and ISS missions. Biodosimetry data were collected by measurements of chromosomal aberrations in peripheral blood lymphocytes before and after the mission, and comparison with individual calibration curves measured on the ground. From Cucinotta *et al.*, 2008.

Comparison of different measurements on the Space Shuttle, MIR, and ISS is provided in Fig. 13. Comparison between the ISS and the MIR spectra for $E > 1$ MeV displays that the neutron spectrum has higher flux at greater shielding depth, demonstrating that a thicker shield produces more high-energy neutrons, while spectra are similar at low energy. However, the ISS spectrum has a much lower total flux than MIR even though the shielding is similar. The discrepancy is likely to be due to the different instruments used: Bonner ball neutron detectors on ISS and nuclear emulsions on MIR and the Space Shuttle. The results suggest that the data in Table V should be taken with some caution, and precise measurements of neutron spectra and fluxes are still needed.

Figure 14 gives a summary of the effective doses received by NASA astronauts during various space flights (Cucinotta *et al.*, 2008). Roughly 50% of the absorbed dose is caused by trapped protons and 50% by GCR (Benton and Benton, 2001), whereas only 20% of the effective dose is attributable to trapped protons (Cucinotta *et al.*, 2008). The effective doses vary with altitude and inclination for each flight. The highest values were observed during the high altitude shuttle flights at low inclinations with up to 4 mSv/day and during the Apollo program with about 3 mSv/day. The radiation fields responsible for this exposure are quite different.

2. Organ doses

Measurements of the effective dose by Eq. (2) require knowledge of the doses in different organs. Excess relative risks for radiation-induced cancers from atomic-bomb survivors are based on bone marrow doses (about 79% of the skin dose) for leukemia and colon dose (about 67% of the skin dose) for solid cancers (ICRP, 2007). The recommended career limits for activities in LEO (Table III) refer to effective doses, which must be estimated from personnel dosimetry combined with radiation transport codes (NCRP, 2002). Only the skin dose is measured in all astronauts by TLD. The use of phantom measurements can improve effective dose estimates but ultimately cannot represent the movements of individual astronauts within a complex spacecraft.

Organ doses have been calculated by NASA using computerized anatomical models (CAM) (Billings, Yucker, and Heckman, 1973; Atwell, 1994). The CAM man model

TABLE V. Comparison between dose and dose equivalents for neutrons and charged particles in four different STS missions at 28.5° inclination in LEO. Neutron dose was measured by nuclear emulsions and charged particle dose by TLD-100 detectors (Badhwar, Keith, and Cleghorn, 2001).

Mission	Altitude (km)	Neutron dose rate (μGy/day)	Charged particle dose rate (μGy/day)	Neutron equivalent dose rate (μSv/day)	Charged particle equivalent dose rate (μSv/day)
STS-55	302	5.9	57.2	52.0	120.1
STS-57	470	25.3	461.9	220.0	859.4
STS-65	306	11.0	75.2	95.0	157.8
STS-94	296	3.7	101.5	30.8	213.9

represents a 50th percentile U.S. Air Force male. The computerized anatomical female model has been obtained by removing male organs and incorporating female organs and taking into account the smaller stature of the woman. In the 10-day STS-91 mission (June 1998), organ doses were measured using 59 chips (TLD plus the plastic nuclear track detector) positioned into a life-size human phantom torso, made of tissue-equivalent resin and including a skeleton (Badhwar *et al.*, 2002). The effective dose E [Eq. (2); tissue weighting factors are provided in Table I] was 4.1 mSv, which is approximately 90% of the skin equivalent dose. Bone marrow and colon equivalent doses were less than 80% of the skin equivalent dose. A phantom still onboard ISS is MATROSHKA (Fig. 15). MATROSHKA (Reitz *et al.*, 2009) is designed as an anthrophomorphic upper torso phantom, with 33 slices, each 25 mm in thickness. A base structure houses the electronic boxes for data acquisition and data transmission of the internal temperature and pressure as well as the active radiation detector sensors. A carbon fiber container with a mass density of ~ 0.5 g/cm^2 simulates the shielding distribution of an astronauts EVA suit. The phantom torso is equipped with TLD placed in 354 polyethylene tubes, which are accommodated in the 33 slices, enabling determination of the absorbed dose and depth-dose distribution at 800 measurement points in a 2.5 cm x-y-z grid. Combination of TLD and nuclear track etch detectors are assembled in polyethylene boxes ($60 \times 40 \times 25$ mm) at selected organ locations (eye, lung, stomach, kidney, and intestine) as well as in a Nomex-made travel poncho. For the determination of the skin dose detectors are sewed into polyethylene stripes directly on the skin surface. Seven active radiation detector monitors are distributed in the simulated organ regions $-5\times$ silicon detectors for determination of the heavy ion and neutron component and one silicon telescope (DOSTEL) is located on top of the head of the phantom. MATROSHKA uses therefore more than 6000 detectors. The MATROSHKA project started in January 2004 and has experienced from that time on three exposures of detector sets onboard the ISS: one outside exposure (MTR-1) and two inside exposures (MTR-2A and MTR-2B). In its third exposure phase (MTR-2B) the MATROSHKA facility was stored inside the Russian Zvezda module from October 2007 until November 2008. Measurements for MTR-2 phase B were performed with passive and active radiation detectors. Results from MTR-1 (Fig. 15) show a reduction in the dose in the internal organs, due to the body self-shielding, which is though paralleled by an increase in the quality factor (Reitz *et al.*, 2009). For instance, the skin dose is about 0.94 mGy/day, but it is reduced to 0.2 mGy/day in the stomach. However, the quality factor increases from 1.7 to 2.5, and therefore equivalent dose rates are 1.6 and 0.6 mSv/day, respectively.

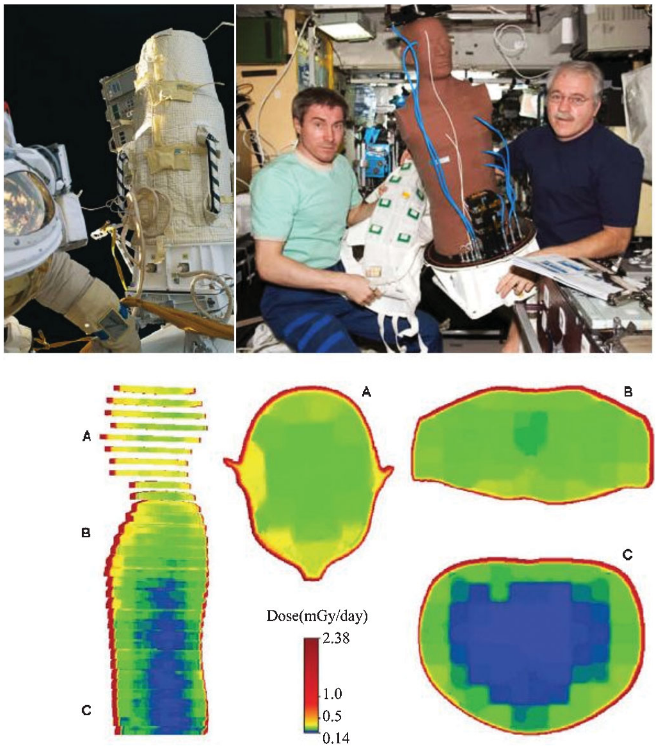

FIG. 15 (color). MATROSHKA on ISS: The MATROSHKA experiment facility (upper left panel) was installed on the outside of the ISS on 27 February 2004 to measure radiation doses that astronauts experience during EVA activities. The phantom and its radiation detectors were brought back inside the ISS on 18 August 2005 as part of Expedition 11 EVA activities: ISS Expedition 11 Commander Sergei Krikalev (left) and Flight Engineer John Phillips (right) dismantle the phantom and remove the passive detector systems for return to Earth (upper right panel). Since then, MATROSHKA is measuring doses to different organs, using active and passive detectors, and different shielding materials covering the torso inside of the ISS. Bottom: The median-saggital plane of the 3D of MATROSHKA including "skin dose" distribution (Reitz *et al.*, 2009). 2D dose distributions for a slice of the head, the shoulder region and the lower torso (the whole phantom consists of 33 slices, each 25 mm thick loaded with dosimeters). These results are based on dose values measured inside the phantom and directly on the skin by thermoluminescence dosimeters. This represents the dose distribution in an outside exposure. Graphics courtesy of Günther Reitz (DLR).

3. Radiation detectors for exploratory-class missions

There are no measurements of the radiation environment on planetary surfaces such as the Earth's Moon and Mars. Recent measurements in the Moon orbit were performed by the RADOM spectrometer in the Chandrayaan-1 Indian lunar orbiter (Dachev *et al.*, 2009) and are currently ongoing on the NASA LRO mission (Fig. 1) with two dedicated instruments. The cosmic ray telescope for the effects of radiation (CRaTER) instrument is designed to characterize the global lunar radiation environment and its biological impacts (Spence *et al.*, 2010). CRaTER is an LET spectrometer, consisting of three pairs of thin and thick silicon detectors surrounding two pieces of tissue-equivalent plastic and will measure the spectrum in a very broad range, with a lower limit in energy around 10 MeV. The lunar exploration neutron detector (LEND) instrument measures the neutron emission flux from the entire lunar surface (Mitrofanov *et al.*, 2010). LEND measures thermal, epithermal, and high-energy neutrons up to about 15 MeV, which are produced by spallation of GCR nuclei with the lunar regolith. To satisfy the LRO mission measurement requirements, LEND includes four high pressure ^{3}He proportional counters and an organic crystal scintillator within the collimation module, covered with polyethylene and $^{1}0$B. The radiation environment in the Mars orbit was measured by the Martian radiation environment experiment (MARIE) telescope onboard Mars Odyssey, the robotic spacecraft launched in April 2001 and still in orbit around Mars (Badhwar, 2004). MARIE collected data during Odyssey's cruise and operated in orbit around Mars until the large SPE on 28 October 2003 well beyond the mission requirement of 90 days of data collection. MARIE has been unable to collect data since that time. As the Earth and Mars are often out of phase, SPEs at Mars can be connected from solar disturbances from different regions of the Sun, or from event propagating from distinct magnetic field lines than Earth, thus complicating Earth based forecasts of Mars events. MARIE observed 14 events from 2001 to 2003 (Cleghorn *et al.*, 2004), many of which were not observable from Earth and others that were, however, revealing different characteristics from Mars. After the demise of MARIE in October 2003, a neutron detector on the Odyssey spacecraft continued to make observation of enhanced count rates at Mars (Zeitlin *et al.*, 2010), which allowed further tests of predictive models of SPE propagation.

It can be concluded that radiation monitoring in future interplanetary missions will not be substantially different from the current situation on ISS. In its recent recommendations on future radiation studies for exploration (NCRP, 2006), NCRP has listed five topics in the area of dosimetry and detectors:

- validation of radiation transport models,
- characterization of instruments able to provide microdosimetric spectra, particularly tissue-equivalent proportional chambers (TEPC),
- voxel and physical phantoms for the estimates of the effective dose,
- development of spectrometers able to detect indirect ionizing radiation under intense fluxes of charged particles,
- and measurements of neutron production in fragmentation processes and neutron interaction cross sections.

III. SPACE RADIATION TRANSPORT

The description of the passage of high-energy particles through matter can be made using Boltzmann-type transport equations that treat the atomic and nuclear collisions that alter particle energy and types. As an alternative, Monte Carlo (MC) computer codes sample from interaction processes for individual primaries or their secondary's to develop histories of charged particle passage and energy deposition in materials. NASA has developed a Boltzmann equation approach for HZE nuclei transport denoted as the HZETRN code (Wilson *et al.*, 1991), and coupled light ion-HZE transport also solved with this method. The HZETRN code with the quantum fragmentation multiple-scattering model (QMSFRG) cross sections (Cucinotta, Kim, and Ren, 2006; Cucinotta *et al.*, 2007) agrees with spaceflight measurement of organ dose equivalent to within ±20% (Cucinotta *et al.*, 2000; Cucinotta *et al.*, 2008). The Boltzmann equation is a deterministic description of particle transport. The HZETRN code with broad energy beam boundary conditions and the related GREENTRN code with narrow energy beam or monoenergetic boundary conditions (Wilson *et al.*, 1991, 1995; Tweed, Wilson, and Tripathi, 2004) calculate the average flux of each particle at different depths in shielding. These codes have been well validated by space measurements in LEO or accelerator measurements where good agreement is found. Recent extensions of the code have added multigroup methods for bidirectional neutron transport and improved convergence methods (Clowdsley *et al.*, 2001; Slaba *et al.*, 2010) and the addition of pion transport coupled to the GCR sources (Blattnig *et al.*, 2004). Earlier versions of the HZETRN code (Wilson *et al.*, 1991) considered only a reduced isotopic grid of 59 particles. In recent years the HZETRN code considered a complete isotopic grid including the isotopic composition of the source particles (Cucinotta *et al.*, 2006b), and to consider light ion production through nuclear coalescence (Cucinotta *et al.*, 2007). Complex spacecraft geometries are handled using ray tracing techniques to represent thousands of spacecraft parts albeit in a bidirectional transport.

Monte Carlo codes such as GEANT4 (Agostinelli *et al.*, 2003), PHITS (Niita *et al.*, 2006), FLUKA (Battistoni *et al.*, 2008), HETC-HEDS (Townsend, Miller, and Gabriel, 2005), and MCNPX (James *et al.*, 2006; Aghara *et al.*, 2009) have been used for accelerator and atmospheric radiation studies and more recently for space applications. The MC approach allows for very detailed considerations on detector designs and background events in high-energy experiments to be considered. In principle, more complicated geometries can be considered in the MC approach compared to the HZETRN code because angular scattering of particles is considered; however, in practice simplified geometries have been used by MC codes to represent complex spacecraft geometries, such as cylinders of appropriate dimensions and composition. Many MC transport codes include modules to treat low-energy neutron and photon transport that were originally developed as a reactor design such as the MORSE code. There are quite a few nuclear models utilized within the different MC codes, including commonalities with nuclear models used in the HZETRN codes, which we discuss below. What often is overlooked is that the MC codes have the ability to evaluate stochastic events (Cucinotta *et al.*, 2011); however, in most space radiation applications, the MC codes have reported only on the calculation of average quantities such as fluence, dose, and dose equivalent, and very few analyses of the importance of fluctuations are described.

Space radiation problems are not likely handled with a one-size fits all approach and the specific application drives the method to be used. One aspect of codes that can be standardized is the nuclear interaction models including developing methods of cross comparisons of distinct transport codes. Computational speeds are optimized if data libraries for cross sections are stored and called from data files in programs, rather than including the actual calculation procedure for cross sections within the transport code in order to reduce CPU times. Other considerations are the angular dependence of the reactions. For example, heavy ions above 100 MeV/nucleon travel predominantly in the forward direction and there is only a minor need to evaluate angular deflections for the omnidirectional fields in space. For lower energy heavy ions, atomic collisions dominate which are well described by multiple-scattering and straggling distributions.

On the other hand, neutrons are created by several physical processes that have distinct angular production characteristics. Light charged particles will have behaviors intermediate to neutrons and heavy ions, and the roles of angular deflections for space applications require further study.

A. Particle and heavy ion transport calculations

1. Deterministic codes

The relevant transport equations are derived on the basis of conservation principles (Wilson *et al.*, 2001) for the flux density $\phi_j(x, \Omega, E)$ of type j particles as

$$\begin{aligned}\Omega \cdot \nabla\phi_j(x, \Omega, E) &= \sum_k \int \sigma_{jk}(\Omega, \Omega', E, E')\phi_k(x, \Omega', E')dE'd\Omega' \\ &\quad - \sigma_j(E)\phi_j(x, \Omega, E),\end{aligned} \tag{14}$$

where $\sigma_j(E)$ and $\sigma_{jk}(\Omega, \Omega', E, E')$ are the media macroscopic cross sections. The $\sigma_{jk}(\Omega, \Omega', E, E')$ represent all those processes by which type k particles moving in direction Ω' with energy E' produce a type j particle in direction Ω with energy E. The flux density $\phi_j(x, \Omega, E)$ is the main physical quantity used to determine the physical or biological response by folding it with an appropriate response function for the physical or biological system under study.

There may be several reactions which produce a particular product, and the appropriate cross sections for Eq. (14) are the inclusive ones. The total cross section $\sigma_j(E)$ with the medium for each particle type of energy E may be expanded as

$$\sigma_j(E) = \sigma_j^{\mathrm{at}}(E) + \sigma_j^{\mathrm{el}}(E) + \sigma_j^{\mathrm{r}}(E), \tag{15}$$

where the first term refers to collision with atomic electrons, the second term is for elastic nuclear scattering, and the third term describes nuclear reactions. The microscopic cross sections and average energy transfer are ordered as follows:

$$\begin{aligned}\sigma_j^{\mathrm{at}}(E) &\sim 10^{-16}\ \mathrm{cm}^2 \quad \text{for } \delta E_{\mathrm{at}} \sim 10^2\ \mathrm{eV}, \\ \sigma_j^{\mathrm{el}}(E) &\sim 10^{-19}\ \mathrm{cm}^2 \quad \text{for } \delta E_{\mathrm{el}} \sim 10^6\ \mathrm{eV}, \\ \sigma_j^{\mathrm{r}}(E) &\sim 10^{-24}\ \mathrm{cm}^2 \quad \text{for } \delta E_{\mathrm{r}} \sim 10^8\ \mathrm{eV}.\end{aligned} \tag{16}$$

This ordering allows flexibility in expanding solutions to the Boltzmann equation as a sequence of physical perturbative approximations (Wilson *et al.*, 2001). Many atomic collisions ($\sim 10^6$) occur in a cm of ordinary matter, whereas $\sim 10^3$ nuclear Coulomb elastic collisions occur per cm. In contrast, nuclear reactions are separated by a fraction to many cm depending on energy and particle type. For neutrons, $\sigma_n^{\mathrm{at}}(E) \sim 0$ and the nuclear elastic process appears as the first-order perturbation. Mean free paths for elastic scattering of neutrons may become quite small, especially at low energies in the resonance region (ICRU, 2000).

The solution of Eq. (14) involves hundreds of multidimensional integro-differential equations which are coupled together by thousands of cross terms and must be solved self-consistently subject to boundary conditions ultimately related to the external environment and the geometry of the astronaut's body and/or a complex vehicle. A series of approximate solutions can be studied and indicates a high level of accuracy for most applications (Wilson *et al.*, 2001; Tweed, Wilson, and Tripathi, 2004). The mean energy loss can be introduced in a continuous slowing down approximation (CSDA). The highly directional Coulomb cross section for charged ions and nuclear elastic scattering for neutrons generally dominate the second perturbation term. The angular dispersion and its effects on lateral beam spread and range straggling are important corrections in comparing to laboratory measurements. The nuclear elastic scattering is especially important to neutron fields and has been treated in the past using Monte Carlo methods or multigroup methods (Hughes, Prael, and Little, 1997). The third perturbation term consists of complex energy and angle functions. Results from Monte Carlo codes (Alsmiller *et al.*, 1965) provided the basis for the generation of analytical techniques and the simplification of boundary conditions used in space shield code development (Wilson *et al.*, 1991).

For transport of the GCR heavy ions ($A > 4$), the use of the CSDA in a marching procedure has been implemented in NASA's HZETRN code (Wilson *et al.*, 1991). For GCR transport, an isotopic grid of more than 150 ions is needed to represent all the possible fragments produced with 190 ion uses in the HZETRN code (Cucinotta, Kim, and Ren, 2006). For monoenergetic beam transport, a Gaussian model of the fragment single differential cross section has been considered along with energy straggling using a Green's function approach (Tweed, Wilson, and Tripathi, 2004). For light particle transport, the broad redistribution in energy of the ions in collisions is considered in the marching procedure (Wilson *et al.*, 1991). Angular effects for neutron transport are considered using a multigroup or Monte Carlo transport models (Hughes, Prael, and Little, 1997).

2. Transport coefficients

The transport coefficients describe the atomic, molecular, and nuclear processes by which the particle fields are modified by the presence of a material medium (Wilson *et al.*, 2001). As such, basic atomic and nuclear theories provide the input to the transport code databases. The first-order physical perturbation on the right-hand side of Eq. (14) is the atomic and/or molecular cross sections as noted in Eq. (16) for which those terms in Eq. (14) are expanded about the energy moments as

$$S_n(E) = \sum_i \varepsilon_i^n \sigma_i(E), \tag{17}$$

where ε_i is based on the electronic excitation energy, and $\sigma_i(E)$ is the total atomic and/or molecular cross section for delivering ε_i energy to the orbital electrons (including discrete and continuum levels). The first moment ($n = 1$) is the usual stopping power, and the usual CSDA is achieved by neglecting the higher-energy moments.

In Eq. (17) specification of ε_i and $\sigma_i(E)$ requires complete knowledge of the atomic and molecular wave functions. Stopping power databases are derived semiempirically as the Bethe reduction of Eq. (17) in terms of mean excitation energies and shell corrections (Fano, 1963; Wilson *et al.*, 1991). The stopping power S is adequately described by the Bethe-Bloch formula for most ion energies (Bichsel, 1992):

$$S = \frac{4\pi Z_P^2 Z_T N_T e^4}{m\nu^2}\left\{\ln\left(\frac{2mc^2\beta^2\gamma^2}{I}\right) - \beta^2 - \frac{C(\beta)}{Z_T} + Z_P L_1(\beta) + Z_P^2 L_2(\beta) + L_3(\beta)\right\}, \tag{18}$$

where e is the electronic charge, N_T is the density of target atoms, m is the mass of the electron, c is the speed of light, $\beta = \nu/c$, and I is the mean excitation energy. In Eq. (18), the various terms are the shell correction $C(\beta)$, Barkas correction $L_1(\beta)$, Bloch term $L_2(\beta)$, and Mott and density corrections $L_1(\beta)$. The range of the ion is evaluated from the stopping power as

$$R(E) = \int_0^E \frac{dE'}{S(E')}. \tag{19}$$

The second energy moment is related to energy or range straggling and provides corrections to the ion slowing down spectrum (Fano, 1963). Straggling has been well studied for ion beam applications with leading order and most higher-order correction terms well understood. For broad beams conditions of GCR transport straggling effects are negligible; however, they are important for laboratory studies with monoenergetic beams and for understanding radiation detector responses. The next physical perturbation term is the Coulomb scattering by the atomic nucleus and is typically represented by Rutherford scattering modified by screening of the nuclear charge by the orbital electrons using the Thomas-Fermi distribution for the atomic orbits. The total nuclear Coulomb cross section found by integrating over the scattering directions is related to the radiation length. The differential cross section is highly peaked in the forward direction, and only after many scatterings is significant beam divergence seen. Numerical solutions to the Coulomb multiple-scattering problem have been investigated for many years (Fermi, 1940) and accurately describe experimental data with HZE (Wong et al., 1990) or proton beams (Carlsson and Rosander, 1973).

For determining the particle spectra, numerical techniques have been developed which allow for computationally efficient and accurate computer codes in the straightforward approximation (Wilson et al., 1995). In this model the heavy ion flux $\phi_j(E, x)$ of an ion j with mass number A_j, charge number Z_j, and energy E (in units of MeV/nucleon) at shielding depth x (in units of g/cm^2) is determined by the partial differential equation (Wilson et al., 1991)

$$\left[\frac{\partial}{\partial x} - \frac{1}{S_j(E)}\frac{\partial}{\partial E} + \sigma_j(E)\right]\phi_j(x, E) = \sum_k \sigma_{j,k}(E)\phi_k(E, x), \tag{20}$$

where $\sigma_j(E)$ is the energy-dependent absorption cross section (cm^{-1}) and $\sigma_{j,k}(E)$ is the fragmentation cross section for producing an ion j from k. The solution to Eq. (20) in the HZETRN code is found using the methods of characteristics where the coordinate transformation from depth and particle range $R_j(E)$ are defined

$$\eta_j = x - R_j(E), \qquad \xi_j = x + R_j(E), \tag{21}$$

and the scaled flux

$$\chi_j(\eta_j, \xi_j) = S_j(E)\phi_j(x, E) \tag{22}$$

is introduced leading to the transport equation

$$\left[2\frac{\partial}{\partial \eta_j} + \sigma_j\right]\chi(\eta_j, \xi_j) = \sum_k \sigma_{j,k}\frac{\nu_j}{\nu_k}\chi(\eta_k, \xi_k), \tag{23}$$

where $S_j(E)$ is the stopping power of ion j, $\nu_j = Z_j^2/A_j$, σ_j is the total absorption cross section, and σ_{jk} is the fragmentation cross section to produce isotope j from projectile isotope k. The solution of the transport equation for light ions and neutrons is distinct from Eq. (23) because of the broad redistribution of energy in collision events as described by Wilson et al. (1991).

3. Monte Carlo codes

There are several MC codes that have been developed for accelerator applications in detectors and therapy with high-energy charged particles (Durante and Bruno, 2010; Schardt, Elsässer, and Schulz-Ertner, 2010), and more recently medical and space applications. These codes often differ by nuclear interaction models used and scoring and geometry approaches. The FLUKA (fluctuating kascade) code transports various charged particles including heavy ions, neutrons, electrons, and photons up to 10^4 TeV for all particles and down to thermal energies. Particle interactions are scored on a 3D mesh for event-by-event histories or performing user specified averages. HETC-HEDS is a NASA developed extension for the former NASA human exploration and development of space (HEDS) efforts of the HETC (high-energy transport code) originally developed at Oak Ridge National Laboratory. PHITS (particle and heavy ion transport code system) is a MC code developed in Japan that treats with all particles up to 200 GeV/nucleon, and incorporates the MCNP code for low-energy neutron and photon transport. GEANT4 (geometry and tracking code) is an MC code developed at CERN for accelerator and detector applications.

The MC approach allows more flexibility compared to deterministic codes for introducing new applications of interest, such as particle transport in magnetic fields, and three-dimensional aspects that would be prohibitive to solve in an analytic approach. Nuclear interaction considerations in the various codes are described below. There are distinctions in how different MC codes treat complex geometries compared to deterministic codes, and much longer CPU times are needed for MC codes making them prohibitively time consuming for spacecraft shielding design studies. Many of the MC codes provide training and support functions through international collaborations.

B. Nuclear interaction cross sections

The types of cross sections required for transport involve total yields and multiplicities and inclusive secondary energy spectra for one-dimensional transport or inclusive double-differential cross sections in angle and energy for three-dimensional transport. For Monte Carlo simulations, exclusive cross sections may be needed for computer algorithms, an enormous construction task when one considers the large number of projectile-target combinations, secondary multiplicities, etc. needed to transport all GCR particles and energies through spacecraft and tissues. Fortunately, physical considerations lead to great simplifications allowing inclusive cross sections to be appropriate for most applications. Low-energy evaporation products including heavy ion target fragments are high LET events. Knockout products from proton or neutron reactions and projectile fragments from GCR nuclei are typically of low to moderate LET; however, their large ranges lead to radiation buildup through further reactions.

1. Nuclear fragmentation models

Three types of nuclear fragmentation models have been developed to consider heavy ion fragmentation cross sections. The first type uses the multiple-scattering series approach of Watson (1953) and high-energy approximations in a quantum multiple-scattering approach. The second approach is the intranuclear cascade (INC) models, originally developed by Metropolis, Bertini, and others at Oak Ridge, and in recent years the Liege INC model developed by Cugnon, and one based on the patron model for the ultrarelativistic case called JAM for jet-AA microscopic transport model. A third approach is the molecular dynamics model (QMD), which is a semiclassical model using Gaussian wave packets and Newtonian equations, and the related Japanese quantum molecular dynamics model used by the PHITS code. Each of these models relies on the two-step picture, called cascade and evaporation, or abrasion and ablation to describe the interaction. The description of nuclear reactions through abrasion (particle removal during ion-ion interaction) and ablation (nuclear deexcitation after the abrasion step) is illustrated in Fig. 16, which shows the roles of projectile overlap, fireball formation in central regions, and the decay of the prefragment spectators. Peripheral collisions lead to small mass removal, while central collisions can lead to the total destruction of the two nuclei. Ablation applies best to peripheral collisions where the remaining nuclei after the collision called the projectile or large prefragment are left in a state of excitation and will decay to the ground state by statistical emission of light particles and γ rays.

The models developed at NASA rely on the quantum multiple-scattering theories (QMST), which are solved to calculate the probability of abrading n nucleons, and to evaluate the excitation spectra of the prefragments. The multiple-scattering series of Watson (1953) for proton-nucleus scattering was extended to the nucleus-nucleus case by Wilson (1974) and forms the basis for considering the elastic channel for determination of the total absorption cross section, and the development of models for the various inelastic channels including nuclear abrasion where the Glauber model (Czyz and Maximon, 1969; Glauber, 2006) is useful (Hufner, Schafer, and Schurmann, 1975). The equations of motion for nuclear scattering are expressed in terms of the transition operator which represents an infinite series for the multiple scattering of the constituents of the projectile and target nucleon. The strong nature of the nuclear force requires a nonperturbative solution to the scattering problem. In relativistic field theory, the non-Abelian nature of the strong force has precluded a formulation of the transition matrix for nuclear scattering using the Lagrangian of quantum chromodynamics (QCD). A relativistically covariant formulation of the problem has been developed by Maung and co-workers using meson exchange theory (Maung, Norbury, and Kahana, 1996). The basic approach, in both relativistic and nonrelativistic multiple-scattering theories, is to resum the multiple-scattering series, which is expressed in terms of the irreducible and reducible exchange diagrams in the relativistic multiple-scattering theory (RMST) or the nuclear potential in the NRMST, in terms of the transition matrix for the constituents of the projectile and target nuclei. This avoids having to deal directly with the highly singular behavior of the nuclear potential at short distances, and instead the constituent transition matrix is used, which is often known from experimental determinations.

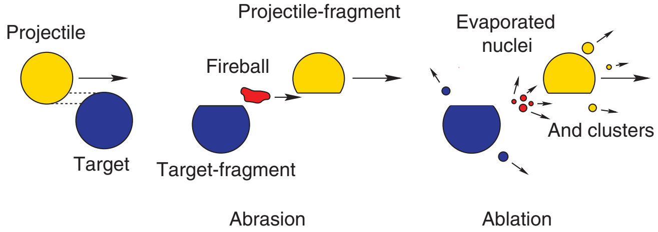

FIG. 16 (color). Illustration of the abrasion-ablation model.

The NRMST is obtained by approximating the full Green's function by the leading order term corresponding to one-meson exchange diagrams and using a nonrelativistic reduction of the three-dimensional Green's function. The potential term is then the sum of the interactions of the constituents (Wilson, 1974)

$$V = \sum_{j=1}^{A_P} \sum_{a=1}^{A_T} \tau_{\alpha j} \tag{24}$$

and the nonrelativistic Green's function is given by

$$g_{\mathrm{NR}} = (E - H_P - H_T)^{-1}, \tag{25}$$

where H_P and H_T are the projectile and target internal Hamiltonians, respectively. At high energies the impulse approximation is invoked, which assumes that the relative kinetic energy of the constituents is much larger than the binding energies such that the propagator is given by

$$g_0 = (E - T_P - T_T)^{-1} \tag{26}$$

and the constituent interactions are replaced by the free interactions which are truly of the two-body form. For high-energy reactions, the scattering is often confined to the forward direction. Here the eikonal approximation is useful for reducing the scattering problem to a closed form expression, which reduces the MST to the form of the Glauber model (Czyz and Maximon, 1969; Wilson, 1974; Glauber, 2006), where cancellation of reflection terms occurs, where nucleons from the projectile and target can rescatter.

2. Elastic and inelastic channels

Knowledge of the elastic amplitude alone is used to determine the total and absorption cross section. The absorption cross section is the key parameter used by MC transport codes to determine if an interaction has taken place in developing Monte Carlo histories. The total (TOT) cross section is found from the elastic amplitude $f(q)$ by using the optical theorem:

$$\sigma_{\mathrm{TOT}} = \frac{4\pi}{k}\,\mathrm{Im} f(\mathbf{q} = 0). \tag{27}$$

The absorption cross section is then found as the difference between the total and elastic cross sections

$$\sigma_{\mathrm{ABS}} = \sigma_{\mathrm{TOT}} - \sigma_{\mathrm{EL}}, \tag{28}$$

where σ_{EL} is the total elastic cross section, and σ_{ABS} is the total absorption cross section. The absorption cross sections are accurately represented by energy-dependent variants (Townsend and Wilson, 1986) of the Bradt-Peters equation (Bradt and Peters, 1950)

$$\sigma_{\mathrm{ABS}} = \pi r_0^2 c_1(E)[A_P^{1/3} + A_T^{1/3} - c_2(E)]^2, \tag{29}$$

where r_0, $c_1(E)$, and $c_2(E)$ are parameters. Figure 17 shows results from experiments for several projectiles on aluminum targets versus the projectile energy. Absorption cross sections have been well studied both experimentally and theoretically and are known with a few percent accuracy (Tripathi, Wilson, and Cucinotta, 2001). Tripathi, Wilson, and Cucinotta (2001) made extension of Eq. (29) to represent most available data and this model is used by GEANT4, PHITS, and HZETRN codes.

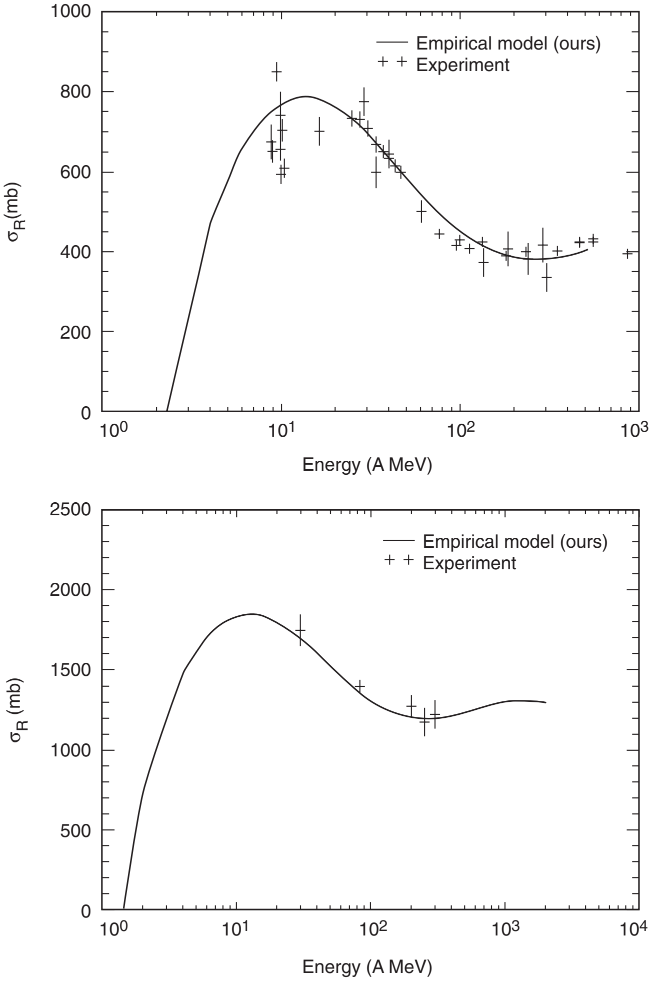

FIG. 17. Comparison of experimental data for p-Al (upper panel) or C-Al (lower panel) absorption cross sections to the theoretical model of Tripathi, Wilson, and Cucinotta (1998).

3. Light ion interactions

For proton or neutron induced knockout of nucleons or light clusters and the fragmentation of light nuclei, such as cosmic-ray helium, the multiple-scattering series is written in a three-body form in order to include the effects of final state interactions (FSI) in the formalism, which was developed for the HZETRN code (Cucinotta, Townsend, and Wilson, 1992; Cucinotta and Dubey, 1994; Cucinotta *et al.*, 1996). An alternate approach would be to consider a distorted wave form for knocked-out particles. The three-body approach of the Faddeev formalism (Faddeev, 1956) allows for a convergent series if the transition matrix for the light particles incident on nuclei is known. The leading order terms to the knockout series are represented by overlap functions for the virtual decay of the nucleus into the participant and spectator, and the quasielastic scattering of the participants. For heavy ions the overlap functions are represented by single particle wave functions.

The transition matrix for the reaction $P + T \to a + b + X$ can be written as a three-body problem of $a - T$, $b - T$, and $a - b$ interactions when rearrangement channels are neglected and with the understanding that all target final and intermediate states must be summed. Using the Faddeev method leads to a multiple-scattering series generated by a coupled set of integral equations (Cucinotta, Townsend, and Wilson, 1992)

$$\tilde{\mathcal{T}} = \tilde{\mathcal{T}}_{aT} + \tilde{\mathcal{T}}_{bT} + \tilde{\mathcal{T}}_{ab}, \tag{30}$$

where $\tilde{\mathcal{T}}_{aT}$, $\tilde{\mathcal{T}}_{bT}$, and $\tilde{\mathcal{T}}_{ab}$ are the cluster amplitudes which are the transition operators for aT, bT, and ab scattering, respectively, in the projectile-target Hilbert space and G_0 is the Green's function in the impulse approximation. The leading order corrections to the pole approximation are found by truncating Eq. (30) as

$$\begin{aligned}\tilde{\mathcal{T}} = (1 + \tilde{\mathcal{T}}_{ab}G_0)(&\tilde{\mathcal{T}}_{aT} + \tilde{\mathcal{T}}_{bT} + \tilde{\mathcal{T}}_{aT}G_0\tilde{\mathcal{T}}_{bT} \\ &+ \tilde{\mathcal{T}}_{bT}G_0\tilde{\mathcal{T}}_{aT})\end{aligned} \tag{31}$$

and replacing $\tilde{\mathcal{T}}_{aT}$ and $\tilde{\mathcal{T}}_{bT}$ by their on-shell values. Equation (31) allows for all orders of multiple scattering, however, assuming the dominance of the ab cluster in the projectile and that ab FSI occur only after interactions with the target. Comparison of the light ion breakup model to experiment for ^{3}H production α-^{12}C reactions is shown in Fig. 18. The MST has been applied to α-particle knockout, as well as to the knockout of nucleons from target nuclei by incident nucleons.

Evaluation of the inclusive cross sections for the α-particle breakup or light particle knockout from nucleon induced reactions involves the quasielastic scattering of the fragments (Cucinotta and Dubey, 1994; Cucinotta, Townsend *et al.*, 1996). For different reactions, the identity of secondaries may be the same (e.g., for p and n production) and quasielastic scattering of the incident nucleon (p or n) may overlap with the knockout distribution. These individual contributions are written as

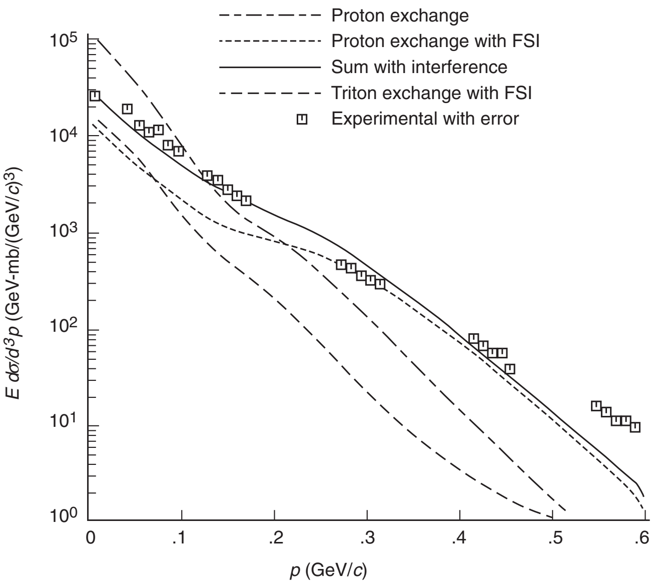

FIG. 18. Transverse momentum distributions for ^{4}He fragmentation on C target into tritons at 1.9 GeV/nucleon. From Cucinotta, Townsend, and Wilson, 1992.

$$\left(\frac{d\sigma}{d\mathbf{p}}\right)_{p,n} = \left(\frac{d\sigma}{d\mathbf{p}}\right)_{\mathrm{K.O.}} + \left(\frac{d\sigma}{d\mathbf{p}}\right)_{\mathrm{QE}} + \left(\frac{d\sigma}{d\mathbf{p}}\right)_{\mathrm{EVAP}}, \tag{32}$$

where we also included a contribution from the decay of highly excited target recoils. Coalescence of light nuclei also should be considered for AA collisions. The quasielastic terms may have a contribution from charge-exchange or nucleon resonances.

In the abrasion-ablation models (Hufner, Schafer, and Schurmann, 1975; Townsend and Wilson, 1986; Wilson, Tripathi *et al.*, 1995; Cucinotta *et al.*, 1998; Cucinotta, Wilson *et al.*, 2006) used to describe heavy ion fragmentation cross sections the abrasion and ablation processes are largely treated as independent processess only linked by the excitation energies of the prefragments at the end of the abrasion stage. The individual steps of abrasion and ablation can be described in both semiclassical and quantum mechanical approaches. Nuclear database development has focused largely on QMST or Monte Carlo approaches to nuclear reactions using an intranuclear cascade model.

For high energies and increasing charge of the projectile and targets, electromagnetic dissociation can lead to the knockout of neutrons, protons, and light nuclear clusters. The virtual photons created by the electromagnetic field of the two nuclei are the cause of this phenomenon. Contributions to fragmentation cross sections can be evaluated using the Weizsacker-Williams method of virtual quanta where the virtual photon spectra of the target nuclei is folded with the photonuclear reaction cross section for the projectile emittal (Norbury and Townsend, 1990; Wilson *et al.*, 1991).

4. Intranuclear cascade models

Monte Carlo simulation techniques can be used to describe nuclear multiple scattering (Ferrari and Sala, 1996; Cugnon, Volant, and Vuillier, 1997) in the so-called intranuclear cascade model (Metropolis *et al.*, 1958). The Monte Carlo approach to reaction theories relies on the phase space considerations and two-body (NN) cross sections and production cross sections for various mesons and delta resonances. The MST is treated in an algorithmic manner by following each nucleon by sampling over the possible energy and momentum transfer allowed by the two-body cross sections, often including Pauli blocking and other nuclear medium effects. Several approaches are used in these codes (Cugnon, Volant, and Vuillier, 1997; Ballarini, Battistoni, and Brugger, 2007) to couple to the intranuclear cascade including the preequilibrium models and the nuclear evaporation models One advantage to the MC approach is that all orders of scattering can be followed in the algorithm. However, many of the quantum aspects of the problem must be ignored including shell structure, the nuclear surface, and interference effects. At high energies, the dual patron model implemented in the JAM code is used by several of the MC transport codes. The FLUKA code uses a multifaceted approach where at high energies the dual patron model is assumed and supplemented by a Glauber-Gribov cascade approach. In the intermediate energy range a generalize INC model is used and finally the preequilibrium approach to nuclear thermalization (PEANUT) model is used (Ballarini, Battistoni, and Brugger, 2007).

5. QMD

In the QMD model (Neise *et al.*, 1990) each nucleon is represented by a Gaussian wave packet and the total wave function is a single particle product of these functions. The one-body distribution function is found by the Wigner transformation of the wave function

$$f(r,p) = N \exp\left[-\frac{(\vec{r}-\vec{R}_i)^2}{2L} - 2L(\vec{p}-\vec{P}_i)^2\right], \tag{33}$$

where L is a parameter representing the spatial spread of the wave packet, R and P correspond to the center-of-mass position and momentum of the wave packet, respectively, and N is the normalization constant. The value of L is taken as 2 fm^2 to best represent stable nuclear ground states (Niita *et al.*, 2006). The equations of motion for the time development of the center-of-mass coordinates obey Newtonian equations. The nuclear potential use in the QMD is usually the Skyrme-type NN interaction with a Coulomb potential. At the end of the dynamical stage of the reaction, deexcitation or ablation of the project and target nuclei occurs using the GEM code in the PHITS version of QMD. An arbitrary parameter in the simulations is the switching time from the dynamical of the QMD stage to the deexcitation which is usually taken as 100 to 150 fm/s (Niita *et al.*, 2006).

6. Fragment momentum distribution

The momentum distribution of projectile fragments can be described as a Gaussian distribution in the projectile rest frame with a small downshift in the average momentum from the projectiles velocity. The longitudinal momentum width is well described by (Goldhaber, 1974)

$$\sigma_L = \sigma_0\left[\frac{n(A_P - n)}{A_P - 1}\right]^{1/2}, \tag{34}$$

where n is the number of nucleons removed from the projectile, and σ_0 is related to the Fermi momentum of the projectile p_F by $\sigma_0 = p_F/\sqrt{5}$. The functional form of the model of Eq. (34) has been discovered in several distinct models (Hufner, 1985); however, it likely arises to the large number of intermediate states in abrasion and ablation, such that the central limit theorem leads to a Gaussian form. The transverse width is approximately the same as the longitudinal for heavier fragments. A small momentum downshift also occurs and is dependent on the fragment mass. Transformation of the Gaussian distribution to the laboratory rest frame at the high energies of interest for space radiation transport problems reveals a narrow angular distribution for projectile heavy ion fragments that are strictly forward peaked in a narrow cone (< 5 deg), i.e., the physical reason for the success of the straightforward approximation. For lighter fragments the longitudinal and traverse widths diverge and the Gaussian model breaks down. This is due both to their smaller mass and to the multiple sources for light particle production including projectile abrasion, projectile ablation, target abrasion, and target ablation, as well as a possible intermediate source due to the formation of an intermediate rapidity fireball in central collisions.

C. Nuclear fragmentation measurements

Older studies used chemical decay methods to extract fragmentation cross sections from target decays; however, these data are considered to be less accurate than the measurements of the cross section directly from projectile interactions with target atoms. Nuclear plastic track detectors became commonly used for fragmentation cross-section measurements through the introduction of CR-39 solid state nuclear track detectors ($C_{12}H_{18}O_7$), which allowed lower charge ions to be measured increasing the accuracy of fragmentation measurements and this approach is still used today. Iancu, Flesch, and Heinrich (2005) used CR-39 detectors of 0.6 mm thickness to determine trajectories and charges of nuclear fragments. Etching in 6 N NaOH at 60° C for 59 h helped to identify etch pits and latent tracks which are related to the energy loss of the ions. Scanning systems on computed controlled microscopes and image analysis software have been developed to improve data analysis. Of interest is a similar approach that can be used to understand charge and LET spectra from astronauts returning from space when CR-39 is made part of crew personnel dosimetry.

The earliest studies of projectile fragmentation with particle beams were reported by Schimmerling, Vosburgh, and Todd (1971) at the former Princeton-Penn Accelerator. Silicon detectors provided a reliable and convenient approach to the measurement of fragmentation cross sections and were used by several groups at Lawrence Berkeley National laboratory including the work of Schimmerling *et al.* (1989) of Ne beams in a water column, Webber, Kish, and Schrier (1990) on carbon and CH_2 targets for cosmic-ray studies, and by Cummings *et al.* (1990) for a variety of targets of interest for shielding analysis. More recently a large number of measurements have been made with a similar approach by the Lawrence Berkeley Laboratory group with the experimental setup shown in Fig. 19. Upstream of the target are detectors that ensure that events are initiated by a single incident ion. The T1 and T2 detectors are 330 mm thick with active areas of 300 mm^2 and are used to trigger the experiment. A pair of 1 mm thick with 1500 mm^2 active area position-sensitive silicon detectors (PSD1Y and 1X) are placed downstream of the target material. A second set of position-sensitive detectors (PSD2Y and 2X) are placed 30 cm farther downstream. Each PSD generates two position-dependent signals and a signal proportional to the total charge liberated in the detector. Data analysis examines the energy loss in T1 and T2 and the position-sensitive detectors. Based on the energy loss in the various detectors, a series of cuts is made to ensure the primary initiated the fragmentation event and to reject events where fragments undergo a second reaction in one of the detectors. The number of events of a given charge is denoted $N(Z)$, and the probability of the projectile interaction in the absence of the target by $P_0(Z)$.

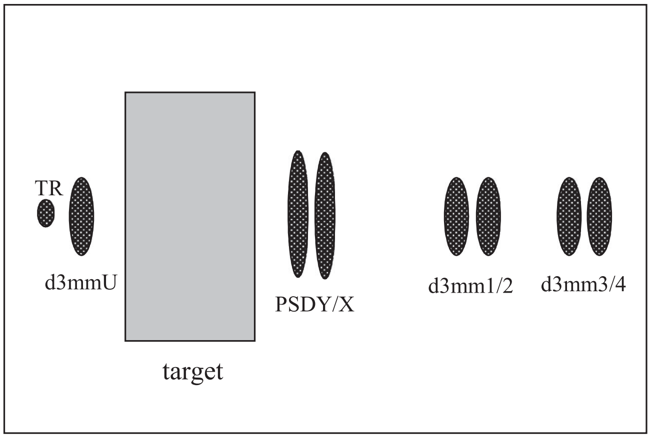

FIG. 19. Schematic diagram showing the relative sizes, depths, and positions of the target and detectors used in experimental setup of the Lawrence Berkeley Laboratory group. The position of the detectors and target materials and thicknesses are modified dependent of the projectile charge and energy and the target material. From Zeitlin *et al.*, 2010.

The charge changing cross section is given by

$$\sigma_{\rm cc} = \frac{-A\ln[P(\text{primary})]}{\rho d N_a}, \tag{35}$$

where N_a is Avogadro's number, ρ is the target density, and A is the target mass number. For describing projectile fragmentation, total inclusive cross sections for fragmentation of the more abundant GCR nuclei are needed at several energies and for an array of targets of interest for spacecraft shielding and for transport in tissues. The cross section for each fragment is corrected for the background from the detector system (Zeitlin *et al.*, 1997).

For heavy ion fragmentation, a minimum data set includes elemental distributions for $Z_F > 2$; however, isotopic cross sections are more stringent tests of cross-section models than the elemental cross sections. For neutron, hydrogen, and helium fragments, cross section differentials in energy and

TABLE VI. Representative experimental data on fragmentation of $Z = 10$ to 28 projectiles on elemental targets.

Projectile	Energy (GeV/nucleon)	Targets	Z_F range	Reference
^{20}Ne	0.6	H, C, Al, Cu, Sn, Pb	3–9	Zeitlin *et al.* (2001)
^{20}Ne		H, C		Webber, Kish, and Schrier (1990)
^{24}Mg	3.65	C, Al, Cu, Ag, Pb	6–11	Sampsonidis *et al.* (1995)
^{24}Mg	0.6	H, C	6–11	Webber, Kish, and Schrier (1990)
^{28}Si	14.5	H, C, Al, Cu, Ag, Pb	6–13	Brechtmann and Heinrich (1988)
^{28}Si	0.45	H, C, Al, Cu, Ag, Pb	6–13	Flesch *et al.* (2001)
^{28}Si	0.6	H, C, Al, Cu, Ag, Pb	5–13	Zeitlin *et al.* (2008)
^{32}S	3.65	C, Al, Cu, Ag, Pb	7–15	Sampsonidis *et al.* (1995)
^{32}S	0.7	H, C, Al, Cu, Ag, Pb	6–15	Brechtmann and Heinrich (1988)
^{32}S	1.2	Al, Pb	6–15	Brechtmann and Heinrich (1988)
^{35}Cl	0.65, 1.0	H, C, Al, Cu, Ag, Pb	5–16	Zeitlin *et al.* (2008)
^{36}Ar	0.4	H, C, Al, Cu, Ag, Pb	7–17	Iancu, Flesch, and Heinrich (2005)
^{40}Ar	1.65	C, KCl	9–19	Tull (1990)
^{40}Ar	0.4	H, C, Al, Cu, Ag, Pb	5–17	Iancu, Flesch, and Heinrich (2005)
^{40}Ar	0.4, 0.65	H, C, Al, Cu, Ag, Pb	5–17	Zeitlin *et al.* (2008)
^{48}Ca	0.21	Be		Westfall *et al.* (1979)
^{48}Ti	1.0	H, C, Al, Cu, Ag, Pb	5–21	Zeitlin *et al.* (2008)
^{56}Fe	1.09	H, C	12–25	Webber, Kish, and Schrier (1990)
^{56}Fe	1.55	H, C, Al, Cu, Pb	12–25	Cummings *et al.* (1990)
^{56}Fe	1.05	H, C, Al, Cu, Pb	12–25	Zeitlin *et al.* (1997)
^{56}Fe	0.66	H, C, Al, Cu, Ag	6–25	Flesch *et al.* (1999)
^{56}Fe	1.65	H, C, Al, Cu, Ag	6–25	Flesch *et al.* (1999)

angle are required. Table VI shows a recent survey of existing measurements for elemental distributions for fragments produced from GCR projectiles with charges from 10 to 26 showing the target mass projectile energy available. Cross sections for the C and O nuclei are more numerous and have considered isotopic distributions rather than elemental ones (Olsen *et al.*, 1983). Data sets for projectiles can be divided roughly into three types of studies, with the first including more than one beam energy over the full range of target masses important for spacecraft and planetary habitats. A second series of experiments made complete measurements at one beam energy over the full range of target masses with supplemental data at other energies. Finally, other data sets consider measurements limited in target mass and energy spread. There are a reasonable number of projectile fragmentation data sets now available with the above noted exceptions; however, the projectile energies of the data are lacking with more data needed in the 0.1 to 0.4 GeV/amu region and above 1 GeV/amu. Also cross-section data and multiplicities extending to lower fragment charge are needed. The isotopic composition of the GCR (Webber, Kish, and Schrier, 1990; Cucinotta, Kim, and Ren, 2006) needs to be considered with the full grid of isotopes rather than reduced ones in order to eliminate unnecessary error. The Fe fragmentation measurements of Zeitlin *et al.* (1997) resolved discrepancies in older data sets. Figures 20 and 21 compare measurements to several nuclear reaction models. The odd-even effect is not described by the nuclear fragmentation model version 2 (NUCFRG2) and is under-represented by the PHITS code. The QMSFRG model is in good agreement with many data sets (Cucinotta, Wilson *et al.*, 2006) and provides a good description of the odd-even effects, which originates largely from the ablation step.

Light particle production (n, p, d, ^{3}H, ^{3}He, ^{4}He, and mesons) in the GCR is largely from primary and secondary protons and neutron induced reactions. Current transport codes predict 10%–30% of light particles are produced by helium and HZE nuclei induced reactions depending on material type. However, these estimates are based on sparse cross-section databases. A large number of measurements exist for p and n production for p and n induced reactions [see, e.g., Alard *et al.* (1987) and review by ICRU (2000)]. Most radiation transport codes have assumed only an evaporation component for d, t, h, and α target fragments and neglecting the importance of a fast knockout component of these ions for GCR transport.

These ions contribute substantially to the buildup effect in shielding due to their ranges which scale with the proton range as p:d:t:h:α to 1:2:3:3/4:1 and provide up to a 25%

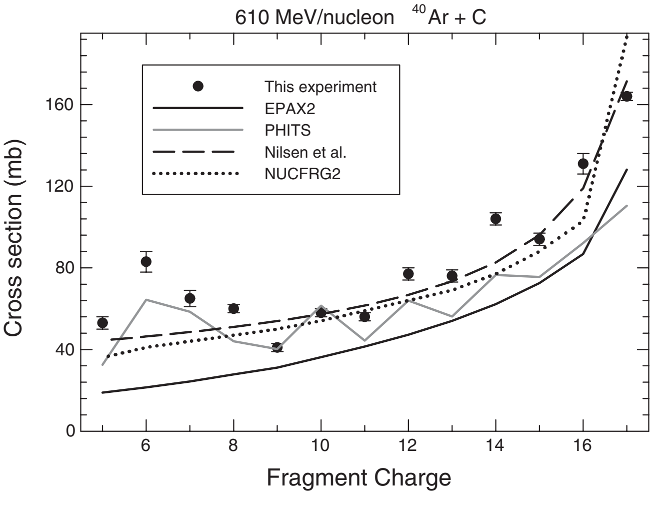

FIG. 20. Fragmentation cross sections for ^{40}Ar on ^{12}C at 610 MeV/nucleon. Comparisons to several fragmentation models are shown. From Zeitlin *et al.*, 2008.

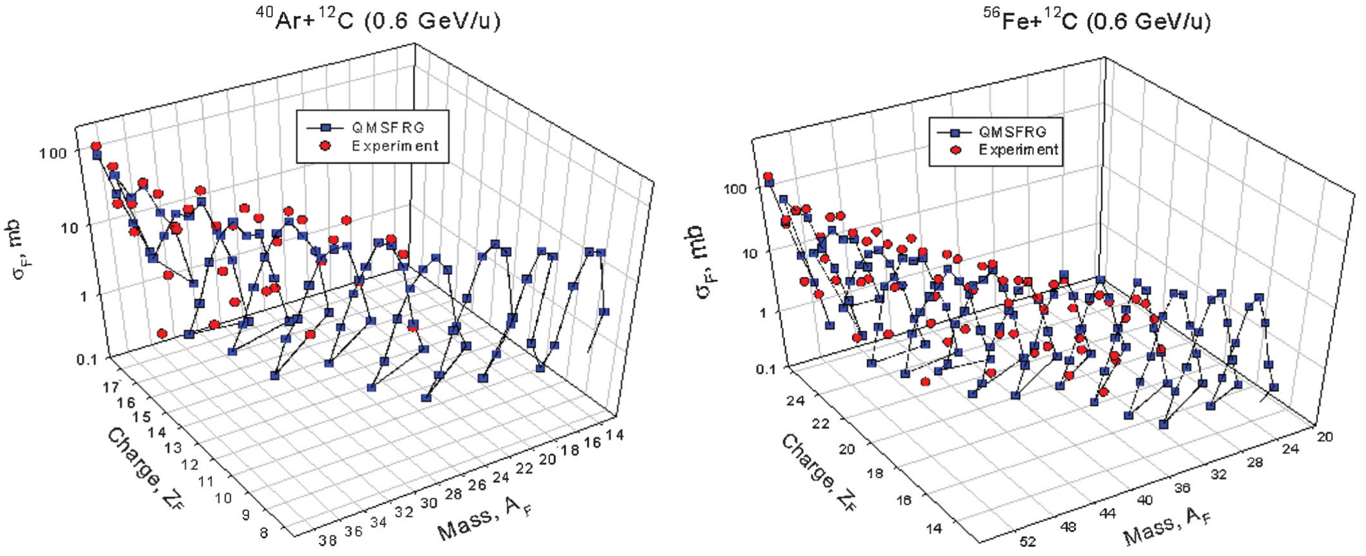

FIG. 21 (color). Comparisons of the QMSFRG model (Cucinotta, Wilson *et al.*, 2006) to experiment for isotopic distribution of fragments for (left panel) ^{40}Ar on ^{12}C at 0.6 GeV/nucleon and (right panel) ^{56}Fe on ^{12}C interactions at 0.6 GeV/nucleon. Experimental data from Webber, Kish, and Schrier, 1990.

increase in the dose equivalent for aluminum shielding over the evaporation contribution alone (Cucinotta, Townsend *et al.*, 1996). Direct knockouts of high-energy tritons are especially important because of their large ranges in shielding. Knockout components will be sensitive to nuclear structure effects such as shell structure and clustering in the nuclear ground state. For example, α knockouts contribute for ^{12}C and ^{16}O projectile or targets, d knockout for ^{14}N, and t for ^{27}Al. The limited existing measurements of these cross sections suggest that double-differential cross-section measurements at several proton energies on a wide range of targets are needed. Light particle production from composite projectiles provides an interesting effect where a substantial number of particles are produced with a higher velocity than that of the projectiles due to internal Fermi motion of the projectile. The effects of this process on GCR transport have not been studied. These data could be supplemented with double-differential cross sections for light particle production from several of the more abundant GCR nuclei (e.g., He and O).

D. Validation of transport codes

There are three approaches to assessing uncertainties in transport models describing exposures to sensitive tissue sites behind spacecraft shielding from space radiation:

1. Comparison of ground-based measurements for defined beams of thin and thick targets for different material compositions and amounts.
2. Intercomparison of radiation transport codes using matched configurations and environments.
3. Comparison of transport codes to spaceflight measurements.

The NASA Space Radiation Laboratory (NSRL) made extensive measurements for a variety of HZE nuclei of the Bragg ionization curve in polyethylene or aluminum shielding. A recently developed Monte Carlo based transport code, the GCR event-based risk model (GERMCODE), utilizes the QMSFRG model of the nuclear interaction database, and the atomic energy loss subroutines from HZETRN to describe the NSRL beam line for radiobiology applications (Cucinotta, Plante *et al.*, 2011). Figure 22 shows a comparison of the NSRL measurements to the GERMCODE for ^{28}Si, ^{37}Cl, ^{48}Ti, and ^{56}Fe nuclei. Excellent agreement between the model and measurements is seen at all depths, including past the Bragg peak or primary-ion range where only secondary radiation contributes. In Fig. 23 we show comparisons of the GERMCODE to measurements by Zeitlin *et al.* (2008) of elemental distributions of secondary fragments at two depths in polyethylene shielding for 1 GeV/u Fe beams. Agreement between theory and measurements is typically within ±20%. Energy loss in silicon detectors has been measured behind graphite epoxy. Data were compared to the GREENTRN code, which has many important overlaps with the HZETRN code. The results in Fig. 24 show good agreement between the code and measurement (Walker *et al.*, 2005).

Intercomparisons of the HZETRN code to different Monte Carlo codes (HETC-HEDS and FLUKA) have been performed for well-defined shielding configurations and identical source energy spectra for GCR (Heinbockel *et al.*, 2011a) and SPEs (Heinbockel *et al.*, 2011b). These results, as summarized in Fig. 25, show good agreement for neutron and deuterons from GCR proton spectra behind 20 cm of water shielding. Other comparisons on organ doses did not consider all of the contributions from target fragments that introduce minor differences and some inconsistencies in how the different codes evaluate the dose are apparent (Heinbockel *et al.*, 2011a, 2011b).

These comparisons show a reasonable overall agreement between transport code predictions when compared with identical source spectra and shielding configuration. However, in some cases different codes give very different predictions, especially for the production of light ions, where predictions can differ as much as an order of magnitude. A possible minor discrepancy is the mesons, electrons, and γ rays that may contribute 10% to 15% of the absorbed

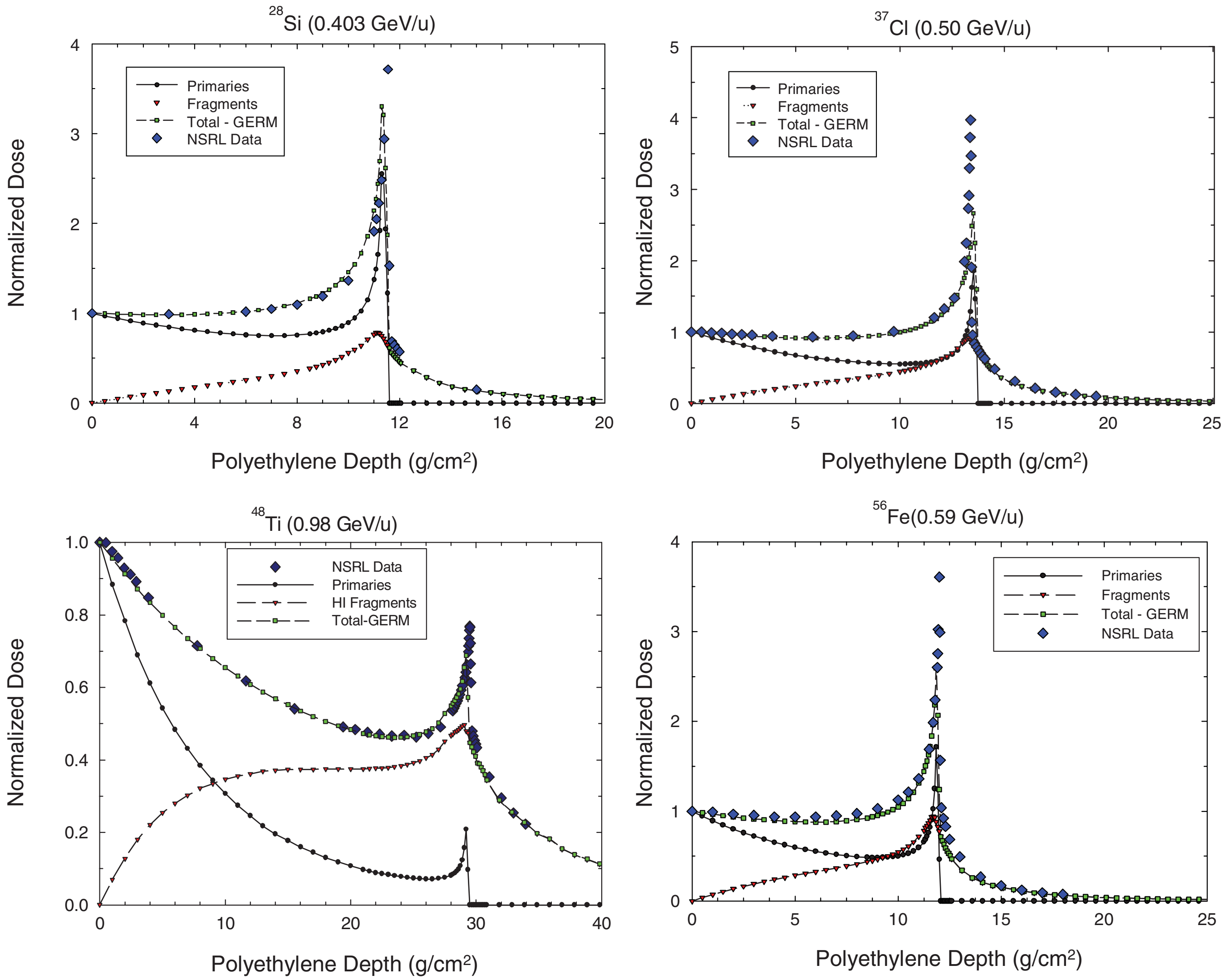

FIG. 22 (color). Comparisons of the GERMCODE with QMSFRG cross sections to NSRL measurements for the depth dose in polyethylene for nearly monoenergetic ^{56}Fe (0.59 GeV/u), ^{48}Ti (0.98 GeV/u), ^{37}Cl (0.5 GeV/u), and ^{28}Si (0.403 GeV/u) nuclei. From Cucinotta, Plante *et al.*, 2011.

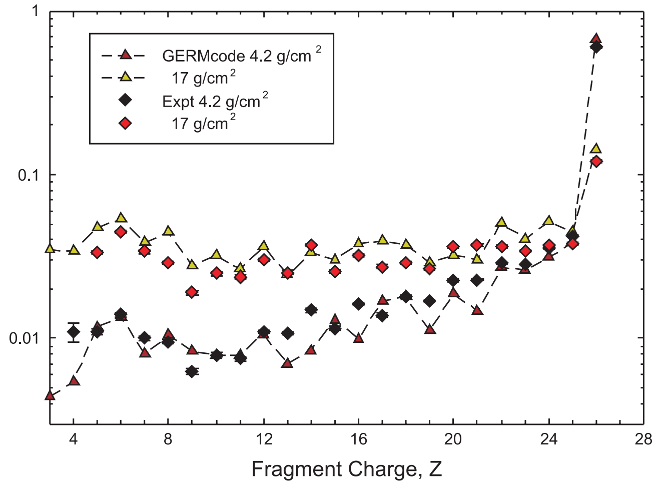

FIG. 23 (color). Comparison of the GERMCODE with the QMSFRG nuclear cross-section model to thick target data from Zeitlin *et al.* (2008) for fragmentation of 1 GeV/nucleon ^{56}Fe beam at two depths of polyethylene.

dose from GCR behind ISS levels of shielding (Aghara *et al.*, 2009); however, they provide a much smaller contribution to the dose equivalent, because of their small quality factor compared to HZE nuclei or stopping protons and He nuclei. These processes have not been fully integrated into all versions of the various existing codes and should be considered for deep shielding predictions (> 50 g/cm^2). Agreement between the NASA codes with phantom torso measurements on the space shuttle and ISS are within 20% (Cucinotta *et al.*, 2008), and the comparison of energy spectra discussed above suggests a similar agreement would be obtained with other transport codes.

Energy spectra for light particles have been measured with particle hodoscopes and shown good agreement with the HZETRN code as shown in Fig. 26 (Badhwar *et al.*, 1995) and for neutrons in Fig. 27. Measurements of heavy ion spectra require large detector areas and few have been made in human rate vehicles because of the mass requirements. Other spaceflight measurements of LET or microdosimetry measurements of lineal energy spectra using

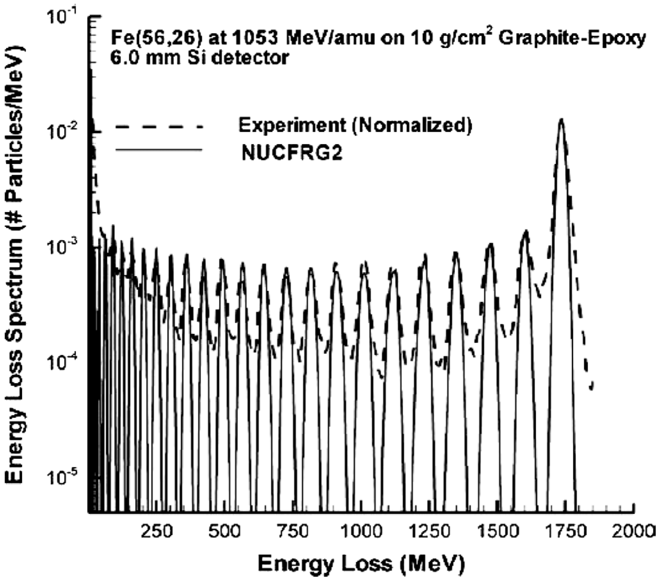

FIG. 24. Comparisons of the GREENTRN code to measurements for the summed energy loss in the silicon detector from fragments of a 1053 MeV/amu ^{56}Fe beam behind 10 g/cm^2 graphite epoxy (51%/49%). From Walker *et al.*, 2005.

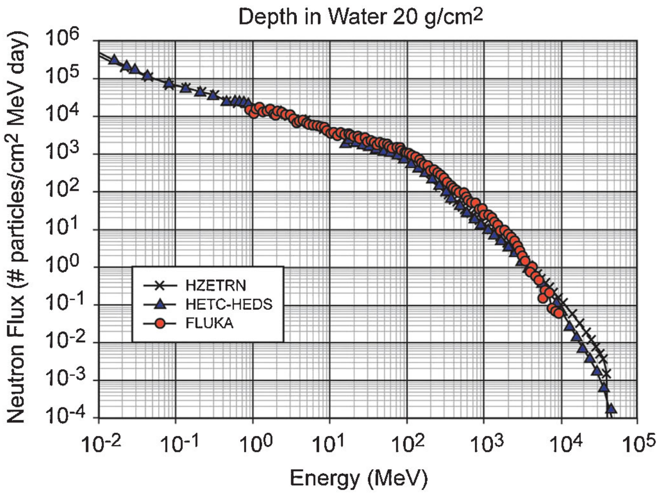

FIG. 25 (color). Intercomparison of secondary neutron spectra calculated with several space radiation transport codes. From Heinbockel *et al.*, 2011a.

TEPC have also been shown to be in good agreement with transport codes (Shinn *et al.*, 1999; Barber *et al.*, 2001). Agreement is improved when models of detector response are used to make such comparisons. Corrections of measurements often involve model dependent assumptions such as the conversion from silicon to tissue-equivalent LET spectra where the conversion factor is dependent on energy and charge number. Also, the combined TLD plus CR-39 method for estimating dose equivalent (Yasuda *et al.*, 2001) involves corrections on the high LET sensitivity of TLDs and low LET sensitivity of CR-39. TEPC comparisons to measurements require the conversion of energy and charge spectra into lineal energy spectra, which can differ substantially from LET spectra.

E. Track-structure models

Track-structure models provide a description of the position of excitations and ionization of target molecules from the passage of ions through a medium. These descriptions are needed in theoretical models of biological responses, for understanding the extrapolation of limited radiobiology data to other radiation qualities, and for describing the response of radiation detectors to the variety of ions in space (Katz, Scharma, and Homayoonfar, 1972). Application of Monte Carlo track-structure simulation codes has been used for studying the distribution and types of initial DNA damage including models of single-strand break, double-strand break, base damage, and clusters of DNA damage (Goodhead and Nikjoo, 1989), of oxidative species created by radiation (OH^-, H_2O_2, $e-$, etc.) (Plante and Cucinotta, 2008) or the description of the response of TEPCs (Nikjoo, Khvostunov, and Cucinotta, 2002). Analytic models have also been used for a range of application in particle detection and the theoretical description of radiobiology data. The assumptions of analytical models can be validated by the more detailed MC simulations and are useful for space radiation applications, where a large number of particle types and energies place practical limitation on the use of MC simulations.

1. Monte Carlo track simulations

Ionization and excitation processes caused by the ions track and the electrons liberated by the primary ions lead to a stochastic process of biological events as particles pass through DNA, cells, or tissues (Paretzke, 1987). The energetic secondary electrons denoted as δ rays can traverse many cell layers from the track. The so-called core and penumbra are loose terminology that appear in the literature; however, there has been no precise definition of these terms other than the core is close to the track and the penumbra due to the far reaching δ rays. Older models (Chatterjee and Schaefer, 1976) artificially assumed 50% of the energy deposition is in the core and 50% in the penumbra. In fact, more than 80% of the energy deposition from heavy ions is imparted by δ rays (Cucinotta *et al.*, 1998).

The cross sections needed for track simulation codes are the total, total elastic, total inelastic, ionization, and excitation cross sections. Single and double-differential cross sections are needed for production of electrons from the primary ion and for production from the secondary δ rays (Plante and Cucinotta, 2008). For ion tracks, codes include RITRACK, PITS, OREC, and DELTA; however, the energy and charge range of many of these codes are limited to energies below 10 MeV/nucleon or require extensive CPU times to sample high-energy δ rays produced by relativistic ions. The RITRACK code generates radiation tracks up to very high energies ($>$ 10 GeV/nucleon) and includes relativistic corrections to ionization and excitation cross sections, including bremsstrahlung contributions (Plante and Cucinotta, 2008, 2009) as well as the production of different radiolytic species.

The GSI code TRAX (Krämer and Kraft, 1994) uses the empirical cross-section formulas by Rudd (1997) modified for use at high ion energies and with empirical corrections in accordance with energy loss tables. With this correction, the microscopic calculations of TRAX can be expanded to predict

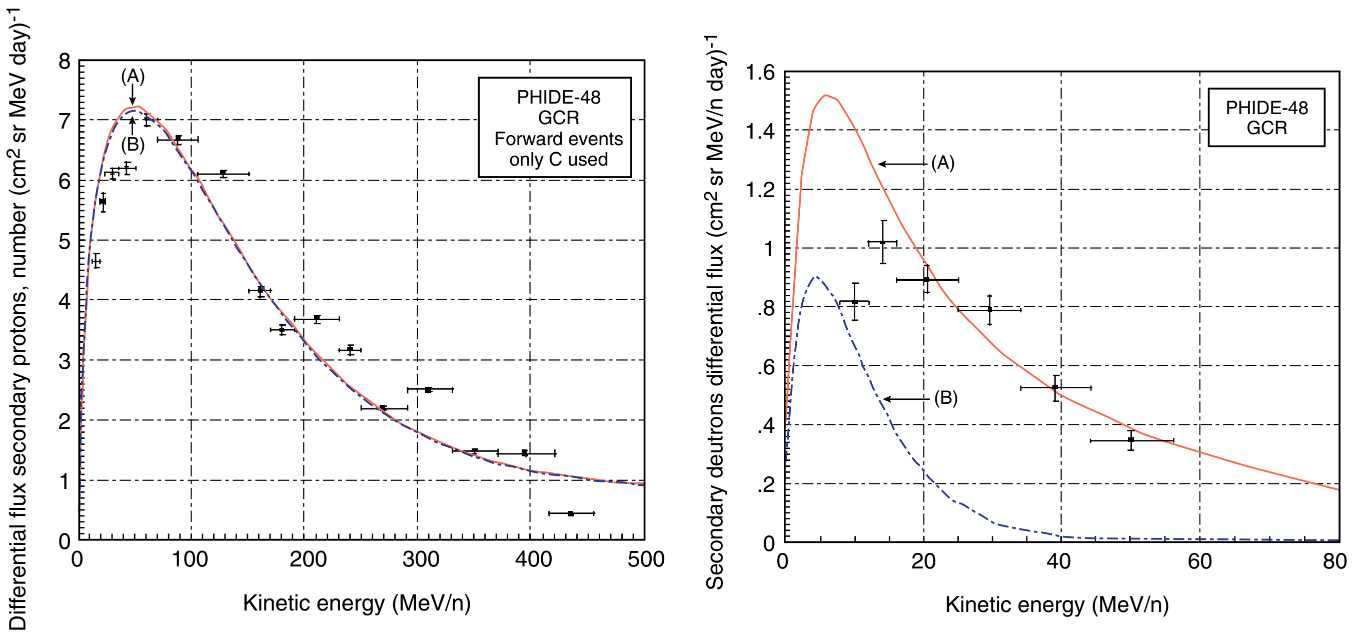

FIG. 26 (color online). Comparisons of proton (left) and deuteron (right) energy distributions from GCR on the STS-48 mission to HZETRN results. From Badhwar *et al.*, 1995.

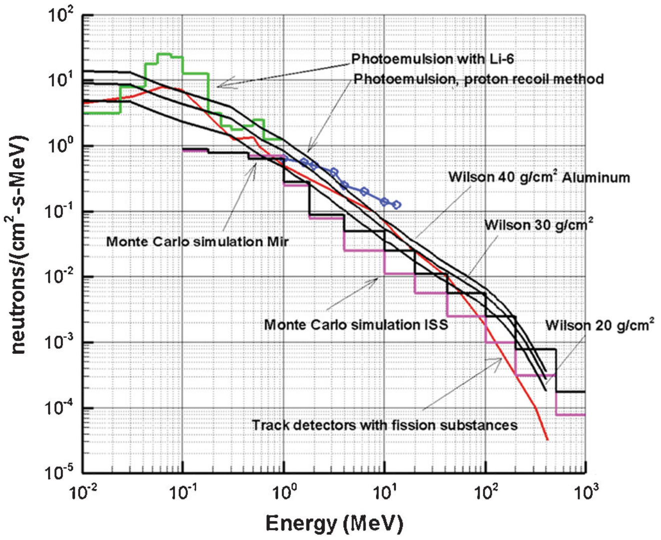

FIG. 27 (color). Comparisons of transport codes to ISS neutron spectra measurements.

macroscopic quantities, such as the position of the Bragg peaks of heavy ions. Bragg peak positions can be reproduced within less than 0.7 mm, and the dose values are in good agreement with macroscopic calculations. TRAX yields the width of the Bragg peaks in a natural way as a result of the emission of δ electrons with a spectrum of kinetic energies. With the inclusion of nuclear interactions, which are not described in the current code version, TRAX should be able to accurately reproduce the macroscopic dose deposition patterns starting from *ab initio* microscopic track-structure simulations (Krämer and Durante, 2010).

There are few data at high energies to validate the accuracy of the electron production cross sections or effective charge assumptions used by these models (Rudd, 1997). Intercomparisons of codes for the frequency distribution in

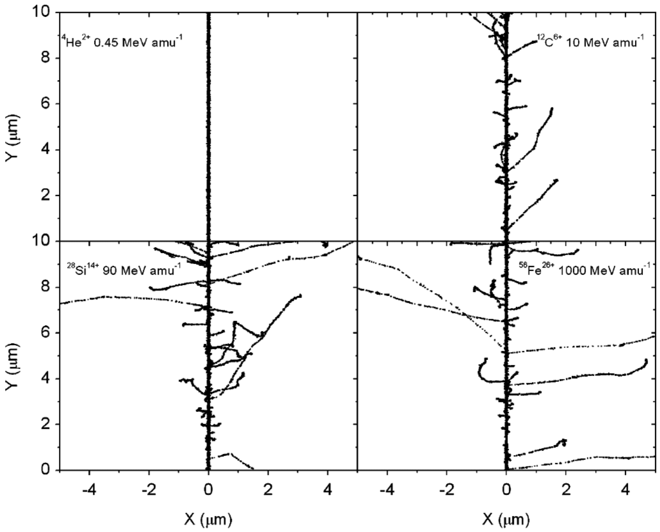

FIG. 28. Projections over the X-Y plane of simulated tracks segments (calculated at $\sim 10^{-12}$ s) for the following impact ions: $^{4}\mathrm{He}^{2+}$ (0.45 MeV amu^{-1}), $^{12}\mathrm{C}^{6+}$ (1 MeV amu^{-1}), $^{28}\mathrm{Si}^{14+}$ (90 MeV amu^{-1}), and $^{56}\mathrm{Fe}^{26+}$ (1 GeV amu^{-1}). Ions are generated at the origin along the Y axis in liquid water at 25° C under identical LET conditions ($\sim$ 150 keV μm^{-1}). Each dot represents a radiolytic species. From Plante and Cucinotta, 2008.

biomolecules by ions and electrons have been made and indicate reasonable agreement between models (Nikjoo, Uehara, and Brenner, 1997). In Fig. 28 we show a stochastic description of energy deposition in water for different ions with identical LET of 150 keV/μm.

2. Analytic track-structure models

A "first-order" numerical approach that relates LET, the basic physical parameter in conventional risk assessment, to track structure is to consider the relationship between the radial dose distributions about the track and the LET. The radial dose is the energy density distribution in a cylindrical shell of radius t, about the ions path (Butts and Katz, 1967). LET is related to the radial dose by integrating the radial distribution over all radial distances up to the maximum allowable value t_M:

$$\mathrm{LET} = 2\pi \int_0^{t_M} t dt [D_\delta(t) + D_{\mathrm{exc}}(t)] + \text{nucl. stopping}. \tag{36}$$

In Eq. (36) contributions from ionization are denoted here as D_δ, and excitations D_{exc} are considered in the radial distribution. The value of t_M defines the track width and is a function of ion velocity, corresponding to the range of electrons with maximum energy ejected by the passing ion. The track width can extend well beyond 100 μm as the ion's velocity approaches the speed of light. The effects of nuclear stopping in radiation action are only important for very low-energy ions (< 0.1 MeV/nucleon). In the model of Kobetich and Katz (1968) the primary electron spectrum from ion interactions with target atoms is folded with average transmission properties of electrons to obtain the spatial distribution of electron dose as a function of radial distance from the ion's path. The radial dose from ionization and δ-ray transport is described by

$$D_\delta(t) = -\frac{1}{2\pi t} \sum_i \int d\Omega \int d\omega \frac{\partial}{\partial t} [E(t,\omega)\eta(t,\omega)] \frac{dn_i}{d\omega d\Omega}. \tag{37}$$

In Eq. (37) ω is the initial electron energy, E is the residual energy of an electron with energy ω after traveling distance t, and $\eta(t,\omega)$ is the transmission probability that an electron with starting energy ω penetrates a depth t. Equation (37) includes an angular distribution for the number of primary electrons produced from target atom i, n_i, with energy ω and solid angle Ω. The cross sections for electron production from protons are scaled to heavy ions using the effective charge Z^*. The angular distribution has important effects on the radial distribution at both large and small radial distances, and only a minor effect at intermediate values where a $1/t^2$ behavior holds. An *ansatz* (Brandt and Ritchie, 1974) can be used for the radial dependence of the excitation term $D_{\mathrm{exc}}(t)$ as

$$D_{\mathrm{exc}}(t) = C_{\mathrm{exc}}(A, Z, \beta) \frac{\exp(-t/2d)}{t^2}, \tag{38}$$

where $d = \beta/2hc/(2\pi\omega_r)$, c is the speed of light, β is the ion velocity scaled by c, h is Plank's constant, $\omega_r = 13$ eV for water, and C_{exc} is the normalization parameter. In Eq. (38) the radial extension of excitations is confined to very small distances (< 10 nm) as characterized by the parameter d (Brandt and Ritchie, 1974). Characteristics of the two components of the radial dose are illustrated in Fig. 29, for two ions of LET close to 30 keV/μm (1 MeV H and 300 MeV/nucleon Ne ions) (Cucinotta, Nikjoo, and Goodhead, 1999). The radial dose for the Ne beam extends for many microns, while the low-energy proton beam deposits all of its energy within 0.1 μm of the track.

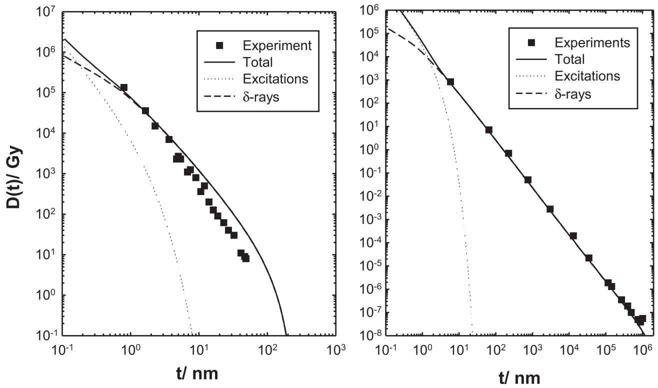

FIG. 29. Comparison of calculations of radial dose distributions to experiments for ^{1}H at 1 MeV (LET = 27 keV/μm) and ^{20}Ne at 377 MeV/nucleon (LET = 31 keV/μm). From Cucinotta, Nikjoo, and Goodhead, 1999.

A "second-order" numerical approach to track structure, more closely related to the Monte Carlo simulation, is to model the frequency distribution of energy imparted to a volume of biomolecular dimensions (Goodhead, 1995; Cucinotta, Nikjoo, and Goodhead, 2000). For high-energy ions, the frequency distribution can be described using the ion's impact parameter and distinguishing events where the ion passes through the volume (primary-ion events) and outside the volume (δ-ray events), and by determining the mean and variance of the energy imparted to the volume including corrections for δ-ray escape out of the volume. The two components are weighted by considering the number of events as a function of impact parameter. The frequency distributions (Goodhead, 1995; Cucinotta, Nikjoo, and Goodhead, 2000) demonstrate that there are energy deposition events in biomolecular targets that occur for high-LET radiation that are not possible with low-LET radiation, even at high doses (< 100 Gy) (Goodhead and Nikjoo, 1989). Validations of theoretical predictions of track-structure models are severely limited at this time; however, the development of new experimental techniques in nanodosimetry could offer approaches for validation.

IV. SHIELDING

On Earth, radiation protection strategies are normally divided into 3 groups as follows: (1) increasing the distance from the source, (2) minimizing time of the exposure, and (3) use of radiation shielding.

Increasing the distance to the source plays no role in space because the GCR are omnidirectional, and SPEs permeating along magnetic field lines become isotropic within a few hours after an event start (NCRP, 2006). Minimizing time of the exposure is problematic for space exploration because it may limit the performance of mission science objectives. Increasing rocket velocity to shorten times to planetary destinations is a long-term goal of space programs. The Apollo missions to the Moon lasted up to 12 days, exploration of near Earth objects such as asteroids may take up to a year, and a Mars mission can last up to 1100 days with conventional rockets. New nuclear reactor powered plasma propulsion systems such as the VASIMR are under development, which can cut Earth-to-Mars transit times below 60 days (Chang-Diaz, 2000), but at the time exist in concept only (Durante and Bruno, 2010). For farther destinations, such as the outer planets or interstellar exploration, long times in space must be accommodated by radiation protection methods. Thus, developing spacecraft or planetary habitat shielding becomes the major approach for radiation protection with biological countermeasures or genetic selection for radiation resistance outside the scope of this review.

SPE shielding problems have been shown to be readily solved using current technologies and localized storm shelters inside spacecraft, which is not the case for the problem of GCR shielding. For both GCR and SPE, material selection and optimization of topology are major considerations. Spacecraft volumes may be constrained as well as mass when considering shielding augmentation. More importantly, the extra fuel required to launch such shielding compounds the mass dedicated to shielding. There is also a competition between shielding mass relative to other necessary resources or flight safety factors. Dual use shielding approaches, such as water, fuel, and food storage, are useful in this regard. *In situ* shielding using planetary resources is also of interest. Passive and active shielding approaches are both areas of ongoing research.

Basic concepts in atomic and nuclear physics can be used to guide material selection augmented with detailed radiation transport code predictions. Engineering considerations on material strength, temperature, UV degradation, flammability, etc. must be considered along side of radiation protection, and the composite picture must be analyzed. Materials with the smallest mean atomic mass are usually the most efficient shields for both SPE and GCR. The composition of the radiation field changes as particles lose energy and suffer nuclear interactions in traversing structural materials, instruments, and the tissues of astronauts. Both the energy loss and the changes in particle fluence are related to the number of atoms per unit mass (in units such as grams) in the traversed material, which, in turn, is proportional to Avogadro's number divided by the atomic mass number A for each element of the material. The energy loss by ionization of a single component of shielding material with atomic number Z is proportional to the number of electrons per atom and thus proportional to Z/A. However, the energy lost per gram of material and per incident fluence (e.g., in units of particles per cm^2), the "mass stopping power," is also inversely proportional to the density ρ (e.g., in $\mathrm{g/cm}^3$) of the material, so that the energy lost by one incident particle per cm^2 per unit mass is proportional to $(Z/\rho)A$.

The number of nuclear interactions per unit mass and per unit incident fluence is proportional to σ/A, where σ is the total nuclear reaction cross section. To a first approximation, σ is proportional to $A^{2/3}$, so that the nuclear transmission is proportional to $1/A^{1/3}$. The ratio of electronic stopping power to nuclear interaction transmission is thus proportional to $(Z/\rho)A^{2/3}$. Materials with small atomic mass have the highest number of electrons per nucleon (e.g., Z/A is 1 for hydrogen, 0.5 for carbon, but 0.48 for aluminum, 0.46 for iron, and 0.40 for lead). Light mass materials have smaller nuclei and therefore more of them can fit into a given mass, so that there can be more nuclear interactions. Furthermore, the ratio of ionization energy loss to nuclear interactions is also dependent on the material density. For liquid hydrogen ($\rho_{.} = 0.07\ \mathrm{g/cm}^3$), the ratio is ~ 14, whereas for aluminum ($\rho_{.} = 2.7\ \mathrm{g/cm}^3$) the ratio is only 0.5, and for lead ($\rho_{.} = 11.3\ \mathrm{g/cm}^3$) the ratio is 0.2. From these considerations, an electron plasma would provide the best shield from GCR. A shield made of liquid hydrogen, which has the highest ratio of electrons to nuclei per atom and produces minimal secondary radiation (e.g., mesons), is the second best choice. Hence, interest in polyethylene and hydrogen embedded nanofibers. The character of these interactions and the secondary nuclei produced through both projectile and target fragmentation is important. Lighter nuclei have fewer neutrons to release and some nuclei, e.g., carbon, can break into three helium nuclei without releasing any neutrons. In tissue, the release of three helium atoms is much more biological damaging than that of neutrons; however, if produced within spacecraft shielding materials neutrons are a higher concern because of their longer ranges than slow helium particles. For very thick shields, lighter nuclei are also more effective in shielding against the built-up neutrons. For these and related reasons, detailed knowledge of the actual composition of the radiation fields (and of the biological consequences of exposure to them) is required to evaluate the net effect of shielding materials.

A. Shielding of solar particle events

Solar particles are constrained in energy with most event containing particles with kinetic energies below a few hundred MeV, thus allowing effective shielding approaches to be developed with passive shielding. As described above there have been about 400 SPEs in the space age, however, many of these events lead to very small organ doses. Kim *et al.* (2009a) ranked each event by the proton fluence above 30 MeV to form a probability distribution of the likelihood of an event of a given size and time period using hazard analysis. They then considered the variability in energy spectra for the events with integral fluences $> 10^8\ \mathrm{protons/cm}^2$, corresponding to 34 SPEs. Considering the variability of SPE spectra is preferred over the choice of a single or small number of event spectra (ASEB, 2008). Figure 30 shows results for the blood-forming organ doses behind $5\ \mathrm{g/cm}^2$ aluminum shields. This analysis shows that only 4 SPEs in the space era would have led to doses sufficient to possibly cause acute radiation sickness with fairly minimal shielding amounts. Furthermore, no events would have led to acute radiation death with minimal shielding due to their cumulative organ dose and dose rates (Hu *et al.*, 2009). The results also show that the integral 30 MeV proton fluence is a poor predictor of organ doses, and a more recent analysis shows sufficient improvements when the 100 MeV integral proton fluence is used as a predictor (Kim *et al.*, 2009b). The situation would be different for EVAs where doses can reach high levels for many events; however, spacesuit materials and design reduce exposures to some extent (De Angelis *et al.*, 2004). Using the catalog of past SPEs and probabilistic risk assessment approaches, the level of shielding needed is established to be in the few to about $20\ \mathrm{g/cm}^2$ for the most

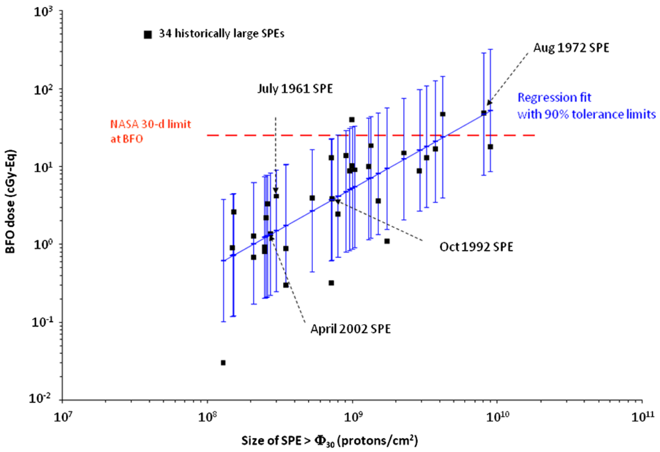

FIG. 30 (color online). The blood-forming organ (BFO) dose behind 5 $\mathrm{g/cm^2}$ aluminum shields from the 34 largest SPEs in the space age (1955–2010) ranked by 30 MeV proton integral fluence, $\Phi > 30$ MeV calculated by the BRYNTRN code. The circles show the doses from each of the 34 events. The error bands show the 90% confidence levels due to the variability of the proton energy spectra based on the 34 events. The dashed line shows the NASA 30 day dose limit for the BFO. From Kim *et al.*, 2009a.

dangerous events. The wall thicknesses of spacecraft are on the order of 5 $\mathrm{g/cm^2}$; however, when the internal equipment is considered shielding thicknesses much higher occur, and 20 $\mathrm{g/cm^2}$ of shielding is easily achieved in localized areas called storm shelters within space vehicles. Optimizing mass through material selection and topological considerations are the focus for SPE shields. Shielding approaches must be developed for transit vehicles, planetary habitats, and EVA including pressurized rovers each of which has specific limitations (ASEB, 2008). Figure 31 shows the advantages of polyethylene or water compared to aluminum in protecting against SPEs where the probability of exceeding the 30-day limit has been calculated for increasing 100 MeV proton fluence. A sufficient reduction in SPE shielding requirements occurs if materials with high hydrogen content are utilized.

Because SPEs last only several hours at the peak exposure rates, localized shielding approaches including EVA shielding, portable shielding, and using crew sleep quarters as storm shelters are considered to be sufficient for SPE protection. Mass requirements on the order of 1000 kg are needed to provide storm shelter protection for a crew of three when optimal material selection and topologies within vehicles or habitats are considered. For EVA shielding nearby pressurized rovers is advantageous; however, spacesuit design and shielding blankets or coats made of hydrogenous materials to cover vital organs is advantageous.

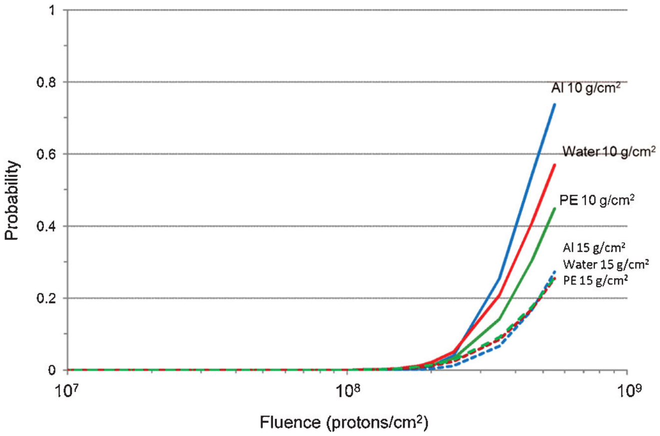

FIG. 31 (color). Calculations of the probability to exceed the 30-day dose limits for the blood-forming organ of 250 mSv, for different shielding material types and amounts, as a function of the fluence of protons with energy $E > 100$ MeV.

B. Shielding of galactic cosmic radiation

Figure 32 shows the contributions from various charge groups to the effective doses for a Mars mission near solar minimum predicted by the HZETRN transport code (Cucinotta, Hu *et al.*, 2010). Charge group contributions to the effective doses for the interplanetary and surface segments are shown along with the total for a 30-month mission to Mars. Note the neutron effective dose from $Z = 1$ and 2 particles is counted in the total values for these groups and not in the neutron category, which shows only $Z > 2$ contributions from neutrons. In Fig. 33 the energy spectra for different charge groups are shown. The heavy ions attenuate slowly with increasing shielding; however, slow protons and helium nuclei of relatively high-LET values build up in tissue along the path of the higher-energy protons, neutrons, and heavy ions making up about one-third of the tissue dose equivalent. The LET spectra for increasing amounts of water and liquid hydrogen shielding are shown in Fig. 34 (Wilson *et al.*, 1995). Clearly $\mathrm{LH_2}$ provides a significant reduction in high-LET components compared to other materials. The predictions of transport codes can be tested by heavy ion accelerator measurements. Zeitlin *et al.* (2008) considered a large number of materials exposed to 1.087 GeV/nucleon Fe nuclei using the detector system uses to measure fragmentation cross sections described in Fig. 19. The measurements (see Fig. 35) verify the improved efficiency of the hydrogeneous materials. A complication arises due to the many energy and charge groups in space. In fact, Durante *et al.* (2005) showed

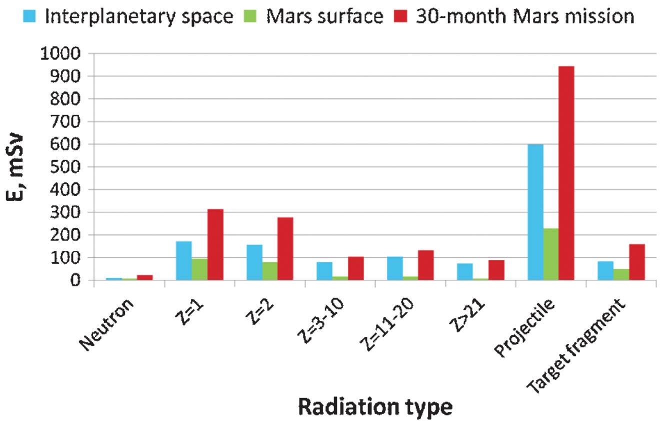

FIG. 32 (color). Charge group contributions to the effective doses for Mars mission and interplanetary and surface segments. Note the neutron effective dose from $Z = 1, 2$ particles is counted in the total for these groups and not in the neutron category which shows only $Z > 2$ contributions from neutrons. From Cucinotta, Hu *et al.*, 2010.

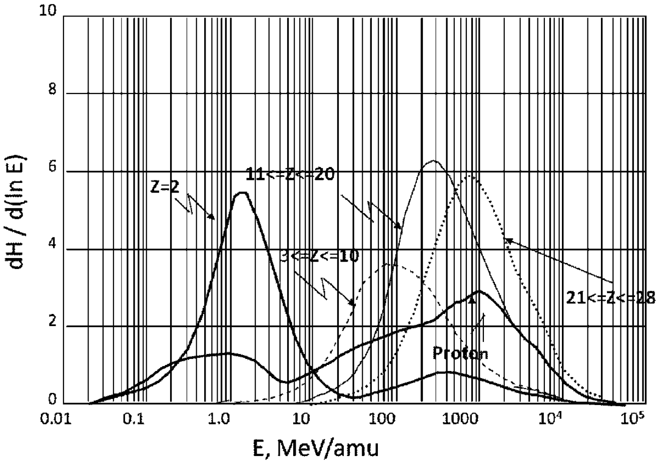

FIG. 33. Contributions of different GCR charge groups vs kinetic energy to the skin dose equivalent calculated in the HZETRN code for 5 $\mathrm{g/cm^2}$ aluminum shielding. From Wilson *et al.*, 1995.

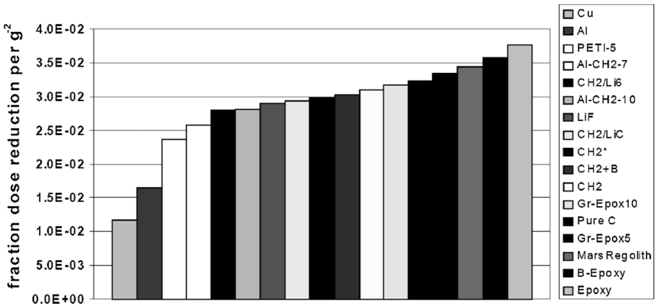

FIG. 35. Dose reductions for various materials placed in a 1.087 GeV/nucleon ^{56}Fe beam. From Zeitlin *et al.*, 2008.

that for chromosomal aberrations behind shielding some ions have reduced effectiveness behind shielding and others increased, dependent on where on the RBE versus LET response curve the particle falls.

The importance of various GCR charge groups and energies in shielding material selection is dependent on the biological response model considered. However, these considerations are clouded by the uncertainties in such knowledge. Current radiobiological response models of cancer and other risks are not able to determine which shielding material is optimal under statistical tests that consider the uncertainties in such a calculation (Cucinotta, Kim, and Ren, 2006). A more recent concern is the possibility of nontargeted effects or other peculiarities of the response of humans to radiation (Barcellos-Hoff, Park, and Wright, 2005; Cucinotta and Chappell, 2010) which lead to a deviation from a linear response model; the value of radiation shielding and the importance of mission length are diminished if biological responses are sublinear with increasing doses and possibly increased if threshold doses occur.

Slowing down incident GCR particles using materials with a preponderance of energy loss due to ionization and a minimum probability of nuclear interactions is not always an optimal strategy. Nuclei such as carbon and oxygen, incident at high energy, have low LET, well beneath the peak value of RBE. When they lose energy in a shielding material (without suffering nuclear interactions), their LET increases. As a consequence, their RBE also increases instead of decreasing, so that they become more hazardous, rather than less hazardous. On the other hand, the LET of incident, high-energy heavier nuclei, such as iron, is close to the 150 keV/μm corresponding to the peak RBE. Losing energy and slowing down further increases their LET beyond the peak, yet they may become no more hazardous despite their higher LET due to the role of cell killing. Nuclear interactions that change a penetrating GCR nucleus into lighter nuclei, e.g., nuclear interactions that fragment Si into C and He (α particles), result in particles of lower RBE, the desired outcome. On the other hand, fragmentation of oxygen or carbon atoms in tissue into α particles produces particles near the maximum RBE of energies of just a few MeV. The fragmentation of high-LET iron into lower-LET chromium or silicon fragments changes the contribution to the radiation field from less hazardous particles, beyond the RBE peak, to more hazardous particles with an LET at or before the peak. A complicated picture emerges with many balances between increasing and decreasing energy deposition, and secondary projectile and targetlike nuclear fragments.

1. Shielding performance index

Aluminum structures have been the main stay of spacecraft. Also clear is the fact that hydrogen is certainly the optimal material for radiation protection. Materials with

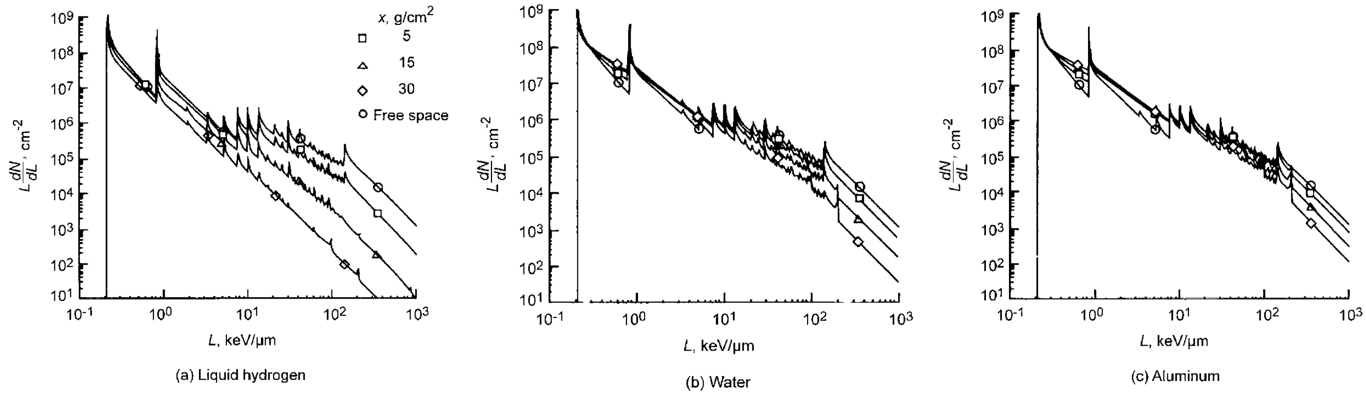

(a) Liquid hydrogen

(b) Water

(c) Aluminum

FIG. 34. Differential LET spectra from the HZETRN code for increasing amounts of liquid hydrogen, water, and aluminum shielding. From Wilson *et al.*, 1995.

atomic constituents heavier than aluminum such as steel or lead produce too many neutrons to be of interest for space radiation protection. With these ideas in mind, Wilson *et al.* (1993) devised a shielding performance index to bound material effectiveness relative to aluminum when considering different biological response models. Shield performance of a material m is defined relative to the standard aluminum technology by the shield performance index, which is the ratio of a risk assessment variable in aluminum to that of material m. Figure 36 shows the contributions from different GCR charge groups at solar minimum comparing the conventional systems using radiation quality factors to radiobiological models of cell killing, neoplastic transformation, and mouse tumors. Using these results, Fig. 37 shows the performance index relative to increasing aluminum shielding amounts. Performance indexes from 2 to more than 10 are possible with typical amounts of spacecraft shielding, although the calculations used only a minimal amount of tissue shielding and thus likely overestimate the performances. These results suggest that new high hydrogen content materials could provide significant benefits compared to aluminum, especially if amounts from 10 to 30 g/cm^2 could be afforded in vehicle designs.

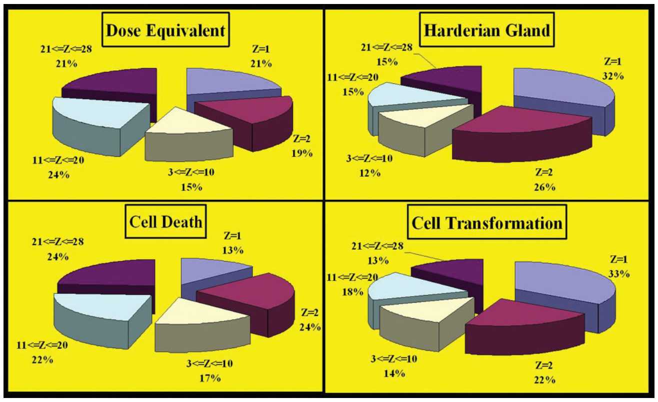

FIG. 36 (color). Several different measures of radiation quality calculations of different GCR charge groups to overall risk measures for 5 g/cm^2 of aluminum and no tissue shielding are shown. From NASA, 1998.

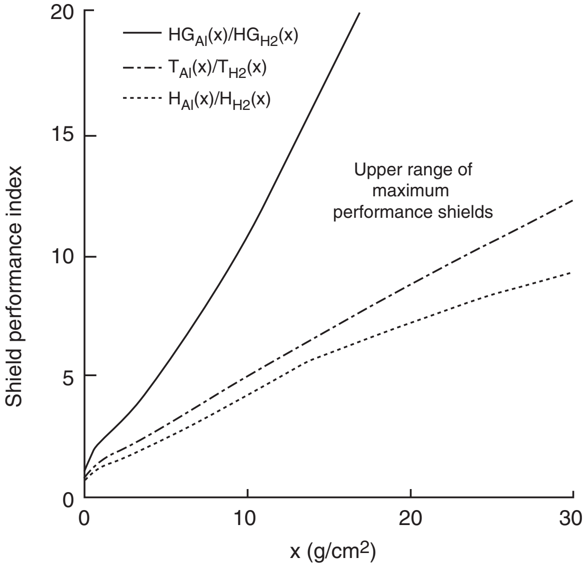

FIG. 37. Range of maximum performance index relative to liquid hydrogen relative to aluminum using various biological response models including Harderian gland tumors in mice (HG), transformation (T), and dose equivalent (H).

2. Uncertainty analysis

An uncertainty analysis using Monte Carlo propagation of errors from different factors that enter into a shielding calculation of cancer risks was developed by Cucinotta, Manual *et al.* (2001) and Cucinotta, Kim, and Ren (2006). Uncertainty factors considered are epidemiology data, dose-rate effects, radiation quality factors, and space physics. Probability distribution functions (PDF) representing the range of possible values for each factor are devised. The cancer risk projections for space missions are found by folding predictions of the tissue-weighted LET spectra behind spacecraft shielding dF/dL with the radiation cancer mortality rate to form a rate for a trial J:

$$m_J(E, a_E, a) = m_{lJ}(E, a_E, a) \int dL \frac{dF}{dL} L Q_{\text{trial}-J}(L) x_{L-J} \tag{39}$$

(not shown are the uncertainty quantiles associated with the low-LET mortality rate, m_{lJ}). The result of Eq. (39) is then used with the formula for the risk of exposure-induced death (REID) that considers a double-detriment life table for radiation cancer risk on top of the background of other causes of death in the U.S. population. After accumulating sufficient trials ($\sim 10^5$), the results for the REID estimates are binned and the median values and confidence intervals found. A χ^2 test for determining if PDFs for two distinct shielding configurations or materials are significantly different was developed (Cucinotta, Kim, and Ren, 2006). They denoted the calculated PDFs for a REID of R_i for two configurations or materials as $p_1(R_i)$ and $p_2(R_i)$, respectively. Each $p(R_i)$ follows a Poisson distribution with variance $\sqrt{p(R_i)}$. The χ^2 test for characterizing the dispersion between the two distributions is then

$$\chi^2 = \sum_n \frac{[p_1(R_n) - p_2(R_n)]^2}{\sqrt{p_1^2(R_n) + p_2^2(R_n)}}. \tag{40}$$

Once χ^2 is determined, the probability $P(n, \chi^2)$ that the two distributions are drawn from the same parent distribution is calculated. If χ^2 is sufficiently large such that $P(n, \chi^2)$ is less than about 20% is an indication that we can conclude that the two distributions lead to distinct cancer risks from GCR and/or SPEs, with the material with the lowest mean and upper 95% CI (confidence interval) values preferred for radiation protection. However, the opposite result indicates either that the materials are approximately the same or that the uncertainties in risk models prevent us from concluding that the configuration or material is superior for radiation protection properties. Cucinotta, Kim, and Ren (2006) evaluated χ^2 for the LET-dependent parts of the uncertainties (quality factors and physics) separately, since only these

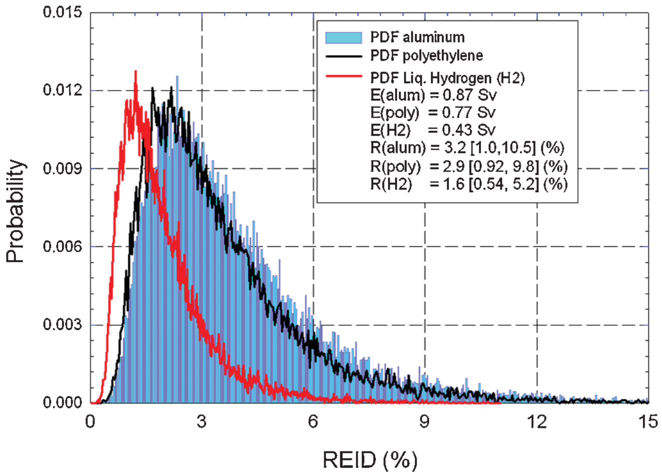

FIG. 38 (color). PDFs for fatal cancer risk probability for 40-year-old males on a 600-day Mars swing-by mission with 20 g/cm^2 shielding of aluminum, polyethylene, or liquid hydrogen. Effective doses and point estimates or 95% CI for risk of exposure-induced death (REID) are shown in the box. From Cucinotta, Kim, and Ren, 2006.

contributions explicitly depend on the modification of radiation fields by shielding.

Figure 38 shows PDFs for the GCR as solar minimum for aluminum, polyethylene, and liquid hydrogen shielding with areal density of 20 g/cm^2. Table VII shows results for the χ^2 statistic comparing polyethylene and hydrogen shielding effectiveness to aluminum. The August 1972 SPE is considered for these comparisons. As shown by Fig. 30, large variations will occur in risk estimates for specific events; however, the August 1972 SPE provides a good model for a large event. For calculations that ignore the low-LET risk coefficient uncertainties, near solar maximum with a large SPE, significant results ($P < 0.01$) are found for liquid hydrogen, and for the GCR at solar minimum (with $P < 0.15$). We conclude that because of the modest differences between polyethylene and aluminum as GCR absorbers, and the large radiobiological uncertainties in cancer risk projection models, the benefits of polyethylene compared to aluminum shielding for GCR cannot be proven at this time. A key factor in these results is that although aluminum is a greater producer of secondary radiation compared to polyethylene, tissue shielding "equalizes" much of these differences.

3. Novel and *in situ* shielding materials

Polyethylene has been identified as a useful structural polymer for spacecraft shielding with various fabrication strategies developed for damage tolerant stiff structure and inflatable vehicles (Wilson *et al.*, 1991). An important challenge is how to form high-density polyethylene fiber with polyethylene matrix and bond the resulting composite face sheets to form polyethylene foams. Approaches considered

TABLE VII. From Cucinotta, Kim, and Ren (2006). χ^2 test at solar minimum for 20 g/cm^2 shields for 40-yr males on a Mars swing-by mission. $P(n, \chi^2)$ is the probability materials cannot be determined to be significantly different ($n = 500$). Values in bold for $P(n, \chi^2) < 0.2$ indicate a significant improvement over aluminum.

Test material	E (Sv)	REID (%)	95% CI	χ^2/n	$P(n, \chi^2)$
			All uncertainties		
Aluminum	0.87	3.2	[1.0, 10.5]	· · ·	· · ·
Polyethylene	0.78	2.9	[0.94, 9.2]	0.05	>0.99
Hydrogen	0.43	1.6	[0.52, 5.1]	0.63	>0.99
			LET-dependent uncertainties		
Aluminum	0.87	3.2	[1.9, 8.7]	· · ·	· · ·
Polyethylene	0.78	2.9	[1.8, 7.5]	0.08	>0.99
Hydrogen	0.43	1.7	[1.0, 4.2]	**1.10**	**<0.15**
Same as a near solar maximum for 5 g/cm^2 shields.					
Test material	E (Sv)	REID (%)	95% CI	χ^2/n	$P(n, \chi^2)$
			All uncertainties		
Aluminum	1.21	4.4	[1.5, 13.1]	· · ·	· · ·
Polyethylene	0.94	3.5	[1.2, 10.8]	0.14	>0.99
Hydrogen	0.52	2.1	[0.60, 6.4]	0.81	>0.99
			LET-dependent uncertainties		
Aluminum	1.21	4.4	[3.0. 11.0]	· · ·	· · ·
Polyethylene	0.94	3.5	[2.3, 8.8]	0.32	>0.99
Hydrogen	0.52	2.1	[1.2, 5.2]	**1.38**	**<0.001**
Same as a near solar maximum for 20 g/cm^2 shields.					
Test material	E (Sv)	REID (%)	95% CI	χ^2/n	$P(n, \chi^2)$
			All uncertainties		
Aluminum	0.54	2.0	[0.60, 6.8]	· · ·	· · ·
Polyethylene	0.45	1.7	[0.52, 5.6]	0.08	>0.99
Hydrogen	0.24	0.9	[0.27, 2.9]	0.77	>0.99
			LET-dependent uncertainties		
Aluminum	0.54	2.0	[1.2, 5.6]	· · ·	· · ·
Polyethylene	0.45	1.7	[1.0, 4.6]	0.15	>0.99
Hydrogen	0.24	0.9	[0.52, 2.4]	**1.26**	**<0.005**

are plastic thermosets, aliphatic systems, and *e*-beam curing. Aliphatic systems lose strength at both low and high temperatures to be expected under space conditions. Wilson, Cucinotta, and Schimmerling (2004) discussed the usage of aliphatic and aromatic hybrid polymers as an improvement to a purely aliphatic system. Carbon nanotubes with high hydrogen content offer a distinct approach and are under investigation for improved structural layouts.

The high costs of launch mass make *in situ* shielding on the lunar or Mars surface of interest. Distinct approaches may be required since a higher relative fraction of astronaut exposures on the Mars surface are due to neutrons compared to the lunar surface due to the Mars atmosphere both depleting heavy ions and adding neutrons. The exposure to astronauts will depend on which region of Mars a habitat occupies (Wilson, Clowdsley *et al.*, 2004), because large variations in secondary neutrons can occur due to the soil composition as well as seasonal variations due to the presence of protective ice (water or permafrost) as shown in Fig. 39. Landing sites will likely be chosen by science requirements; however, they may require distinct shielding approaches dependent on the fractional contribution from neutrons to the total risk. Digging regolith to shield planetary habitats with take-along equipment is one approach considered. Certainly, exposures could be reduced substantially if several meters of regolith are used to cover a habitat. However, long times spent within habitats will likely reduce the science objectives of such missions. The Moon is known to contain lava tubes as well as craters that partially shield space radiation, and Mars has similar geographical features to increase habitat shielding. *In situ* hydrogen or perhaps launched boron could be used to create regolith shielding bricks; however, they will require new manufacturing approaches on planetary surfaces.

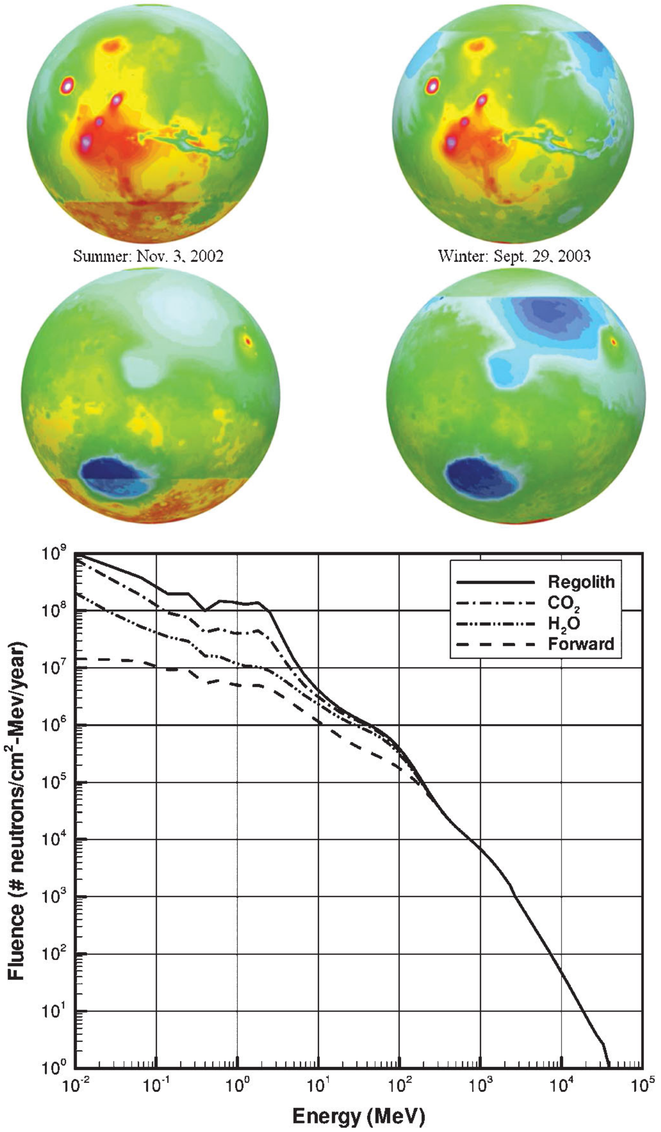

FIG. 39 (color). Neutron doses on Mars. Variations in charged particle doses are caused by the atmospheric height in different geometric locations, whose maps were measured by the MOLA altimeter on the Mars Global Surveyor spacecraft, launched in 1996. The upper panel shows the seasonal variation of the integral neutron fluence above 10 MeV due to ice buildup reducing regolith back-scattered neutrons. The bottom plot shows the forward and backward neutron fluences for different Mars soil compositions. From Wilson, Clowdsley *et al.*, 2004.

C. Active shielding

Active shielding involves the generation of electromagnetic fields to deflect space radiation. Several approaches have been proposed (Townsend, 2001) as follows: (1) electrostatic shield, (2) plasma shield, (3) confined magnetic field, and (4) unconfined magnetic fields.

Each approach should be considered relative to passive shielding in terms of effectiveness as well as power and mass requirements and the possibility of device failure. Also, harmful effects need to be considered including biological effects of strong magnetic field on humans, and the disturbing of lunar dust, which contains nanophase iron (ASEB, 2008) from the electromagnetic field. Lunar dust was reported to irritate the skin and respiratory systems of the Apollo astronauts.

Developments in superconducting magnets are necessary to provide effective active shielding from GCR. The experience gained during the development of the alpha magnetic spectrometer (AMS) superconducting magnet has been useful to develop ideas and techniques to be applied to radiation shield for exploration missions (Battiston, 2007, 2008). However, an anomalous heating of the cryogenic superconducting magnet eventually forced the AMS Collaboration to exchange the superconducting AMS-02 magnet (Blau *et al.*, 2004) to the previously developed, less sensitive, permanent magnet. This permanent magnet has been delivered to ISS by the Space Shuttle Endeavor on 16 May 2011, and is now operating in its search for antimatter. During the development of the cryogenic superconducting magnet (2 coils of Ni-Ti operating at 1.8 K, generating a field of 0.87 T in the center), the AMS Collaboration proposed conceptual designs of magnetic configuration optimized for a travel to Mars or for a Moon base, with toroidal configurations able to provide a zero-magnetic field inside the spacecraft. However, the experience of the AMS Collaboration also shows that the cryogenic superconducting magnet technique is critical for spaceflight and presently not yet reliable. In the future, cryogen-free superconductors could provide excellent solutions, pending technological improvements in this field.

As an example magnetic lenses built from superconducting magnets have been described by Spillantini et al. (2007) for protection from directional SPE-type radiation. An angular cone ±10° could protect a several cubic meter volume against protons with energies up to about 200 MeV using a so-called D-shaped toroid field with a devise mass of about 1100 kg, which is in the range of the mass required by a passive shielding storm shelter to protect the same volume. However, the directionality of the field is a disadvantage compared to passive shielding.

Recently, renewed interest in electrostatic shielding has led to several possible designs. The model described by Tripathi, Wilson, and Younquist (2008) illustrates many of the problems with such approaches. Tripathi, Wilson, and Younquist (2008) described a lunar base electrostatic shield made of 12 spheres: 6 of 20 m radius located 160 m from the habitat along several axes, and a 6 of 10 m radius located 50 m along 50 m away from the habitat. Each sphere carries a +300 MV charge. The resulting configuration was shown to reduce the GCR dose equivalent at the surface of the skin by about two-thirds. A smaller reduction would be found at the deep seated organ due to the buildup of target fragments from the residual high-energy GCR nuclei. The mass of shields approached that of the habitat and therefore comes at a very high launch cost, perhaps of interest for a permanent moon base. These possibilities will require very large power requirements, and nuclear powered reactors are a useful option.

V. SPACE RADIATION EFFECTS

A. Biological effects

Most of the uncertainty on space radiation risk is associated with poor knowledge of the biological effects of cosmic rays. In particular, gaps in knowledge are mostly related to the following:

- relative biological effectiveness factors of energetic heavy ions for late effects, both cancer and noncancer;
- dose and dose-rate reduction effectiveness factors;
- errors in human data including statistical, dosimetry, and transfer between populations in application to space radiation risks;
- effects of the exposure to the mixed high- and low-LET space radiation field;
- shape of the dose-response curve at low doses for charged particles;
- and interaction of radiation damage with other space environment stressors (particularly microgravity).

The main biological effects associated with exposure to cosmic radiation are as follows:

- carcinogenesis,
- late degenerative tissue effects,
- acute effects, and
- hereditary effects.

Cancer is currently dominating risk estimates, and as discussed the dose limits are most constraints by cancer mortality risk. However, noncancer effects are becoming an increasing source of concern. They can again be divided into

- acute and late damage to the CNS,
  cataract formation,
- cardiovascular diseases including coronary heart disease and stroke.
- digestive and respiratory diseases,
- and accelerated senescence leading to endocrine and immune system dysfunction.

Acute effects are expected only for very intense SPE hitting an unprotected crew. The prodromal risks such as nausea, vomiting, and fatigue are the most likely (Hu et al., 2009), and acute mortality is very improbable. Hereditary effects are generally assumed to be a factor of 10 or more lower than somatic effects in radiation protection, although there is missing evidence for heavy ions in this field. The age at flight and the small number of astronauts tend to reduce the importance of hereditary and reproductive effects.

Interestingly, so far the cataract is the only cosmic radiation-induced effect actually observed in astronauts (Cucinotta, Manual et al., 2001; Chylack et al., 2009). Recent epidemiological evidence does not support the existence of dose threshold for radiation-induced lens opacification, although the shape of the dose-response curve is still unclear (Blakely et al., 2010). However, animal studies show that the RBE of heavy ions for cataract induction is as high as 50 at doses below 100 mGy (Brenner et al., 1991), thus explaining the high effectiveness for accelerated caratactogenesis in space.

The RBE represents a major source of uncertainty, and indeed the problem of radiation quality is central in radiation protection on Earth as well. The shape of the dose-response curve at low doses is a key problem, and the importance of nontargeted effects or adaptive response mechanisms is still unclear both for radiation protection on Earth (Mullenders et al., 2009) and in space (Cucinotta and Durante, 2006; Cucinotta and Chappell, 2010). Conventional risk assessment approaches have been limited to using averaged quantities such as dose or dose equivalent. The stochastic models of nuclear reactions and track structure described in Sec. III will be needed to fully utilize the results of radiobiology experiments and to develop new stochastic based disease models to replace the oversimplifications embodied in the conventional RBE approach.

The large number of health risks of concern, entailing many tissues and diseases, complicates pursuing approaches such as genetic selection, because it is highly unlikely that one person could be resistant to so many diseases. Approaches to biological countermeasures are also challenged by the multitude of health risks as well as the types of radiation in space and the chronic exposure of up to 3 years for a Mars mission. These factors limit the applicability of radio-protectors developed for terrestrial exposures, which are usually for acute exposures to low-LET radiation.

Large ground-based radiobiology research experimental programs are currently ongoing to reduce uncertainty on biological effects of heavy ions, in the USA (at the NASA Space Radiation Laboratory in the Brookhaven National Laboratory, NY), Europe (at GSI in Darmstadt, Germany), and Japan (at HIMAC in Chiba). Results from these experiments have been reviewed (NCRP, 2000; Durante, 2002; ESA, 2006; NCRP, 2006; Cucinotta and Durante, 2006; Durante and Cucinotta, 2008; NASA, 2009; Maalouf, Durante, and Foray, 2011), and the interested reader will find all of the most updated biological information in those papers.

B. Effects on microelectronics

The effects of cosmic radiation on microelectronics are also a major concern for the safety in spaceflight. In fact, the charge generated by the ionization of energetic charged particles in spacecraft electronics can upset microcircuit functions and eventually lead to catastrophic failures.

HZE damage is caused by electron-hole pairs that are generated in silicon dioxide and other insulators (McNulty *et al.*, 1996; Holmes-Siedle and Adams, 2002). Proton- and neutron-induced single-event effects are generally caused by nuclear reaction fragments produced in the semiconductor, typically spallation nucleons and Si recoils (Tang, 2005). The damage in the integrated circuit is the result of trapping of excess charges at or near the interface region between the oxide (or other insulator) and semiconductor. The effect depends on the particle charge and energy, and on how excess electron-hole pairs are transported within the oxide. When low electric fields are present in the oxide, recombination reduces the pairs transported to critical interface regions (charge yield). If the charge yield is low, then the net effect of the deposited dose is reduced. If the charge yield is high enough, it can induce destructive effects (single-event latchup, single-event gate rupture, single-event burnout, single-event dielectric rupture, and single-event snapback) or nondestructive effects (single-event upset, single-event transient, single-event functional interrupt, and single-event hard errors).

Single-event upset (SEU), or "soft errors," are the most common space radiation-induced effects, and they occur also in our terrestrial computers. It is a change of state (bit flip) affecting bipolar and metal-oxide-semiconductor elements. As noted, SEU are nondestructive, i.e., the bit flip can be corrected by rewriting the affected element, but they can still represent a threat to spacecraft electronics. Microelectronic failures or multiple-bit error rates generated serious problems in several missions, including Cassini and the Hubble telescope. Since they represent a major issue in the design of any kind of space mission, these effects have been reviewed several times [see, e.g.,Iniewski (2010), and the reader can consult the literature for specialized information]. What is particularly interesting from the physical point of view, and in a way similar to the problem of biological effects, is the dependence of SEU from the energy and charge.

Before electronic components can be sent into space, they have to be qualified on Earth. These tests are usually done using γ rays (for total dose effects) or at low-energy accelerator facilities (for SEU). The vulnerability of a device to SEU is normally defined by a threshold LET (minimum LET required to produce SEU) and the saturated cross section (maximum upset rate for the device, when no increase is observed by further increasing the LET). But, as for the biological effect, LET alone may not be the only parameter characterizing the effect. Below the LET threshold, nuclear reactions can still produce SEU, and high-energy ions are more effective than low-energy ions (Dodd *et al.*, 2007). On the other hand, recent studies using particles at energies around 1 GeV/nucleon suggest that above the LET threshold and before saturation, the cross section is higher for low-energy ions compared to relativistic HZE at the same LET (Connell *et al.*, 1996; Metzger *et al.*, 2011), a track-structure effect (see Sec. III.E) also observed for inactivation of viruses (Butts and Katz, 1967) and mammalian cells (Katz *et al.*, 1971; Cucinotta, Wilson *et al.*, 1996; Elsässer *et al.*, 2010) by heavy ions. Tests at high-energy accelerators are also preferable because the particles can cross the whole device and allow testing the device at different tilt angles (Pellish *et al.*, 2010; Metzger *et al.*, 2011). High-energy spallation sources can also be used for neutron-induced SEU testing.

VI. CONCLUSIONS

Along with biomedical research, efforts in nuclear, particle, and radiation physics are essential to the success of future exploration missions to Mars and other destinations. There are many areas where physics takes a lead role in risk assessment for astronauts, including the translation from radiobiology and biophysics into radiation protection methods and spacecraft design. Radiation physics has shown that shielding should be successful for SPE protection and how to optimize approaches in order to reduce costs and improve safety factors. Physics has also taken the lead in determining how poorly shielding approaches against GCR work, based on the detailed understanding of nuclear reactions and secondary radiation that occur from the passage of protons and HZE nuclei in all materials including tissue. Analysis also indicates that active shielding using magnetic fields and electrostatics is severely challenged for GCR, yet continues to be of interest because of the potentially high payoff.

Existing radiation transport codes agree with measurements of organ dose equivalents within 20%; however, further improvements in transport codes are of interest. Future work will continue to improve knowledge of interaction cross sections and their usage in space radiation transport codes. Many cross-section data sets have been determined; however, there are still significant gaps in double-differential cross sections for light particle production, cross sections for new materials of interest, and knowledge of exclusive cross sections that is needed to support stochastic based risk models that supplant the current deterministic dose based quantities. The description of energy deposition in biomolecules due to nuclear processes or δ rays as mapped to tissue and organ structures is needed to support new risk assessment approaches as well. In parallel, robotic precursor missions to the surface of Mars and other near Earth objects sample the environment with particle detectors and dosimetry prior to the arrival of future explores. Transport codes and energy deposition models play essential roles in the understanding of these new data sets.

ACKNOWLEDGMENTS

Research on space radiation protection at GSI is partially supported by the European Space Agency (IBER contract) and by Beilstein Stiftung (NanoBIC contract). Space radiation activities at NASA are supported by the NASA Space Radiation Program. We thank Svetlana Ktitareva for editing the manuscript, Dr. Myung-Hee Kim for help with figures, and Dr. Emanuele Scifoni for useful discussions.

REFERENCES

Aghara, S. K., S. R. Blattnig, J. W. Norbury, and R. C. Singleterry, 2009, Nucl. Instrum. Methods Phys. Res., Sect. B **267**, 1115.

Agostinelli, S., *et al.*, 2003, Nucl. Instrum. Methods Phys. Res., Sect. A **506**, 250.

Alard, J. P., *et al.*, 1987, Nucl. Instrum. Methods Phys. Res., Sect. A **261**, 379.

Alsmiller, R. G., D. C. Irving, W. E. Kinney, and H. S. Moran, 1965, *Proceedings of the Second Symposium on Protection Against Radiations in Space* (NASA SP-71), p. 177.

ASEB, 2008, *Aeronautics and Space Engineering Board, Managing Space Radiation Risks in the Era of Space Exploration* (National Academy of Sciences Press, Washington, DC).

Atwell, W., 1994, Adv. Space Res. **14**, 415.

Badhwar, G. D., 2004, Space Sci. Rev. **110**, 131.

Badhwar, G. D., W. Atwell, F. F. Badavi, T. C. Yang, and T. F. Cleghorn, 2002, Radiat. Res. **157**, 76.

Badhwar, G. D., F. A. Cucinotta, and P. M. O'Neill, 1993, Radiat. Res. **134**, 9.

Badhwar, G. D., J. E. Keith, and T. F. Cleghorn, 2001, Radiation Measurements **33**, 235.

Badhwar, G. D., and P. M. O'Neill, 1992, Nucl. Tracks Radiat. Meas. **20**, 403.

Badhwar, G. D., and P. M. O'Neill, 1994, Adv. Space Res. **14**, 749.

Badhwar, G. D., J. U. Patel, F. A. Cucinotta, and J. W. Wilson, 1995, Radiation Measurements **24**, 129.

Ballarini, F., *et al.*, 2007, Adv. Space Res. **40**, 1339.

Band, D., 1993, Astrophys. J. **413**, 281.

Barber, R. E., F. A. Cucinotta, H. Nikjoo, G. D. Qualls, and J. W. Wilson, 2001, SAE/ICES 2001-01-2371.

Barcellos-Hoff, M. H., C. Park, and E. G. Wright, 2005, Nat. Rev. Cancer **5**, 867.

Battiston, R., 2007, Nucl. Phys. B, Proc. Suppl. **166**, 19.

Battiston, R., 2008, Nucl. Instrum. Methods Phys. Res., Sect. A **588**, 227.

Battistoni, G., *et al.*, 2008, Nucl. Phys. B, Proc. Suppl. **175–176**, 88.

Belli, M., F. Cera, R. Cherubini, A. M. I. Haque, F. Ianzini, G. Moschini, O. Sapora, G. Simone, M. A. Tabocchini, and P. Tiverton, 1993, Int. J. Radiat. Biol. **63**, 331.

Benton, E. R., and E. V. Benton, 2001, Nucl. Instrum. Methods Phys. Res., Sect. B **184**, 255.

Bichsel, H., 1992, Phys. Rev. A **46**, 5761.

Billings, M. P., W. R. Yucker, and B. R. Heckman, 1973, *Body Self-Shielding Data Analysis* (McDonald Douglas Astronautics Company West), MDC-G4131.

Blakely, E. A., *et al.*, 2010, Radiat. Res. **173**, 709.

Blattnig, S. R., J. W. Norbury, R. B. Norman, J. W. Wilson, R. C. Singleterry, and R. Tripathi, 2004, "MESTRN: A Deterministic Mesons-Muon Transport Code for Space Radiation," NASA Technical Report No. TM-2004-212995 (National Aeronautics and Space Administration, Washington, DC).

Blau, B., S. M. Harrison, H. Hofer, S. R. Milward, G. Kaiser, J. S. H. Ross, S. C. C. Ting, and J. Ulbricht, 2004, Nucl. Instrum. Methods Phys. Res., Sect. A **518**, 139.

Bradt, H. L., and B. Peters, 1950, Phys. Rev. **77**, 54.

Brandt, W., and H. R. Ritchie, 1974, Primary Processes in the Physical Stage (Tech. Info. Center, US, Atomic Energy Commission), p. 20.

Brechtmann, C., and W. Heinrich, 1988, Z. Phys. A **331**, 463.

Brenner, D. J., *et al.*, 2003, Proc. Natl. Acad. Sci. U.S.A. **100**, 13761.

Brenner, D. J., C. Medvedovsky, Y. Huang, G. R. Merriam, and B. V. Worgul, 1991, Radiat. Res. **128**, 73.

Butts, J. J., and R. Katz, 1967, Radiat. Res. **30**, 855.

Carlsson, J., and K. Rosander, 1973, Phys. Med. Biol., **18**, 633.

Casolino, M., *et al.*, 2007, Adv. Space Res. **40**, 1746.

Chang-Diaz, F., 2000, Sci. Am. **283**, 90.

Chatterjee, A., and H. J. Schaefer, 1976, Radiat. Environ. Biophys. **13**, 215.

Chen, J., D. Chenette, R. Clark, M. Garcia-Munoz, T. K. Guzik, K. R. Pyle, Y. Snag, and P. J. Wefel, 1994, Adv. Space Res. **14**, 765.

Chylack, L. T., L. E. Peterson, A. H. Feiveson, M. L. Wear, F. K. Manuel, W. H. Tung, D. S. Hardy, L. J. Marak, and F. Cucinotta, 2009, Radiat. Res. **172**, 10.

Cleghorn, T. F., P. B. Saganti, C. J. Zeitlin, and F. A. Cucinotta, 2004, Adv. Space Res. **33**, 2215.

Cliver, E. W., 2006, Adv. Space Res. **38**, 119.

Clowdsley, M. S., J. W. Wilson, M.-H. Y. Kim, R. C. Singleterry, R. K. Tripathi, J. H. Heinbocke, F. F. Badavi, and J. L. Shinn, 2001, Physica Medica **17**, 94, Supplement 1.

Connell, L. W., F. W. Sexton, P. J. McDaniel, and A. K. Prinja, 1996, IEEE Trans. Nucl. Sci. **43**, 2814.

Cronin, J. W., 1999, Rev. Mod. Phys. **71**, S165.

Cucinotta, F. A., S. Hu, N. A. Schwadron, K. Kozarev, L. W. Townsend, and M.-H. Y. Kim, 2010, Space Weather **8**, S00E09.

Cucinotta, F. A., I. Plante, A. Ponomarev, and M. Y. Kim, 2011, Radiation Protection Dosimetry **143**, 384.

Cucinotta, F. A., and L. J. Chappell, 2010, Mutat. Res. **687**, 49.

Cucinotta, F. A., and R. R. Dubey, 1994, Phys. Rev. C **50**, 1090.

Cucinotta, F. A., and M. Durante, 2006, Lancet Oncol. **7**, 431.

Cucinotta, F. A., M. H. Kim, V. Willingham, and K. George, 2008, Radiat. Res. **170**, 127.

Cucinotta, F. A., M. Y. Kim, and L. Ren, 2006, Radiation Measurements **41**, 1173.

Cucinotta, F. A., M. Y. Kim, S. I. Schneider, and D. M. Hassler, 2007, Radiat. Environ. Biophys. **46**, 101.

Cucinotta, F. A., F. K. Manuel, J. Jones, G. Iszard, J. Murrey, B. Djojonegro, and M. Wear, 2001, Radiat. Res. **156**, 460.

Cucinotta, F. A., H. Nikjoo, and D. T. Goodhead, 1999, Radiat. Environ. Biophys. **38**, 81.

Cucinotta, F. A., J. W. Wilson, J. R. Williams, and J. F. Dicello, 2000, Radiat. Meas. **32**, 181.

Cucinotta, F. A., H. Nikjoo, and D. T. Goodhead, 2000, Radiat. Res. **153**, 459.

Cucinotta, F. A., W. Schimmerling, L. E. Peterson, J. W. Wilson, G. D. Badhwar, P. Saganti, and J. F. Dicello, 2001, Radiat. Res. **156**, 682.

Cucinotta, F. A., L. W. Townsend, and J. W. Wilson, 1992, Phys. Lett. B **282**, 1.

Cucinotta, F. A., L. W. Townsend, J. W. Wilson, J. L. Shinn, G. D. Badhwar, and R. R. Dubey, 1996, Adv. Space Res. **17**, 77.

Cucinotta, F. A., J. W. Wilson, P. Saganti, X. Hu, M. Y. Kim, T. Cleghorn, C. Zeitlin, and R. K. Tripathi, 2006, Radiation Measurements **41**, 1235.

Cucinotta, F. A., J. W. Wilson, M. R. Shavers, and R. Katz, 1996, Int. J. Radiat. Biol. **69**, 593.

Cucinotta, F. A., J. W. Wilson, R. K. Tripathi, and L. W. Townsend, 1998, Adv. Space Res. **22**, 533.

Cucinotta, F. A., H. Wu, M. R. Shavers, and K. George, 2003, Gravit. Space Biol. Bull. **16**, 11 [http://www.ncbi.nlm.nih.gov/pubmed?term=cucinotta%20shavers%20george].

Cugnon, J., C. Volant, and S. Vuillier, 1997, Nucl. Phys. **A620**, 475.

Cummings, J. R., W. R. Binns, M. H. Garrand, M. H. Israel, J. Klarmann, E. C. Stone, and C. J. Waddington, 1990, Phys. Rev. C **42**, 2508.

Czyz, W., and L. Maximon, 1969, Ann. Phys. (N.Y.) **52**, 59.

Dachev, T., B. Tomov, P. Dimitrov, and Y. Matvichuk, 2009, Curr. Sci. **96**, 544 [http://www.ias.ac.in/currsci/feb252009/544.pdf].

De Angelis, G., B.M. Anderson, W. Atwell, J.E. Nealy, G.D. Qualls, and J.W. Wilson, 2004, J. Radiat. Res. **45**, 1.

Dodd, P., *et al.*, 2007, IEEE Trans. Nucl. Sci. **54**, 2303.

Durante, M., 2002, Riv. Nuovo Cimento Soc. Ital. Fis. **25**, 1 [http://paperseek.sif.it/index.php?journal=ncr&issue=08&year=2002&month=August&issuetitle=&vol=025&action=browse].

Durante, M., and C. Bruno, 2010, Eur. Phys. J. D **60**, 215.

Durante, M., and F.A. Cucinotta, 2008, Nat. Rev. Cancer **8**, 465.

Durante, M., K. George, G. Gialanella, G. Grossi, C.L. Tessa, L. Manti, J. Miller, M. Pugliese, P. Scampoli, and F.A. Cucinotta, 2005, Radiat. Res. **164**, 571.

Elsässer, T., *et al.*, 2010, Int. J. Radiat. Oncol. Biol. Phys. **78**, 1177.

ESA, 2003, HUMEX: Study on the Survivability and Adaptation of Humans to Long-Duration Interplanetary and Planetary Environments, Report No. ESA-ESTEC SP-1264.

ESA, 2006, Investigation on Biological Effects of Space Radiation (IBER) Study Final Report ESA publication CR-P-4585.

ESA, 2007, European Objectives and Interests in Space Exploration, ESA Strategy & Architecture Office.

Faddeev, D., 1956, *Mathematical Aspects of the Three-Body Problem in Quantum Scattering Theory* (I1 DanieliDavey and Co., Inc., New York).

Fano, U., 1963, Annu. Rev. Nucl. Sci. **13**, 1.

Fazel, R., H.M. Krumholz, Y. Wang, J.S. Ross, J. Chen, H.H. Ting, N.D. Shah, K. Nasir, A.J. Einstein, and B.K. Nallamothu, 2009, N. Engl. J. Med. **361**, 849.

Fermi, E., 1940, *Summer Lectures* (University of Chicago, Chicago, IL).

Ferrari, A., and P. Sala, 1996, ATLAS Note Phys-No-086, CERN, Geneva, Switzerland.

Feynman, J., G. Spitale, J. Wang, and S. Gabriel, 1993, J. Geophys. Res. **98**, 13 281.

Flesch, F., S.E. Hirzebruch, G. Huntrup, H.R.T. Streibel, E. Winkel, and W. Heinrich, 1999, Radiation Measurements **31**, 533.

Flesch, F., G. Iancu, W. Heinrich, and H. Yasuda, 2001, Radiation Measurements **34**, 237.

Glauber, R.J., 2006, Rev. Mod. Phys. **78**, 1267.

Goldhaber, A.S., 1974, Phys. Lett. **53B**, 306.

Goodhead, D.T., 1995, Radiat. Environ. Biophys. **34**, 67.

Goodhead, D.T., and H. Nikjoo, 1989, Int. J. Radiat. Biol. **55**, 513.

Heinbockel, J.H., *et al.*, 2011a, Adv. Space Res. **47**, 1079.

Heinbockel, J.H., *et al.*, 2011b, Adv. Space Res. **47**, 1089.

Heynderickx, D., B. Quaghebeur, J. Wera, E. Daly, and H. Evans, 2004, Space Weather **2**, S10S03.

HLEG, 2009, Report of the High-Level Expert Group on the European Low-Dose Risk Research (EU).

Holmes-Siedle, A., and L. Adams, 2002, *Handbook of Radiation Effects* (Oxford University Press, Oxford, UK).

Hu, S., M.Y. Kim, McClellan, and F.A. Cucinotta, 2009, Health Phys. **96**, 465.

Hufner, J., 1985, Phys. Rep. **125**, 129.

Hufner, J., K. Schafer, and B. Schurmann, 1975, Phys. Rev. C **12**, 1888.

Hughes, H., R. Prael, and R. Little, 1997, X-Division Research Note XTM-RN(U)97-012, Los Alamos National Laboratory, LA-UR-97-4891.

Iancu, G., F. Flesch, and Q. Heinrich, 2005, Radiation Measurements **39**, 525.

ICRP, 1977, Publication 21. Ann. ICRP 1.

ICRP, 1991, Publication 60. Ann. ICRP 21.

ICRP, 2007, Publication 103. Ann. ICRP 37.

ICRU, 1993, Report No. 51, Oxford University Press, Cary, NC.

ICRU, 2000, Report No. 63 (International Commission on Radiation Units and Measurements, Bethesda, MD).

Iniewski, K., 2010, *Radiation Effects in Semiconductors* (CRC Press, Taylor & Francis, London, UK).

James, M.R., G.W. McKinney, J.S. Hendricks, and M. Moyers, 2006, Nucl. Instrum. Methods Phys. Res., Sect. A **562**, 819.

Katz, R., B. Ackerson, M. Homayoonfar, and S.C. Scharma, 1971, Radiat. Res. **47**, 402.

Katz, R., S. Scharma, and M. Homayoonfar, 1972, *Topics in Radiation Dosimetry, Radiation Dosimetry Supplement 1*, edited by F.H. Attix (Academic Press, NY), p. 317.

Kim, M.Y.H., M.J. Hayat, A.H. Feiveson, and F.A. Cucinotta, 2009a, Health Phys. **97**, 68.

Kim, M.Y.H., M.J. Hayat, A.H. Feiveson, and F.A. Cucinotta, 2009b, Adv. Space Res. **44**, 1428.

King, J.H., 1974, J. Spacecr. Rockets **11**, 401.

Kobetich, E.J., and R. Katz, 1968, Phys. Rev. **170**, 257.

Koshiishi, H., H. Matsumoto, A. Chishiki, T. Goka, and T. Omodaka, 2007, Radiation Measurements **42**, 1510.

Krämer, M., and M. Durante, 2010, Eur. Phys. J. D **60**, 195.

Krämer, M., and G. Kraft, 1994, Radiat. Environ. Biophys. **33**, 91.

Maalouf, M., M. Durante, and N. Foray, 2011, J. Radiat. Res. **52**, 126.

Maung, K.M., J.W. Norbury, and D.E. Kahana, 1996, J. Phys. G **22**, 315.

McCracken, K.G., G.A.M. Dreschhoff, E.J. Zeller, D.F. Smart, and M.A. Shea, 2001, J. Geophys. Res. **106**, 21 585.

McGuire, R.E., T.T. von Rosenvinge, and F.B. McDonald, 1986, Astrophys. J. **301**, 938.

McNulty, P.J., R.A. Reed, W.J. Beavaius, and D.R. Roth, 1996, IEEE Trans. Nucl. Sci. **NS-43**, 397 [http://ieeexplore.ieee.org/xpl/freeabs_all.jsp?arnumber=509809].

Metropolis, N., R. Bivinis, M. Storm, J.M. Miller, and G. Friedlander, 1958, Phys. Rev. **110**, 204.

Metzger, S., *et al.*, 2011, Investigation of Single Event Effects with Very High Energy Ions, GSI Report No. 2011-1, p. 1438.

Mitrofanov, I., *et al.*, 2009, Space Sci. Rev. **150**, 183.

Mullenders, L., M. Atkinson, H. Paretzke, L. Sabatier, and S. Bouffler, 2009, Nat. Rev. Cancer **9**, 596.

Narici, L., 2008, New J. Phys. **10**, 075010.

NASA, 1998 (NASA HQ, Washington, DC).

NASA, 2005, NASA/SP-2004-6113.

NASA, 2009, NASA/SP-2009-3405.

NCRP, 2000, Report No. 132 (NCRP, Bethesda, MD).

NCRP, 2002 (NCRP, Bethesda, MD).

NCRP, 2006, Report No. 153 (NCRP, Bethesda, MD).

Neise, L., M. Berenguer, C. Hartnack, G. Peilert, H. Stoecker, and W. Greiner, 1990, Nucl. Phys. A **519**, 375.

Niita, K., T. Sato, H.I.H. Nose, H. Nakashima, and L. Sihver, 2006, Radiation Measurements **41**, 1080.

Nikjoo, H., I.K. Khvostunov, and F.A. Cucinotta, 2002, Radiat. Res. **157**, 435.

Nikjoo, H., S. Uehara, and D.J. Brenner, 1997, *Microdosimetry: An Interdisciplinary Approach*, edited by D.T. Goodhead, P. O'Neill, and H.G. Menzel (The Royal Society of Chemistry, Cambridge, England), p. 3.

Norbury, J.W., and L.W. Townsend, 1990, Phys. Rev. C **41**, 372.

NRC, 2006, *Health Risks from Low Levels of Ionizing Radiation: BEIR VII Phase 2* (National Academies Press, Washington, DC).

Nymmik, R.A., 1996, Radiation Measurements **26**, 417.

Olsen, D.L., B.L. Berman, D.E. Greiner, H.H. Heckman, P.J. Lindstrom, and H.J. Crawford, 1983, Phys. Rev. C **28**, 1602.

O'Neill, P., 2010, IEEE Trans. Nucl. Sci. **57**, 3148.

Paretzke, H., 1987, *Radiation Track Structure* (Wiley, New York), p. 89.

Parker, E. N., 1965, Planet. Space Sci. **13**, 9.

Pellish, J., *et al.*, 2010, IEEE Trans. Nucl. Sci. **57**, 2948.

Plante, I., and F. A. Cucinotta, 2008, New J. Phys. **10**, 125020.

Plante, I., and F. A. Cucinotta, 2009, New J. Phys. **11**, 063047.

Posner, A., 2007, Space Weather **5**, S05001.

Reitz, G., R. Beaujean, E. Benton, S. Burmeister, T. Dachev, S. Deme, M. Luszik-Bhadra, and P. Olko, 2005, Radiation Protection Dosimetry **116**, 374.

Reitz, G., *et al.*, 2009, Radiat. Res. **171**, 225.

Rodger, C. J., and M. A. Clivelrd, 2008, Nature (London) **452**, 41.

Rudd, M., 1997, HZE Interactions in Biological Materials (NASA CP 3360).

Sampsonidis, D., E. Papanastassiou, M. Zamani, M. Debeauvais, J. C. Adloff, B. A. Kulakov, M. I. Krivopustov, and V. S. Butsev, 1995, Phys. Rev. C **51**, 3304.

Schardt, D., T. Elsässer, and D. Schulz-Ertner, 2010, Rev. Mod. Phys. **82**, 383.

Schimmerling, W., J. Miller, M. Wong, M. Rapkin, J. Howard, H. G. Spieler, and J. V. Blair, 1989, Radiat. Res. **120**, 36.

Schimmerling, W., K. G. Vosburgh, and P. Todd, 1971, Science **174**, 1123.

Schimmerling, W., J. Wilson, F. Cucinotta, and M. Kim, 1999, *Requirements for Simulating Space Radiations with Particle Accelerators* (Kodansha Scientific Ltd., Tokyo), p. 1.

Shinn, J. L., G. D. Badhwar, M. A. Xapsos, F. A. Cucinotta, and J. W. Wilson, 1999, Radiation Measurements **30**, 19.

Slaba, T. C., S. R. Blattnig, M. S. Clowdsley, S. A. Walker, and F. F. Badavi, 2010, Adv. Space Res. **46**, 800.

Spence, H., *et al.*, 2010, Space Sci. Rev. **150**, 243.

Spillantini, P., M. Casolino, M. Durante, R. Müller-Mellin, G. Reitz, L. Rossi, V. Shurshakov, and M. Sorbi, 2007, Radiation Measurements **42**, 14.

Straube, U., T. Berger, G. Reitz, R. Facius, C. Fuglesang, T. Reiter, V. Damann, and M. Tognini, 2010, Acta Astronaut. **66**, 963.

Tang, H. H. K., 2005, Nucl. Phys. **A752**, 706.

Townsend, L., 2001, Phys. Med. **17**, 84, Suppl. 1.

Townsend, L., and J. Wilson, 1986, Radiat. Res. **106**, 283.

Townsend, L. W., T. M. Miller, and T. A. Gabriel, 2005, Radiation Protection Dosimetry **116**, 135.

Townsend, L. W., D. L. Stephens, J. L. Hoff, E. N. Zapp, H. M. Moussa, T. M. Miller, C. E. Campbell, and T. F. Nichols, 2006, Adv. Space Res. **38**, 226.

Tripathi, R. K., J. W. Wilson, and F. A. Cucinotta, 1998, Nucl. Instrum. Methods Phys. Res., Sect. B **145**, 277.

Tripathi, R. K., J. W. Wilson, and F. A. Cucinotta, 2001, Nucl. Instrum. Methods Phys. Res., Sect. B **173**, 391.

Tripathi, R. K., J. W. Wilson, and R. C. Younquist, 2008, Adv. Space Res. **42**, 1043.

Tull, C., 1990, Ph.D. thesis (University of California), lBL-29718.

Tweed, J., J. W. Wilson, and R. K. Tripathi, 2004, Adv. Space Res. **34**, 1311.

Tylka, A. J., J. H. Adams, P. R. Boberg, B. Brownstein, W. F. Dietrich, E. O. Flueckiger, E. L. Petersen, M. A. Shea, D. F. Smart, and E. C. Smith, 1997, IEEE Trans. Nucl. Sci. **44**, 2150.

Tylka, A. J., and A. Dietrich, 2009, in *Proceedings of the 31st International Cosmic Ray Conference, Lodz, Poland* [http://icrc2009.uni.lodz.pl/proc/html/index.php_id=1.html].

UNSCEAR, 2000, Volume I Annex B (United Nations Office, Vienna).

UNSCEAR, 2008, Volume I (United Nations Office, Vienna).

Vette, J., 1991, NSSDC/WDC-A-R&S 91-29 (Vienna).

Walker, S. A., J. Tweed, J. W. Wilson, F. A. Cucinotta, R. K. Tripathi, S. Blattnig, C. Zeitlin, L. Heilbronn, and J. Miller, 2005, Adv. Space Res. **35**, 202.

Watson, K. M., 1953, Phys. Rev. **89**, 575.

Webber, W. R., J. C. Kish, and D. A. Schrier, 1990, Phys. Rev. C **41**, 547.

Westfall, G. D., L. W. Wilson, P. J. Lindstrom, H. J. Crawford, D. E. Greiner, and H. H. Heckman, 1979, Phys. Rev. C **19**, 1309.

White, R. J., and M. Averner, 2001, Nature (London) **409**, 1115.

Wilson, J., L. Townsend, W. Schimmerling, G. Khandelwal, F. Khan, J. Nealy, F. Cucinotta, L. Simonsen, J. Shinn, and J. Norbury, 1991, Transport Methods and Interactions for Space Radiations, NASA RP 1257.

Wilson, J., R. K. Tripathi, F. A. Cucinotta, J. L. Shinn, F. F. Badavi, S. Y. Chun, J. W. Norbury, C. J. Zeitlin, L. Heilbronn, and J. Miller, 1995, An Evaluation of the Semiempirical Nuclear Fragmentation Database, NASA TP 3533.

Wilson, J. W., 1974, Phys. Lett. **52B**, 149.

Wilson, J. W., M. S. Clowdsley, F. A. Cucinotta, R. K. Tripathi, J. E. Nealy, and G. DeAngelis, 2004, Adv. Space Res. **34**, 1281.

Wilson, J. W., F. A. Cucinotta, J. Miller, J. L. Shinn, S. A. Thibeault, R. C. Singleterry, L. C. Simonsen, and M. H. Kim, 2001, Mater. Des. **22**, 541.

Wilson, J. W., F. A. Cucinotta, and W. Schimmerling, 2004, AIP Conf. Proc., **699**, 913.

Wilson, J. W., M. Kim, W. Schimmerling, F. Badavi, S. Thibeault, F. A. Cucinotta, J. Shinn, and R. Kiefer, 1995, Health Phys. **68**, 50.

Wilson, J. W., J. S. Wood, J. L. Shinn, F. A. Cucinotta, and J. E. Nealy, 1993, A Proposed Performance Index for Galactic Cosmic Ray Shielding Materials, NASA TM 4444.

Wong, M., W. Schimmerling, M. H. Phillips, B. A. Ludewigt, D. A. Landis, J. T. Walton, and S. B. Curtis, 1990, Med. Phys. **17**, 163.

Xapsos, M. A., G. P. Summers, J. L. Barth, E. G. Stassinopoulos, and E. A. Burke, 2000, IEEE Trans. Nucl. Sci. **47**, 486.

Yasuda, H., M. Suzuki, K. Ando, and K. Fujitaka, 2001, Phys. Med. **17**, Suppl. 1, 133 [http://www.ncbi.nlm.nih.gov/pubmed/11771537].

Zeitlin, C., A. Fukumura, L. Heilbronn, Y. Iwata, J. Miller, and T. Murakami, 2001, Phys. Rev. C **64**, 024902.

Zeitlin, C., S. Guetersloh, L. Heilbronn, J. Miller, A. Fukumura, Y. Iwata, T. Murakami, L. Sihver, and D. Mancusi, 2008, Phys. Rev. C **77**, 034605.

Zeitlin, C., L. Heilbronn, J. Miller, S. E. Rademacher, T. Borak, T. R. Carter, K. A. Frankel, W. Schimmerling, and C. E. Stronach, 1997, Phys. Rev. C **56**, 388.

Zeitlin, C., *et al.*, 2010, Space Weather **8**, S00E06.